Power Balance and Characterization of Impurities in the Maryland Spheromak

by

Claude Côté

Dissertation submitted to the Faculty of the Graduate School
of The University of Maryland in partial fulfillment
of the requirements for the degree of
Doctor of Philosophy
1993

Advisory Committee:

Professor Alan DeSilva, Chairman/Advisor
Professor George Goldenbaum
Professor Hans Griem
Professor Richard Ellis
Professor Charles Striffler

Abstract

Title of Dissertation: Power Balance and Characterization of Impurities in the Maryland Spheromak

Claude Côté, Doctor of Philosophy, 1993

Dissertation directed by: Dr. Alan DeSilva, Professor of Physics, Department of Physics and Astronomy

The Maryland Spheromak is a medium size magnetically confined plasma of toroidal shape. Low T_e and higher n_e than expected contribute to produce a radiation dominated short-lived spheromak configuration. A pyroelectric radiation detector and a VUV spectrometer have been used for space and time-resolved measurements of radiated power and impurity line emission. Results from the bolometry and VUV spectroscopy diagnostics have been combined to give the absolute concentrations of the major impurity species together with the electron temperature. The large amount of oxygen and nitrogen ions in the plasma very early in the discharge is seen to be directly responsible for the abnormally high electron density. The dominant power loss mechanisms are found to be radiation (from impurity line emission) and electron convection to the end walls during the formation phase of the spheromak configuration, and radiation only during the decay phase.

Dedication

A mes parents, Jean-Marc et Denise

Acknowledgements

I am very grateful for all the help and encouragements that I have received throughout my graduate studies from the staff of the Laboratory for Plasma Research (LPR) , from my fellow students, and from the main investigators of the Maryland Spheromak project. The sharing of ideas and equipment among the people participating in research at LPR was truly invaluable and my work has benefited greatly from it. One thousand thanks to Ken Diller and Dave Miller for their technical expertise and good spirit; to Jean-Luc Gauvreau, Alex Filuk, Fu-Kwun Hwang, and Riccardo Capovilla for friendship, stimulating discussions, and tennis sessions; to Cecil Chin-Fatt for his mastery of every aspect of the experimental device; and to Professors Alan DeSilva and George Goldenbaum for having the courage to set this large project in motion and for letting me be part of it.

Extra special thanks go to my advisor, Dr. DeSilva, for his seemingly infinite physics knowledge, for his constant willingness to discuss problems and offer possible solutions, and for his kindness. Je serai toujours reconnaissant à ma famille qui n'a cessé de m'appuyer durant toutes ces années au Maryland. Finally, thanks to Barbara for being my pal and such a great gal.

Table of Contents

List of tables

List of figures

Chapter 1

Introduction

1.1 Magnetic confinement fusion

The promise of an abundant, practically inexhaustible source of fuel has generated a worldwide research effort directed toward the production of a thermonuclear fusion reactor. This daunting project faces hurdles on all fronts. On the technical side, the cost and complexity of today's most advanced experimental devices and of those planned for the future are enormous: on the more purely scientific side, the vast array of processes involved and the inherent limitations of the models used to understand and simulate them often prevent a clear determination of the solutions to current problems and of the requirements for a working reactor; and on the political side, nuclear fusion research is largely dependent on public funds whose availability fluctuates in relation with the state of the economy, the views of the political leaders, the public opinion, and so on. Those factors have contributed to the high degree of international cooperation in this field, as now reflected for example in the proposed project ITER (International Thermonuclear Experimental Reactor).

Considering man's ever-increasing need for energy and the finite supply of fossil fuels and fuel for fission, there is a feeling however that despite those difficulties controlled nuclear fusion is bound to be an important energy source

for future generations. And it would indeed seem fitting and quite natural that the process responsible for the sun's energy and, eventually, for life on earth be finally harnessed and used for the planet's health and prosperity.

The basic objective of fusion research is to heat a plasma so that the colliding ions, most likely coming from a mixture of deuterium and tritium gases, can overcome the repulsive Coulomb barrier (to permit fusion reactions) and to provide a sufficient density and confinement time for a sustained burn, i.e., to reach a condition where the heat input from the fusion reaction products is larger than the power losses from the plasma. Power losses include radiation, ionization, charge-exchange neutral particle losses, conduction and convection, as well as those involved in the maintenance of the confining magnetic field.

In the research for fusion by magnetic confinement, where the requirements on the product $n_i\tau_E$ [1,2] (where n_i is the plasma ion density and τ_E is the energy confinement time) are approached by confining a low density plasma for a relatively long time with the help of magnetic fields, tokamaks [3–6] are the most advanced devices and the closest to engineering breakeven. The word tokamak is a Russian acronym for *toroidalnaya* (toroidal) *kamera* (chamber) *magnitnoi* (of magnetic) *katushki* (coils). A number of alternative approaches are still being investigated [7–10] (albeit with shrinking funding) for their own merit and for their contribution to specific aspects of the general research effort in fusion.

Among the most attractive alternate schemes is the magnetized plasma configuration called spheromak [10–17]. As part of the compact-torus class of devices, this configuration combines the desirable features of closed toroidal confinement and simple poloidal-field-generating coils, which do not link the plasma toroid. Spheromaks are characterized by toroidal and poloidal fields which have comparable magnitudes and are generated primarily by plasma currents. By self-regulating all components of its currents and fields, the plasma can relax to a configuration with a minimum amount of free energy available to drive instabilities; these objects were in fact first described in relation with the observation

of persistent magnetic fields in the Crab Nebula [18,19]. Other favorable features for a fusion reactor include the possibility of translation and compression of the plasma and a high value of engineering beta, the ratio of the plasma kinetic pressure to the externally applied magnetic field pressure. The same features are partly responsible for the recent interest in spheromak injection into tokamaks as a means of tokamaks current drive and refueling [20,21].

For all those magnetically confined devices, an understanding of the ways the power fed into the machine couples to the plasma and a determination of the power loss channels is essential since this energy flow will affect most of the confined plasma characteristics, including its temperature and confinement time. The initial motivation for the work presented here was the study of the power balance of the Maryland Spheromak (MS) [13,22–24]. MS was designed to reach an electron temperature of ~100eV (possibly more with auxiliary heating) and to stay confined for at least 1 *m*sec. Among the original purposes of the machine were long term stability studies, transport scaling with B, T_e, $I_{main\ discharge}$ and n_e, and also sustainment studies. Unfortunately, high electron density and powerful energy loss mechanisms have prevented MS from reaching a high temperature and a long confinement time, and have limited the range of plasma physics problems that the machine can explore.

As the predominant energy loss channel in MS turned out to be impurity line radiation, special efforts were made to characterize the impurities (species present, abundance, possible origin, etc.) affecting the plasma behavior. In particular, a close relation will be shown to exist between the amount of impurity and the high electron density. Impurities always play an important role in fusion research experiments, and will have to be taken into account in the design of any fusion reactor.

1.2 Impurities in fusion plasmas

The observed impurity elements can be broadly divided into two classes according to the mechanism responsible for their production, i.e., desorbed and eroded impurities. Common desorbed elements are carbon, nitrogen, oxygen and chlorine. They can be due to thermal desorption, desorption due to particle and photon bombardment, and chemical reactions which release gaseous contaminants such as water or methane. Recipes for removing absorbed impurities from the vacuum walls and from the surface of the various structures within the vacuum vessel exist and are used on most machines. Oxygen is usually the most abundant desorbed impurity, with typical concentration, relative to n_e, in the 0.5–5% range. In contrast, eroded impurities are less abundant, with concentrations in the 0.1–1% range. These are the metallic components of the walls and other internal structures such as titanium, iron, chromium and nickel. The principal known processes by which the bulk wall material can be removed are sputtering, unipolar arcs and evaporation. Sputtering occurs due to plasma ions, charge exchange neutrals and possibly impurity ions.

The presence of impurities has certain important effects on the bulk plasma parameters. First, because of their high charge, impurity ions contribute significantly to the plasma resistivity. This resistivity in turn affects both the ohmic heating rate and current profile, especially in devices which rely on large circulating internal plasma currents. Another effect is radiative cooling by impurities, which can range from devastating to beneficial, depending on the location and rate at which power is lost. For example, ignition of D-T plasmas can be prevented by the presence, at the plasma core, of only 3% of low-Z elements (oxygen), 1% of intermediate-Z elements (iron), or 0.1% of high-Z elements (tungsten) [25]. On the other hand, low-Z ion radiation at the plasma edge helps in transferring the plasma energy rather harmlessly to the wall. Moreover, they also cool the edge and force the current density (and hence the temperature

and power input) distribution to become more centrally peaked, thus reducing the influx of high-Z impurities, presumably by reduced sputtering. (It should be noted though that when attempting to increase n_e to its maximum possible value, light impurity radiation increases, eventually leading to a major plasma disruption in high T_e tokamaks [26,27]. This may be because light impurities shape the current profile, and that this situation is marginal for stability.)

Another area of interest concerning impurities, aside from their influence on plasma properties, is their increasing use as diagnostics. Spectrometers can be used to study impurity ions throughout the plasma volume since the plasma is optically thin to line radiation. The presence or absence of line radiation from various impurity charge states gives information on the electron temperature. Line intensity ratios can also be used to determine the electron temperature and density. The Doppler width of selected transitions can provide an estimate of ion temperatures. In some cases, plasma flow velocities (such as toroidal rotation in tokamaks) can be measured by the Doppler shift of impurity ions moving with the bulk plasma ions. Finally, the detailed measurement of the spatial distribution and time evolution of impurity ion densities provides a powerful tool for the determination of plasma particle transport and confinement. These observations can either rely on naturally occurring impurity elements, or on impurities introduced in a controlled manner.

1.3 Thesis outline

The Maryland Spheromak experiment is first described in chapter 2. Details are given on the formation scheme, the major components of the experimental setup and the diagnostics used. Some important features of the plasmas produced so far in MS are also highlighted. The following chapter is dedicated to

the pyroelectric detector used for the bolometric measurements; after the general principles of pyroelectric radiation detection have been presented, an account is given of the modifications made to a commercial pyroelectric detector to make it suitable for the radiated power measurements in MS. In chapter 4, the measurements taken with the collimated pyrodetector and a vacuum ultraviolet monochromator looking at impurity emission lines are described. By combining the bolometric and spectroscopic data and by using the results of other diagnostics, it was possible to determine the electron temperature and the absolute concentration of several impurity species at different times. Finally, the power and energy balance of MS are analyzed in chapter 5; the bolometric and high voltage probe data are correlated with the measurements of various other diagnostics, and the main results are compared with what has been observed in other spheromak experiments.

Chapter 2

The Maryland Spheromak

2.1 Fundamentals of spheromak formation

Spheromaks have been produced at the University of Maryland dating back to 1979. The series of experiments named Paramagnetic Spheromak (PS-1 to PS-3.5)[28–31] has inspired the design of the larger Maryland Spheromak. All of these experiments have a common formation scheme consisting of a combination of θ and Z-pinch, with the larger MS operating on a longer timescale. The slower formation scheme in MS limits the effects of instabilities and allows for smaller current density on the electrodes [32].

Spheromaks can in fact be initiated in a number of ways, with the plasma eventually reaching the desired configuration since it is a state of minimum energy. The formation schemes that have resulted in the highest temperatures and the longest confinement times so far have been the inductive flux core method [33] (used for example in the device named S-1 at Princeton University [14]) and the method using a magnetized coaxial gun source with flux conserver [34] (used for CTX at Los Alamos National Laboratory [15]). The coaxial source is also used when translation and/or compression of the plasma is desired, as for the injection of compact-torus into tokamaks [20,21,35]. A description of the various formation schemes and a brief review of spheromak research can be found in reference 10.

The combined electrode and inductive scheme used in MS has the advantage of producing a boundary-free plasma. The absence of a metallic boundary close to the plasma is essential for fusion reactor applications but it does make the spheromak more susceptible to shift, tilt and other instabilities.

A schematic of the essential elements of the MS experiment is shown in figure 2.1. The pair of large coils outside the vacuum chamber (bias coils), represented here in cross-section, produces a constant magnetic field on the timescale of the experiment. These coils, together with a pair of smaller coils inside the chamber (reversal coils) and two annular arrays of electrodes form the basic components used in the creation of the spheromak configuration. The reversal coils and electrodes are part of separate capacitor discharge circuits. Note that a spheromak formed in the MS vessel would have its symmetry axis along the symmetry axis of the machine (the "Z" axis). The conical shapes in the figure represent passive stabilization devices (metallic cones or figure-8 coils). The lines besides the reversal coils represent two glass annuli pushed against the coils to prevent Z-discharge currents (I_z) from running behind the reversal coils.

The time history of a spheromak configuration in MS can be divided into four phases. Formation of the configuration per se occurs during the first two phases, initiation/breakdown and relaxation. This is followed by a decay phase and, finally, by a termination phase.

- **initiation/breakdown**

The formation process is started with the activation of the bias coils, which produce a mirror-shaped external confinement field (figure 2.2(a)). The bias current lasts long enough (a few seconds) to allow thorough magnetic field penetration inside the metallic chamber and to make it possible to treat the bias flux within the vessel as a constant on the timescale of the experiment.

In the next step, the reversal coils are energized to reverse the magnetic field at the machine center. The vacuum vessel acts as a flux conserver on the timescale

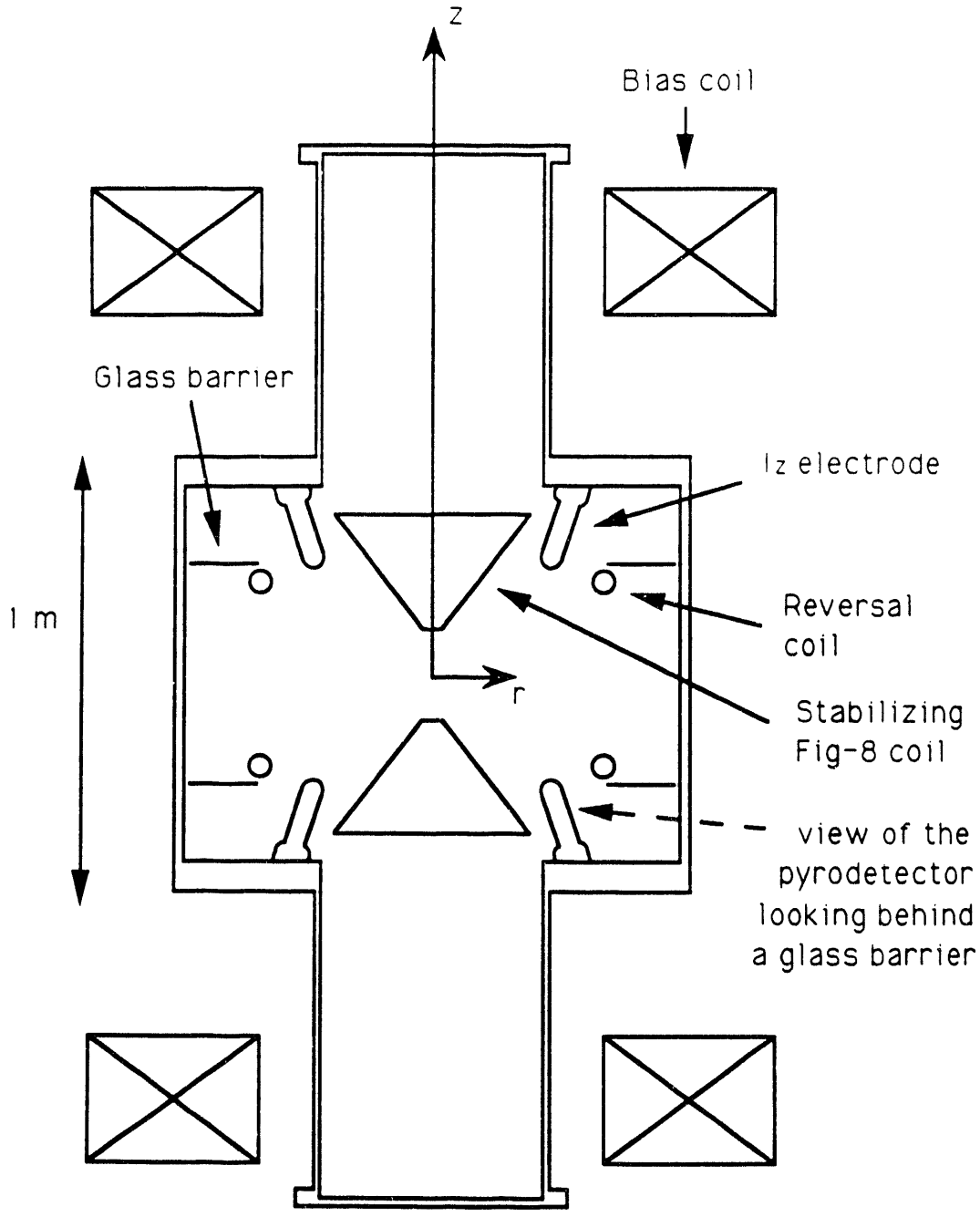

Figure 2.1: MS vacuum vessel and essential components.

of the reversal discharge (90 μsec risetime) and this causes the bias magnetic field lines to be pushed against the vacuum chamber walls (figure 2.2(b)). There is still no toroidal magnetic field.

When the reversal current reaches its peak, the I_z bank is discharged through the electrodes, breaking down the gas (which had been puffed in a few $m$sec before) and producing the plasma. The I_z discharge creates the toroidal magnetic field and provides the initial heating currents (figure 2.2(c)).

During the rise of the I_z pulse, and as the reversal current decreases, a toroidal plasma current is induced just inside the reversal coils (one can say that the reversed magnetic field near the axis is trapped by the recently created and highly conductive plasma). Now as the reversal current returns to zero (both the I_z and reversal discharges are crowbarred to prevent ringing) and enough induced toroidal plasma current's poloidal magnetic field has been generated, the poloidal field just inside the reversal coils gets reversed. This allows reconnection processes to occur that detach the configuration of magnetic fields from the reversal coils structure to form a closed poloidal flux configuration inside the coils [32].

- **relaxation**

The various processes involved in the passage from the configuration reached at the end of the initiation/breakdown phase to the minimum energy configuration called the Taylor state [36,37] constitute the relaxation phase [38–40]. MS was designed to form a plasma with toroidal and poloidal fields that are initially as close as possible to those of the desired final state in order to minimize the reliance on internally generated instabilities during the relaxation phase.

The transition to the Taylor state is characterized by some conversion of poloidal to toroidal flux and vice versa. The final state is a force-free magnetic configuration where the plasma current J is parallel to the plasma magnetic

field **B**:

$$k_0 \mathbf{J} = \nabla \times \mathbf{B} = k\mathbf{B}$$

with k a constant depending only on boundary conditions. In a spherical geometry, the solution to this equation is an expansion in spherical Bessel and associated Legendre functions. To describe classical force-free spheromaks, two terms are kept [41]. The n=0, m=1 term gives the spherical solution and the n=0, m=3 term defines the deviation of the separatrix shape from a sphere. (The separatrix is the surface forming the boundary between closed and open field lines inside the vacuum chamber.) From the first zero of the spherical Bessel function $j_1(x)$, we obtain, for the classical spherical spheromak, $|k|R_s$=4.4934, where R_s is the separatrix radius. The magnetic field structure for this spheromak is shown in figure 2.3.

- **decay**

After the spheromak has formed, and if no sustainment method is used, its internally generated magnetic fields resistively decay, causing the major radius of the plasma to shrink in a constant external magnetic field (figure 2.2(d)). During that phase, the details of the formation scheme have lost their importance and different spheromaks may be compared more readily.

- **termination**

When the plasma configuration becomes too small to be stabilized, a global, rigid body, MHD instability typically terminates the discharge [41,42].

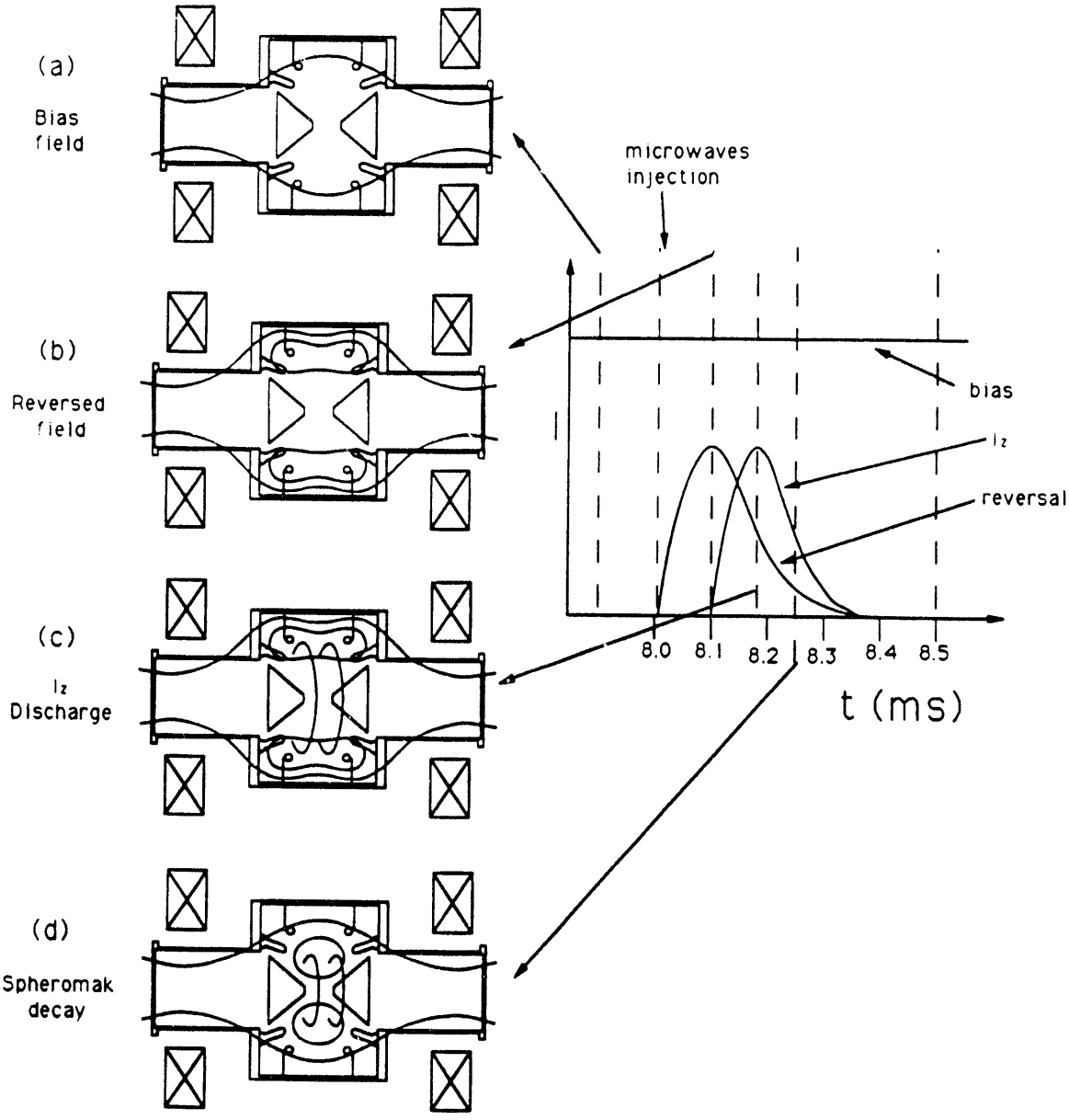

Figure 2.2: MS formation sequence.

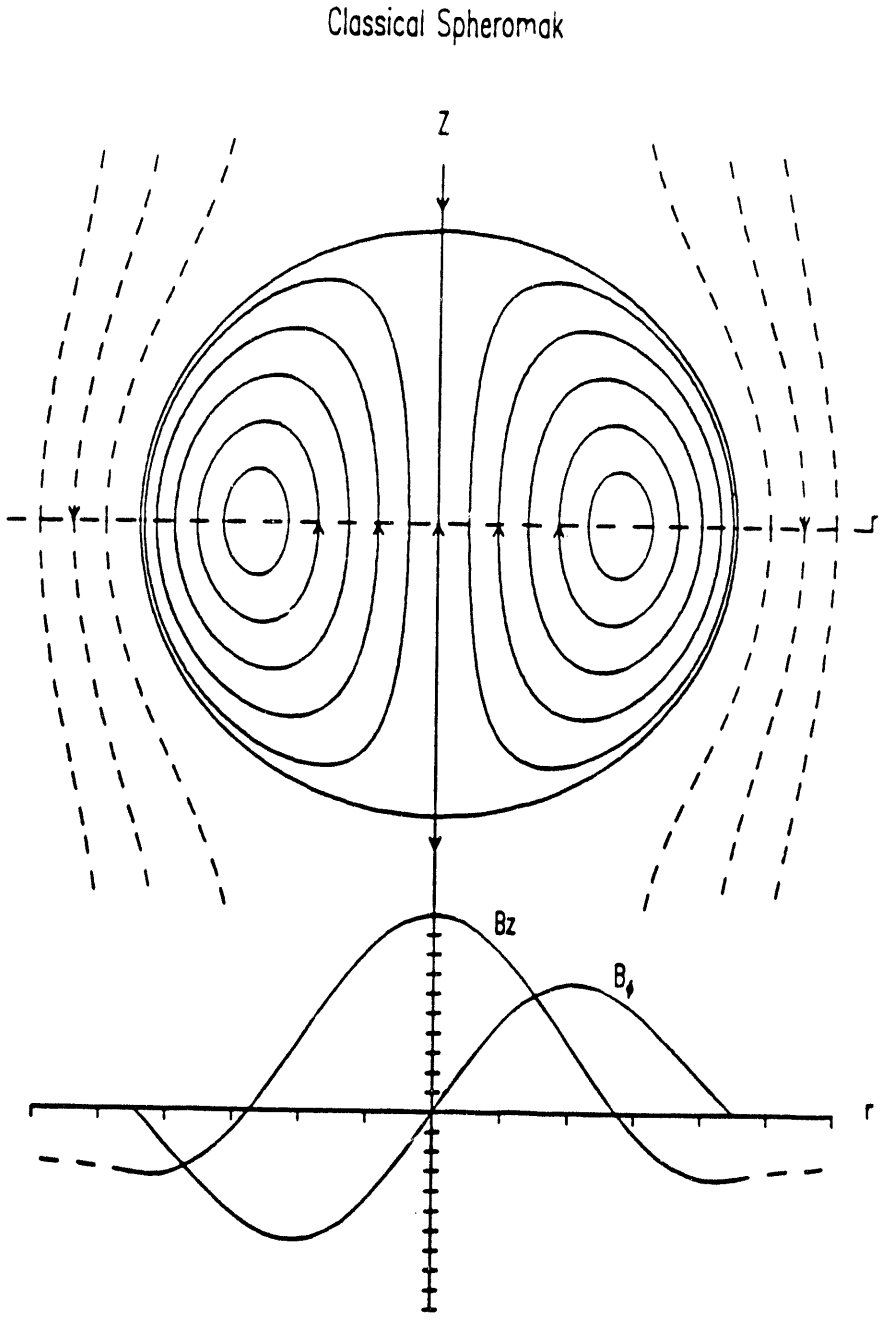

Figure 2.3: Poloidal flux contours of the classical spheromak and its magnetic field profiles on the midplane.

2.2 Detailed description of MS components

2.2.1 Vacuum vessel and pumping system

The MS vessel consists of a main cylindrical chamber and two detachable extensions at each end, all made of non-magnetic stainless steel (see fig. 2.1). The central section is 80 cm long with a 102 cm inside diameter and a wall thickness of 1.9 cm. The extensions, also cylindrical, are 61 cm in length, 46 cm in diameter and have a wall thickness of 0.63 cm.

The vacuum chamber is brought to a base pressure in the 10^{-7} Torr range by two turbomolecular pumps and one cryogenic pump. The turbo-pumps are connected to the central section through 15 cm (diameter) ports and are installed some 2.5 meters away from the vessel to prevent malfunctions caused by the strong bias magnetic field. The cryo-pump is attached directly to an extension section endplate through a 20 cm port and has consequently about 10 times (at $\sim$ 4000 l/sec) the pumping speed of a single turbo-pump.

2.2.2 Bias coils

The bias coils encircle the extension sections and have a mirror ratio of about 5:1. Each coil is made of 600 turns of high purity aluminum foil, with a case serving as a liquid nitrogen dewar. The coils are driven in series by a direct current power supply capable of delivering up to 4 kA for up to 10 seconds. The field at the machine center is 2.2 kG/kA. For the results reported here, the current in the coils was in the range 350–500 A and the bias coil system was sometimes used without liquid nitrogen.

2.2.3 Reversal coils and energy storage system

The two coils have a major diameter of 70 cm and are separated by 38 cm. Each coil is a single turn of solid stainless steel with a circular cross-section 5 cm in diameter. It is epoxied inside a restraining yoke at the entrance point in the vessel. To restrain the coils during a discharge, a few alumina cross-bars are inserted between the coils. The reversed field at the center is 11.6 kG/MA. Note that there is a small up-down asymmetry in this setup from the feeding points of the single turn coils.

The reversal coils are fed by a capacitor bank consisting of fourteen modules with 10 capacitors (11 kV, 175 μF) per module, capable of driving 600 kA in each coil with a quarter period of 90 μsec. In normal operation, the bank is charged to $\pm$4.5 kV and about 250 kA flows in the reversal coils (depending on the temperature in the experimental area).

2.2.4 I_z electrodes and associated capacitor bank

The 2$\times$16 electrodes form an annular array at each end of the main chamber. Each electrode points toward the central region at a 15° angle (with respect to the machine symmetry axis) and enters the back wall through alumina ceramic insulator. The electrodes have a cylindrical (3.175 cm diameter) stainless steel body with replaceable rounded tips. Elkonite (a Cu-W alloy) tips have been used for the work presented here. The distance between the machine axis and the tips of the electrodes is 25 cm, and the end-to-end tip separation is 41 cm.

The I_z electrodes are energized by a capacitor discharge (96$\times$20 kV, 60 μF capacitors) with a quarter period of 80 μsec. The capacitor bank can deliver up to 1.5 MA in the I_z circuit but for most of the shots the capacitors are charged to 11-12 kV and I_z is in the range 800-1000 kA.

2.2.5 Figure-8 coils

To stabilize the plasma against n=1 toroidal mode shifting and tilting instabilities, a pair of passive structures called figure-8 coils [43–45] are inserted in the main chamber. The conically shaped copper coils are installed on axis with the tip of the "cone" extending a few cm past the I_z electrodes toward the machine center. Induced currents on these figure-8 coils maintain the flux difference between the two loops constant. Solid aluminum cones have also been used as passive stabilizer but figure-8 coils have proven slightly more effective and also allow axial injection of the working gas and of microwaves (see section 2.2.7).

2.2.6 Puff valve

The working gas, usually D_2, is injected axially 1 to 2 $m$sec before the shot by a fast-acting puff valve located at one end of the main chamber. A 1 or 2 $m$sec time delay is too short to allow a static filling of the entire vessel and the gas is more concentrated in the central region; this helps prevent gas breakdown near the reversal coils and the creation of undesirable current paths, and also limits the amount of recycling. Static fill pressures are in the range 2–4 mTorr for the majority of the shots. Note that 1 mTorr of D_2 yields an electron density of about 0.66×10^{14} cm^{-3} if the gas is fully ionized and no other source of electrons is present.

2.2.7 Microwave pre-ionizer

Deuterium gas does not break down readily for static fill below ~5 mTorr when Elkonite electrodes are used. To obtain smooth and reproducible breakdowns, the gas is partly ionized before the I_z discharge by a 40 μsec 200 kW microwave

pulse. The tunable magnetron used as a source is set to produce microwaves with a frequency of 8.56 GHz. This will match the electron gyrofrequency, and help the ionization process through electron cyclotron resonance (ECR), for a magnetic field of 3 kG. The axially launched microwaves encounter fields of that magnitude in the central region (where pre-ionization is desirable) just prior to the I_z discharge. Nonetheless, it was observed that the microwaves are much more effective when launched at the reversal coils firing time. There are resonant magnetic fields around the reversal coils soon after firing and this may help create a seed plasma near them. The reversal discharge then becomes the main pre-ionizer through inductive breakdown. This possibly has a negative impact on the impurity content of the plasma. Details of the microwave pre-ionizer setup are given in the appendix.

2.3 Diagnostics

- **Machine monitors**

The bias magnetic field, being a DC field, cannot be measured with regular magnetic probes. Instead it is calculated from the current (determined from the voltage drop across a precision resistor inside the power supply) in the bias coils and the result is added to the pulsed field measured by the probes inside the vessel.

The current flowing through the I_z electrodes, as well as the current in each reversal coil, are monitored by Rogowski loops. Figure 2.4 shows these current waveforms for a typical shot. Note that the I_z discharge uniformity across the 16 electrodes has been established by small Rogowski loops encircling individual electrodes.

The voltage at the base of the electrodes is monitored at each end by voltage

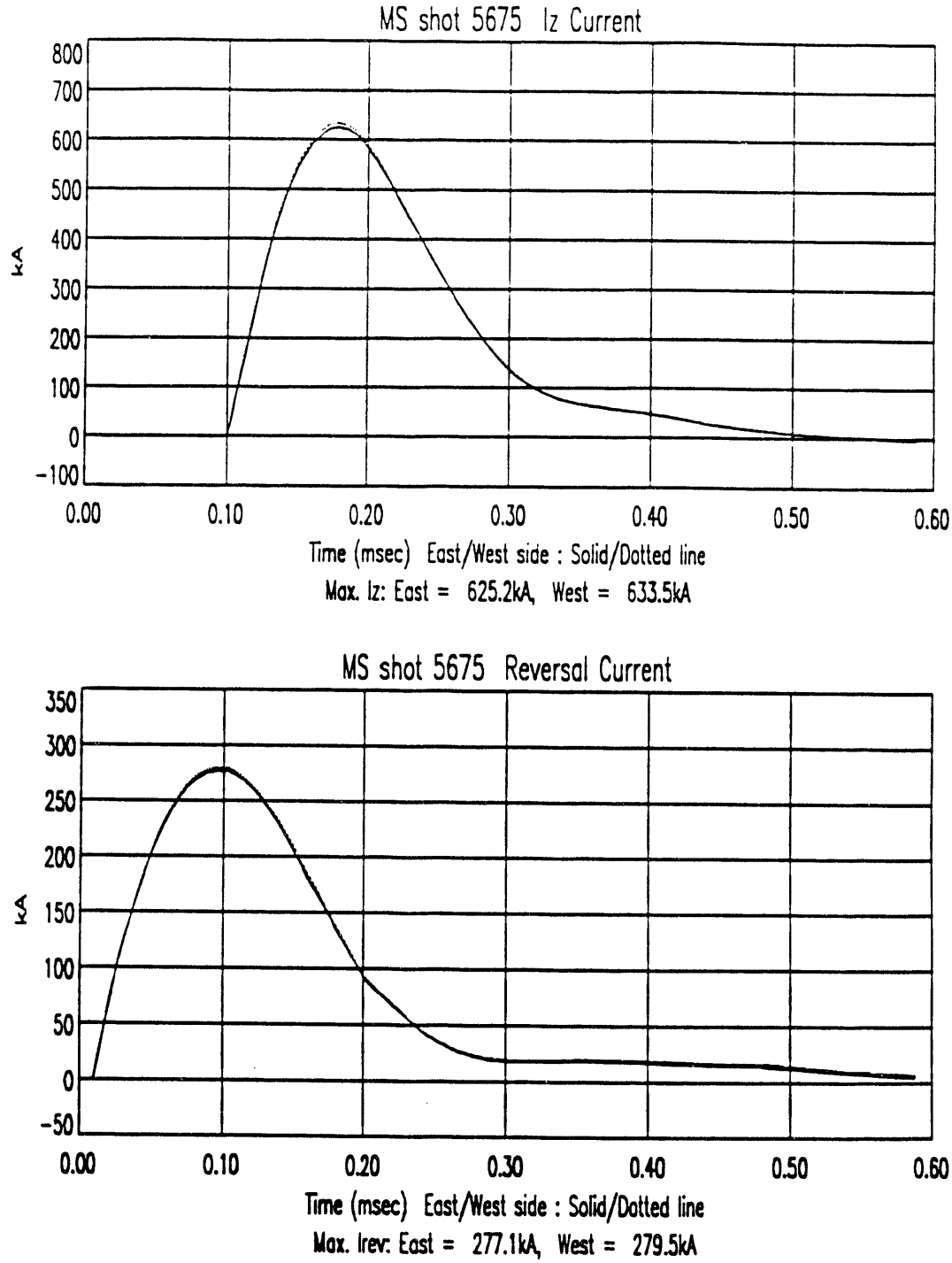

Figure 2.4: I_z and reversal current waveforms. The time 0.10 *m*sec in this figure corresponds to the 8.10 *m*sec used in the rest of the thesis to denote the start of I_z.

dividers (RC compensated). Each divider measures the voltage relative to the screen room ground.

Finally, besides the standard vacuum gauges, a residual gas analyzer (RGA) is used to monitor the quality and characteristics of the machine vacuum.

- **Magnetic probes**

Passive magnetic flux loop probes inserted in the plasma were essential in the study of the formation phase, in confirming the formation of a spheromak and in determining the magnetic structure and stability of this spheromak plasma. Obviously, a more sophisticated diagnostic would have been needed if the presence of probes in the plasma was unacceptable, as it is the case when very high electron temperatures are approached.

Two main arrays of probes have been used in MS. The first, called the midplane probe, is a set of 8 equally spaced pickup coil doublets embedded in a glass body and covered by a thin stainless steel jacket. This probe is inserted radially in the midplane and measures the z and ϕ components (in cylindrical geometry) of $\mathbf{B}$ as a function of r. The time evolution of B_z and B_ϕ for a typical shot is shown in figure 2.5. The second main probe, named the L-probe because of its shape, consists of seven triplets of coils lying in the 19 cm long shorter section of the L. The coils of a triplet are orthogonal and all components of $\mathbf{B}$ can be measured. The longer section of the L-probe is the support rod, radially entering the chamber through a sliding seal on the midplane. The L-probe may be rotated and pulled to produce magnetic field scans in a r-z plane throughout either side of the midplane. Orienting the probe perpendicular to the machine axis allows for midplane scans. Maps of the magnetic structure are obtained by averaging a few shots for a large number of probe positions, taking advantage of the good shot to shot reproducibility of the magnetic fields. A small probe was also placed near the main chamber wall to monitor poloidal currents in that region.

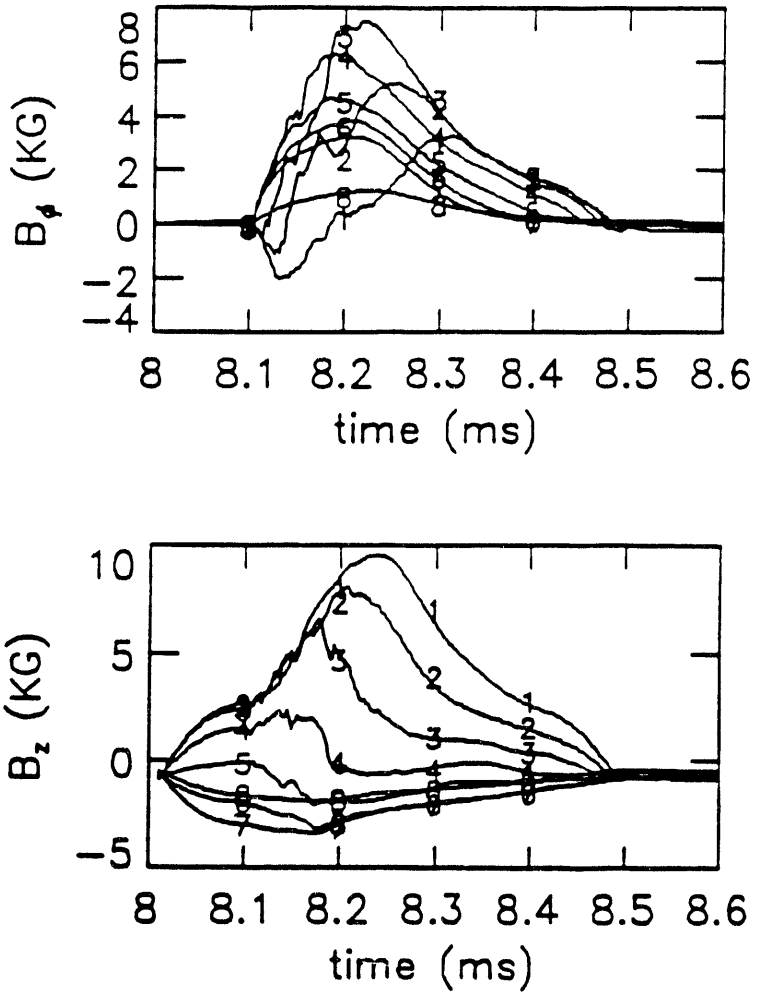

Figure 2.5: Typical toroidal (B_ϕ) and poloidal (B_z) magnetic field traces in the midplane. Signals nb 1–8 correspond to r=[7.18, 13.52, 19.88, 26.23, 32.58, 38.92, 45.28, 51.63] cm respectively.

The magnetic probes were calibrated with a Helmholtz coil. Output signals are integrated with RC filters having time constants in the *m*sec range. The original data were numerically corrected to account for the finite integrator RC time.

• **Interferometry**

The electron density in the midplane is monitored by a four channel He-Ne laser interferometer operating in quadrature mode [46]. The laser beams have a minimum inter-beam separation of 3.8 cm and can be moved vertically to view 8 chords (4 at a time) in the lower half of the midplane. The interferometer setup and the reflecting mirrors located on the other side of the machine are mounted on air-supported granite slabs. For density measurements at a radius greater than 31 cm, Langmuir probes were used. The line-integrated chord data were inverted (with the help of the edge measurements and assuming cylindrical symmetry) using a Bessel function method to obtain radial density profiles for different times.

• **Spectroscopy and bolometry**

Spectroscopic instruments used in MS include two 1/4-meter monochromators, an optical multichannel analyzer (OMA) coupled with a 1 meter spectrometer, and a 1 meter VUV spectrometer (McPherson model 225).

The 1/4-meter monochromators are usually set on carbon and oxygen lines for routine monitoring. The lines chosen are somewhat indicative of the degree of cleanliness of the plasma. The OMA was used for a variety of tasks including ion temperature measurements through time resolved impurity line widths, time history recordings for impurity line emission, scans revealing the spatial distribution of selected ions and measurements of electron temperature using the line ratio method. A second OMA has been used briefly in a low resolution mode to survey the line emission in the visible and near UV for different machine conditions.

The VUV spectrometer was first used in combination with a X-ray film (Kodak type 101) to make a broad survey of the line emission in the 300–2300 Å range. After all of the important lines in that spectral range were identified, the spectrometer was fitted with a photomultiplier tube to reveal the time histories

of the dominant lines. VUV spectroscopy in MS will be described in details in chapter 4.

A pyroelectric detector was used to measure the power radiated from the MS plasma. It was used with a collimator to view different regions of the plasma, and also as a "2π" (solid angle) detector without collimation. Several filters (quartz and LiF windows, Al and C foils) were used with the pyrodetector to select particular spectral regions. Results from the bolometry and the VUV spectroscopy diagnostics have been combined in a way that gives the absolute intensity of all impurity lines seen by the VUV spectrometer. This was then used to determine the concentrations of several impurity species as a function of time. The pyroelectric detector is the subject of the next chapter and the bolometric measurements are presented in chapter 4.

2.4 Overview

2.4.1 Shift instability

The early MS shots were dominated by a shift mode caused by the interaction of the plasma with the bare reversal coils. Magnetic probes indicated the presence of currents flowing from the plasma to the coils, causing the spheromak to form off-center and then to drift in a reproducible manner, independently of the initial conditions. In the design of the experiment, it was thought that the strong magnetic fields surrounding the reversal coils would prevent any current flow to these coils.

To eliminate the shift, the reversal coils were completely covered with a wrapping of teflon tape to insulate them from the plasma. An electrically floating layer of Nichrome foil is applied over the teflon tape to prevent excessive evapo-

ration and gas desorption that would result from the direct contact between the plasma and the teflon wrapping. Titanium foil was also tried as the protective metal layer but it became shredded and torn after a few hundreds shots due to magnetic forces and embrittlement[47]; it could also have enhanced the recycling of impurities since titanium is known to absorb oxygen and hydrogen very well.

With the insulating teflon tape covered with Nichrome foil, used for the work described here, the spheromak forms symmetrically, decays exponentially on axis and starts shifting only after the separatrix has shrunk appreciably in the termination phase.

2.4.2 I_z discharge paths

The second unexpected characteristic affecting earlier MS discharges was the splitting of the I_z discharge in 2 major current paths (again detected by magnetic probes). Both of those paths followed the poloidal magnetic field lines encircling the reversal coils and intersecting the I_z electrode tips at the moment of I_z discharge initiation; but as about half of the current would flow directly between the electrodes along the field lines close to the symmetry axis, the other half would follow the longer but lower inductance path along the magnetic field lines located between the reversal coils and the chamber wall (see figure 2.2(b)). Clearly, the outer current path could lead to additional impurity contamination, lower ohmic heating of the bulk plasma, and lower spheromak magnetic field strength.

After unsuccessful attempts at modifying the I_z electrode's ceramic insulators to block the undesirable current path, 2 large glass annuli were inserted in the chamber and placed in such a way as to form a barrier between each reversal coil and the vessel wall (see figure 2.1). The glass annuli were very effective, stopping completely the current in the outer path and having minimal effect

on the plasma density. The resulting larger central current nearly doubled the spheromak poloidal and toroidal B fields, allowing for field strength values of over 10 kG. Unless otherwise noted, all the data presented here were taken with the glass annuli in the chamber.

It should be mentioned that even with the glass barriers there is still a fraction, about 10% , of the I_z current not flowing directly from one set of electrodes to the other. On most of MS shots, some current flows from the electrode tips directly back to the chamber wall along the surface of the electrode's ceramic insulators. This may be an important source of oxygen and aluminum impurities for the plasma. Unfortunately, only a major redesign of the electrodes and their insulation could solve this problem, as various attempts at a quick fix have shown.

2.4.3 Plasma density

Figure 2.6 shows a typical interferometer trace from a beam scanning the central midplane chord. It represents the line averaged electron density as a function of time. After peaking at around 10×10^{14} cm^{-3} shortly after the peak of I_z, the electron density is about 7×10^{14} cm^{-3} when the spheromak forms at t=8.25 $m$sec, then stabilizes at $\sim4\times10^{14}$ cm^{-3} during a good portion of the spheromak decay.

The deuterium fill gas pressure for that shot was 2 mTorr, and if fully ionized, this amount of gas would give an electron density of 1.3×10^{14} cm^{-3}. So the electron density is higher than would be expected from the injected gas fill. On top of that, n_e does not scale with the amount of gas injected for fill pressures below 10 mTorr, so compressional effects or some other effect related to the dynamic gas filling (as opposed to a static fill) cannot be the only causes of the excessive electron density. Strong recycling of gas from the vessel internal

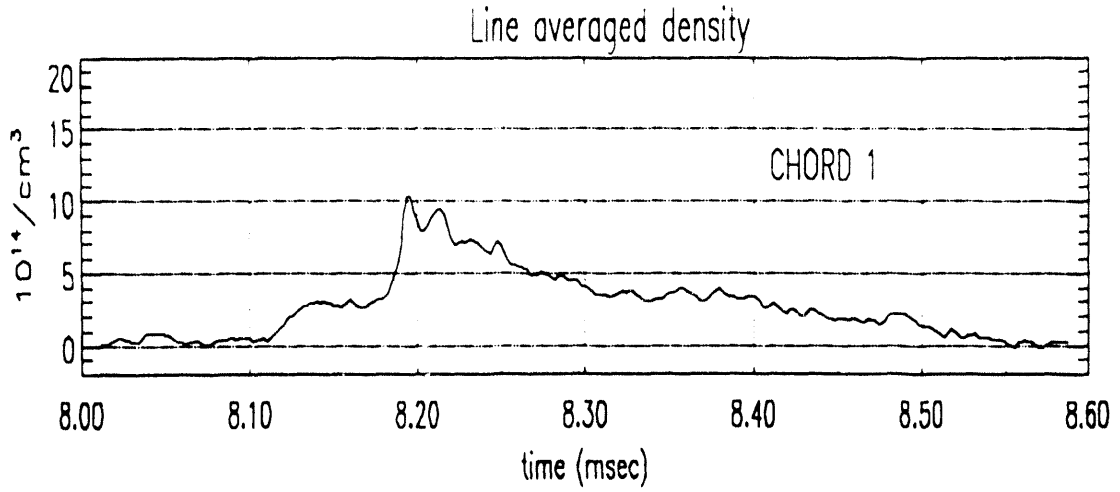

Figure 2.6: Interferometer trace of the line averaged electron density for the central midplane chord.

structures (including the walls) and/or very large amounts of impurities must be invoked to explain the density measurements. This subject will be covered again in chapter 4 when concentrations of the major impurities will be calculated from bolometric and spectroscopic data.

2.4.4 Wall conditioning

High plasma density, electron temperature on the order of only 15 eV at spheromak formation (based on highest impurity ionization stages observed) and minimal influence of the amount of ohmic heating on the plasma temperature and confinement time together indicated that the spheromak was radiation dominated. High n_e combined with low T_e makes for a high plasma resistivity resulting in a rapid decay of the internal magnetic fields.

In order to control gas recycling and reduce impurity influx, a number of wall conditioning techniques have been used. Heating of the machine chamber walls and extensive discharge cleaning in hydrogen had little effect on subsequent MS discharges. Titanium gettering (usually preceded by some discharge cleaning) was more effective however, and the electron density could be seen to go down by 30% or so after application of the getter material. The density would slowly creep back up after a few dozens shots as the titanium became saturated. The base pressure did go down dramatically after gettering but it would go back to its usual level faster than the electron density would. Note also that no correlation between the base pressure and n_e was ever found in MS for shots with no wall conditioning.

Even if titanium gettering was partially successful at lowering the plasma density, the temperature and confinement time of the plasma remained basically unchanged and the spheromak was still believed to be radiation dominated. The electron density could have been reduced a little more by somehow coating the vacuum vessel surfaces left uncoated by the Ti-ball used for gettering. But these sections were a small fraction of the surfaces exposed to the plasma and it is very doubtful that coating them would have had any effect on the plasma confinement time and temperature. Due to the rapid saturation of the getter material and the need for reproducible shots in the data taking process, titanium gettering was not used for the measurements described in the following chapters.

2.4.5 Observations of high ion temperatures

Anomalous ion heating has been observed in many magnetic fusion experiments [48–51] dating back to measurements made on the toroidal pinch Zeta in 1958 [52]. Classically, ions are heated through collisions with the electrons and therefore cannot have a higher temperature than that of the electrons. In MS, it

was observed that the ion temperatures are highest about 20 μsec after the start of the I_z discharge and then decay, eventually matching T_e at the end of the discharge. For O IV, the peak temperature is on the order of 200–300 eV and in general is lower for lower ionization stages. Possible mechanisms responsible for the anomalous heating are instability wave oscillations, helicity transport, tearing modes and X-point heating. This last mechanism, X-point heating [32,53], was found to be the most likely ion heating process in MS [54]. I_z filamentation early in the discharge creates X-points through which ions are accelerated; mass flow kinetic energy is then converted into ion temperature due to plasma viscosity.

Chapter 3

Pyroelectric detection of plasma radiation

Pyroelectric detectors [55-60] were originally chosen to measure the radiation losses in MS because of their low cost, simplicity of use and fast response time. Unfortunately, the commercial pyrodetector first acquired for the bolometric measurements turned out to be totally unsuitable for the task. Large spurious signals, sometimes indicating that the detector was being cooled down when irradiated, were generated when the detector was exposed to the plasma radiation. After eliminating electromagnetic noise as the possible culprit with careful attention to the shielding of the detector and its electronics, the origin of the false signal was traced down to currents created by photoelectrons being ejected when vacuum UV light was striking the detector surfaces (back and front) and its mount.

Commercially available fast pyroelectric detectors are designed to monitor infrared radiation and although all manufacturers claim broadband (X-ray to infrared) detection capabilities, the design of those detectors is in general inappropriate for plasma radiation measurements. Simple modifications to the detection set up, like the use of a biased grid to control the photoelectrons [61] or the insertion of masks to prevent the radiation from hitting certain areas [62], proved only partially effective at eliminating the spurious signal affecting the performance of the commercial pyrodetector when used in MS. Since this pho-

toelectric false signal is much larger than the pyroelectric signal, it needs to be completely eliminated, and it was concluded that the design of the detector itself had to be changed. Miraculously, the particular commercial detector used (Molectron model P1-13) needed only simple design changes that had no effect on its fundamental characteristics (sensitivity, time response,etc.), as described in the second section of this chapter.

Fast pyroelectric detectors used in other plasma experiments have rarely been described in details in the literature. One of the most complete description of a fast pyrodetector used to measure radiation down to 400 Å can be found in reference 63 (this is an article translated from a Russian journal). There is no mention, however, of the need to suppress the spurious signal coming from a current generated when photons with a high photoelectric yield strike the detector surface. The false signal could have been only partially suppressed in a way that was acceptable for the experiment described in the article but would be insufficient in the case of MS. So building a detector based on the design of some (apparently) working plasma radiation pyrodetector would have possibly been useless if the Maryland Spheromak environment proved too challenging for the custom-made device. The approach chosen here of modifying an inexpensive commercial detector was invaluable in defining the design requirements on fast pyrodetectors for them to be true broadband detectors. In order to appreciate these design considerations, some aspects of the theory of pyroelectric detectors are covered next.

3.1 Principles of pyroelectric radiation detection

In 1938, Ta suggested that pyroelectric crystals of the mineral tourmaline could be used for detecting infrared radiation [64]. The implementation of this idea was

delayed until the early 1960's when advances in solid state electronics had made such infrared sensors practical [65,66]. Pyrodetectors were initially confined to military and security applications but an increasingly large number of uses have been found in recent years [55,58].

A pyroelectric material is one which possesses an inherent electrical polarization. This spontaneous polarization is a consequence of the crystal particular symmetry and bonding, and is temperature dependent. Most pyroelectrics are also ferroelectric, which means that the direction of their polarization can be reversed by the application of a suitable electric field, and this polarization reduces to zero at some temperature known as the Curie temperature, T_c, by analogy with ferromagnetism. The dependence of the polarization P on temperature is typically of the form illustrated in figure 3.1. The gradient of this curve, dP/dT, at a particular temperature T, is the pyroelectric coefficient, which is usually denoted by p.

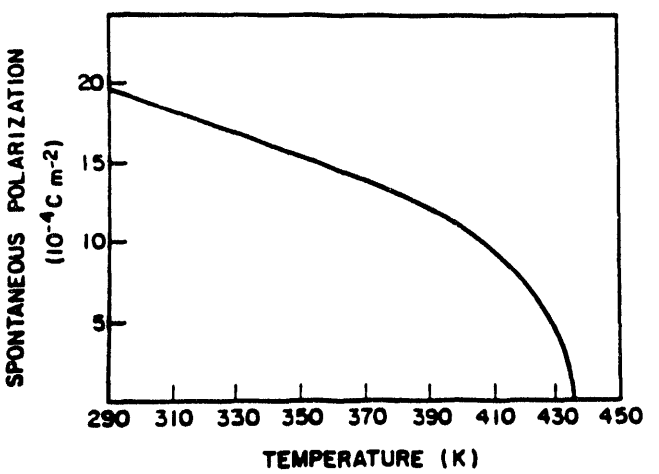

Figure 3.1: Temperature dependence of the spontaneous electric polarization P in terbium molybdate. This example is taken from reference 67.

A pyroelectric detector is a capacitor formed by depositing metal electrodes on a slice of pyroelectric material. with the material being oriented such that its polar axis is perpendicular to the electrode faces. Generally, a ferroelectric consists of a large number of separate domains with differing directions of polarization, so that the net effect over the whole slice is zero. Before use, therefore, these domains must be reoriented by the application of an electric field so that all become parallel to one another. This "poling" process usually consists of heating the detector material above the Curie temperature, applying a large bias to it and then slowly cooling the detector down to room temperature with the bias applied.

Even across a correctly poled detector, there will generally be no observable voltage. This is because its internal polarization is balanced by a surface charge which accumulates via various leakage paths between the two faces. For this reason, the pyroelectric detector can only be used in an a.c. mode and at a frequency high enough for this electrical leakage to be ineffective. Pyroelectrics being very good insulators however, it turns out that even quite slow changes in the sample's temperature produce a measurable change in surface charge.

When the detector is heated by incident radiation, the polarization changes by an amount determined by the temperature change and the pyroelectric coefficient of the material. This produces a change in the charge on the electrodes, and charge flow will occur in an external circuit. The pyroelectric charge generated, Δq, is equal to $pA_d\Delta T$, where A_d is the area of one electrode and ΔT is the temperature change of the pyroelectric material. The pyroelectric current is therefore given by:

$$i = \frac{dq}{dt} = pA_d\frac{dT}{dt}.$$

Expressing dT/dt in terms of the incident power P_i and neglecting heat losses for the moment, we get:

$$i = \left(\frac{p}{\rho c_p l}\right) P_i \tag{3.1}$$

where ρ is the density of the pyroelectric material, c_p is its specific heat at constant stress, and l is the electrode spacing. Responding to the rate of change in temperature rather than directly to the temperature itself, pyroelectric detectors are power meters that can be used at frequencies much higher than those associated with the thermal response of the device, which like that of other thermal detectors is quite slow.

In order to detect the small pyroelectric currents, low noise high impedance amplifiers are necessary. The basic equivalent circuit of the pyroelectric element is simply a current source in parallel with its own capacitance and resistance (which is very high). Let us assume that the input power varies as $P_i(t)=(P_i/2)(1\text{-}\cos\omega t)$. Then for a uniformly heated detector element and a simple thermal circuit (involving only the heat capacity of the detector element and a fixed thermal conductance path to a heat sink), the responsivity R_v, defined as the ratio of the output voltage to the input power, takes the general form [68]:

$$R_v = \left(\frac{p}{\rho c_p l \omega C}\right)\left(\frac{1}{\sqrt{1+(\omega RC)^{-2}}\sqrt{1+(\omega\tau)^{-2}}}\right) \tag{3.2}$$

where R and C are the parallel resistance and capacitance of the detector and external circuit, and τ is the detector thermal time constant. The characteristic features of the responsivity are that it tends to zero both as $\omega \rightarrow 0$ and $\omega \rightarrow \infty$ but for ω between $1/RC$ and $1/\tau$ the responsivity is nearly independent of frequency and is given by $R_v=pR/\rho c_p l$. As the load resistor increases, the voltage responsivity increases but the frequency response decreases. With a small load resistor, flat response from 1 to 10^9 Hz is possible.

Rigorous analyses of pyroelectric detectors have been performed [59], taking into account the effects of mounting techniques and black coatings. The relation given above for the voltage responsivity, however, is adequate for most applications.

The performance of the detector is limited at low radiant power levels by noise,

which can arise from several sources. Since the pyroelectric material is also piezoelectric, mechanical stresses on the bolometer will produce output noise. A piezoelectric signal can be generated simply by the thermal expansion caused by incoming radiation. Another noise source is the thermal noise that occurs due to variations in the bolometer temperature. In fusion research applications however, this and some of the piezoelectric signal associated with sound waves can be reduced to a negligible level by the thermal and acoustic isolation afforded by mounting the sensing element in vacuum.

Besides the commercial applications in infrared detection and imaging, pyroelectric detectors have been used to measure particle fluxes [68–70], radiation losses from high temperature plasmas [61–63,70–75], X-ray bursts [76], blow-off energy from laser-produced plasmas [77], vacuum UV radiation [78,79], and waveform of subnanosecond laser pulses [80,81].

3.2 Development of a fast broadband detector

3.2.1 Description of a commercial miniature detector

The commercial pyrodetector used is simply a square slice of the pyroelectric material lithium tantalate ($LiTaO_3$) mounted on a ceramic substrate and inserted in a TO5 transistor-type housing. The front electrode is circular, with a diameter of 3 mm, and was made by evaporating a thin layer (100 Å) of chromium on the central part of the $LiTaO_3$ crystal. A gold coating forming a narrow strip extends from the electrode's outer edge to a corner of the crystal, and a small gold wire glued to this gold section with conductive epoxy makes the electrical connection with one of the TO5 housing outgoing pins.

The back electrode, which covers the entire underside of the crystal, consists

of a thick layer of gold on top of a thin coating of Cr. The 200 Å or so Cr layer is used to improve the bond between the gold and the $LiTaO_3$ crystal. Although the company making the detector could not give a precise value for the thickness of the gold electrode, a rough evaluation was made by observing the crystal side-on with a microscope. An approximate value of 2 μm for the thickness of the back electrode is obtained by comparing the gold layer with the 50 μm thick $LiTaO_3$ crystal.

To provide thermal insulation at the center of the detector, the crystal is mounted slightly above the substrate on four small beads of conductive epoxy located at the corners. These supporting beads also establish the electrical connection between the back electrode and a conductive path on the underlying substrate leading to one of the housing outgoing pins. The substrate chosen and the mounting scheme minimize vibrations of the detector and stresses in the crystal generated by rapid heating, and this helps suppress piezoelectric noise (microphonic effect).

The use of a thin semi-transparent front electrode and a thicker back electrode gives the detector an absorption coefficient of approximately 50% throughout the visible and the infrared [82,83]. The response time of the sensitive part of the detector is fast, less than 1 ns, because the 100 Å top Cr layer transfers heat quickly to the pyroelectric crystal.

The external circuit used to convert the pyroelectric current to a voltage is shown in figure 3.2. This setup is only one of many possible circuit arrangements but it is the one used for the measurements on MS. It is often called a current mode circuit because the action of the operational amplifier is to hold the voltage near zero at the electrode terminals while causing the pyroelectric current to flow through the feedback resistor R_f. The output signal amplitude is then simply controlled by the magnitude of this feedback resistor when the detector is operating within its flat frequency bandwidth. The feedback capacitance C_f

is used to reduce electrical overshoot and ringing when using a small R_f.

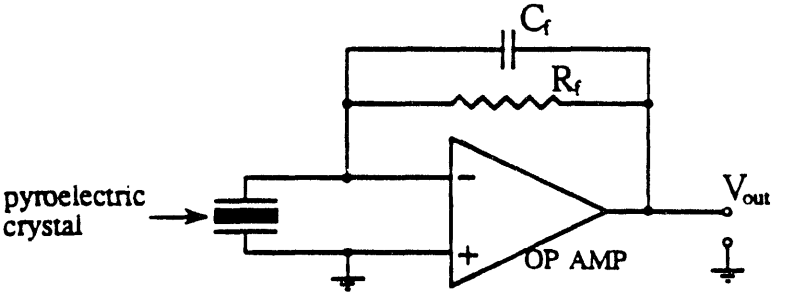

Figure 3.2: Circuit diagram of the current-to-voltage converter used with the pyroelectric detector.

3.2.2 The road to VUV pyrodetection

When used to detect light having a high photoelectric yield, the detector described in the previous section will produce a large spurious signal associated with the ejected photoelectrons. A rough calculation can show how dominant this effect can be. Assuming an incident power of 100 mW, the commercial pyrodetector, having a typical current responsivity of 1 μA per Watt, will generate 0.1 μA of pyroelectric current. Suppose now that the incident light is mainly composed of 800 Å (15.5 eV) photons. We therefore need 4×10^{16} photons/sec hitting the detector in order to get 100 mW of power. If we then take a photoelectric yield (defined here as the number of electrons ejected per incident photon) of 10% for the 800 Å photons, we arrive at a "photoelectron current" of 640 μA, which is more than 3 orders of magnitude greater than the pyroelectric current.

A universal curve of the VUV photoelectric yield of highly polished metals is given in figure 3.3. Almost all metals that have been exposed to air for some

time follow this curve to within 30% in the wavelength range displayed [84]. As will be shown later, the radiation produced by a MS discharge is concentrated in the 500–900 Å region and therefore has a high photoelectric yield.

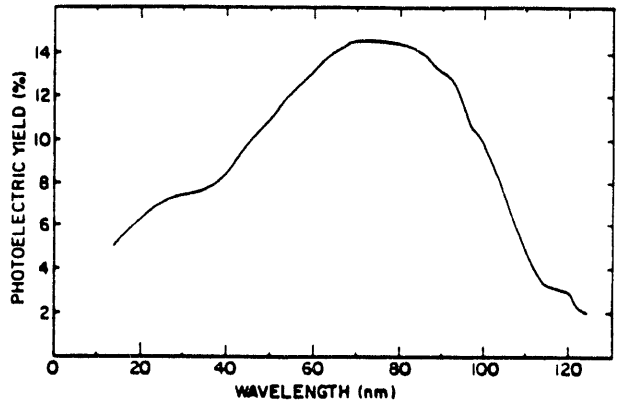

Figure 3.3: Typical photoelectric yield of metals in the 150–1250 Å range.

To prevent the photoelectrons from generating a spurious signal just by coming off the front electrode, it is obvious that this electrode must be grounded (i.e. connected to what serves as ground for the detector electronics). The charge of secondary electrons is then immediately drained to ground and does not contribute to the output voltage. This is also necessary if part of the incident power comes from charged particles.

A schematic of the setup used when the commercial pyrodetector was first tried in MS is shown in figure 3.4a. The front electrode was grounded and an iris was placed just above the crystal surface to control the amount of incident radiation. As stated before, this arrangement produced a very large spurious signal. This signal could have been mistaken for a real thermal signal if not for

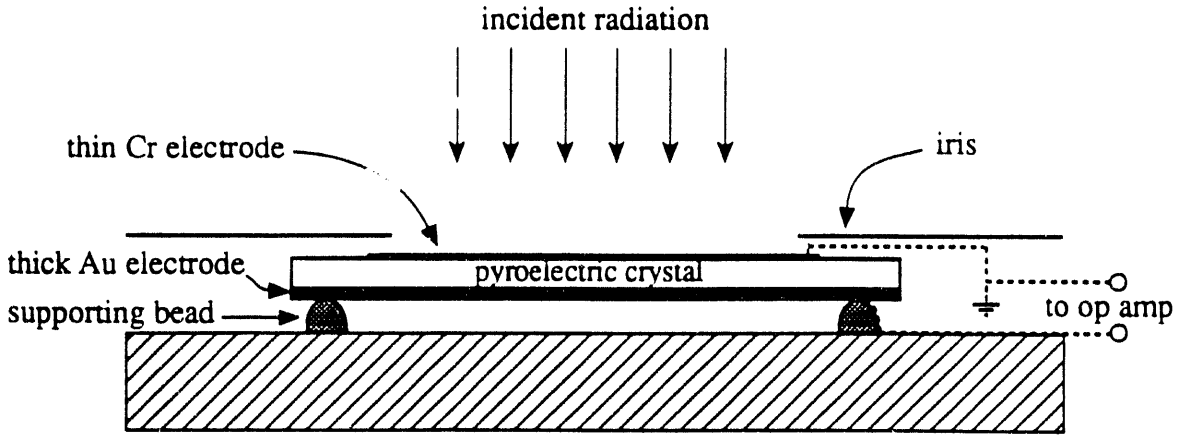

Figure 3.4(a): Detector configuration using an unmodified commercial pyroelectric detector.

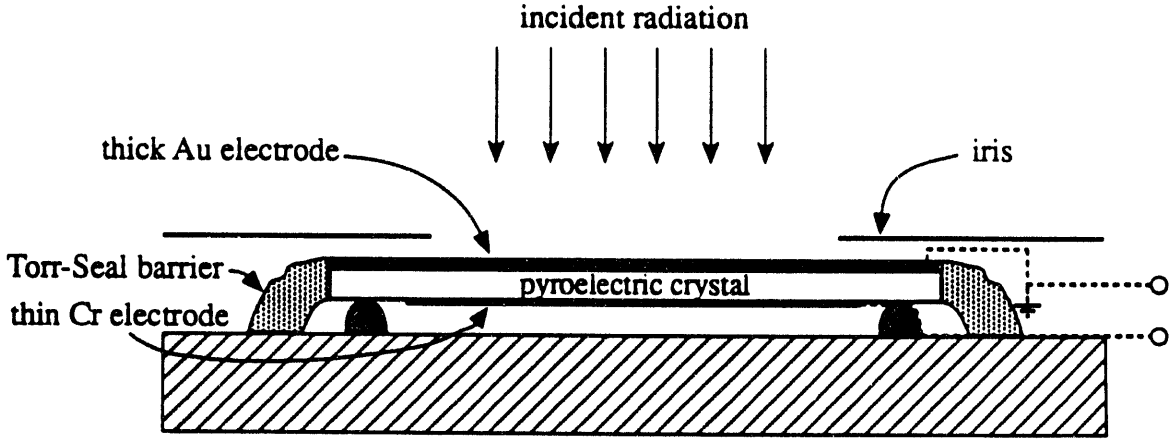

Figure 3.4(b): Configuration of the pyroelectric detector used in MS.

its excessive amplitude and wrong polarity. A biased grid placed just in front of the detector could reverse the signal polarity and change its amplitude, indicating that charged particles, most probably secondary electrons, were still affecting the signal. Similar behavior from pyroelectric detectors used in fusion devices has been mentioned in the literature [85,86], but the precise source of the problem was not identified.

A series of tests and modifications on the commercial detector showed that the spurious signal was in fact still entirely caused by the high photoelectric yield of VUV light and the many ways photoelectrons could affect the output signal even with the front electrode grounded. The design of the detector was modified and the final configuration, used for all the bolometric measurements in MS, is shown in figure 3.4b. It is basically the standard commercial pyrodetector described earlier but with the $LiTaO_3$ crystal flipped over, i.e., the crystal is mounted so that the thick gold electrode is now the grounded electrode facing the radiation. Additionally, the underneath of the crystal is "sealed" by a barrier of Torr-Seal filling the space between the substrate and the edges of the crystal. A thin layer of silver print paint is applied over this barrier and is kept at ground potential. Finally, the conductive paths on the substrate surface (making the connection between the back electrode and an outgoing pin) are all covered with Torr-Seal. The iris, placed just above the crystal in the figure, is in fact put directly on top of the Torr-Seal barrier and its diameter (2.75 mm) is a bit smaller than the diameter of the back chromium electrode. Note that the TO5 housing has to be sliced open (this was done on a lathe) to get the close access needed for these modifications.

The modified design stops 3 main processes: light, possibly on multiple reflections, or photoelectrons hitting the back electrode (which is the signal electrode), the conductive supporting beads or the electrical paths on the substrate, and generating a photoelectric current picked up by the operational amplifier; light or photoelectrons hitting sections of the crystal front surface not covered by an

electrode and depositing charge in (or removing charge from) the pyroelectric material; and light or photoelectrons going through the front electrode (or light ejecting electrons from the front electrode into the crystal) and, again, affecting charges in the crystal. The 2 μm thick gold electrode is 200 times thicker than the Cr electrode and will stop all but the most energetic photons, which make a very small fraction of the incident energy and have a low photoelectric yield anyway.

The elimination of the photoelectric spurious signal was confirmed primarily by observing that the output was not affected by a biased grid for grid voltage values that would previously alter the signal dramatically. The signal should in fact be affected slightly because the energy carried away by ejected electrons (which can be repelled back to the electrode with a negatively bias grid) will reduce the heating rate of the detector. This effect was too small to be observed within the normal shot-to-shot variations in MS. Energy loss from ejected electrons will be discussed further in the next section. An additional test was made with a detector modified in the way shown in figure 3.4b but with a much thicker front electrode made of silver print paint. The time response of this detector was slowed down to about 200 μs by the long heat transfer time between the electrode and the $LiTaO_3$ crystal. When used in MS, the output signal looked like a low-pass filtered version (with a RC time of $\sim$ 200 μs) of the signal obtained by the modified pyrodetector with the gold front electrode. A spurious signal caused by photoelectric effects would not have been affected by the slower thermal response time and would have looked the same with the two modified detectors. Finally, some measurements were made with a thin-metal-film bolometer [87] that agreed with the pyroelectric detector measurements. This bolometer was not used extensively in MS because of its slow time response ($\sim$ 150 μs), its poor signal-to-noise ratio and its uncertain calibration.

In general, the front electrode thickness needed to suppress a photoelectric spurious signal depends on the radiation spectrum of the source whose power

is to be measured. In some applications, energetic electrons contribute to the incident power and their possible transmission through the front electrode has to be considered. If fast response is desired, rapid heat transfer from the front electrode to the pyroelectric material is necessary and the smallest acceptable value for the electrode thickness should be used.

In the case of the modified detector of figure 3.4b, the thicker front electrode increases the response time τ_{th} of the sensitive element (the $LiTaO_3$ crystal and its two electrodes) to [88]:

$$\tau_{th} \approx \frac{\rho c_p x^2}{K} \approx \frac{(2\mu\text{m})^2}{1\ \text{cm}^2/\text{sec}} = 40ns$$

where ρ, c_p, K and x are the gold electrode density, specific heat, thermal conductivity and thickness, respectively. So even with the thicker front electrode, the pyrodetector still has the potential of being very fast. τ_{th} is so small in fact that for the radiation measurements in MS, the response time of the detector, including its external circuit, is instead limited by the need to use large R_f to obtain sufficient sensitivity, and the high end of the flat frequency bandwidth is determined by $(R_f C)^{-1}$, where C is the parallel capacitance of the sensitive element (72 pF for the particular detector used) and external circuit (a few pF). Still, even with the largest R_f used, this response time was never more than a few μs for the measurements made on MS. Also, since the capacitance of the sensitive element and the thickness of the $LiTaO_3$ crystal were unchanged by the modifications made, the responsivity and response time of the commercial pyrodetector and of its modified version are, for a given amount of **absorbed** power, exactly the same in practice.

3.3 The use of pyrodetectors in MS

• Calibration

The current responsivity R_i of the commercial detector is 0.5 μA per incident Watt when using a cw He-Ne laser (the laser beam is chopped at a frequency within the flat frequency bandwidth of the detector). The variation from detector to detector is 5% .

At the laser wavelength of 6328 Å, 44% of the incident power is absorbed by the sensitive element[82]. So the current responsivity can be given more generally as:

$$R_i = 1.14\ \mu\text{A per Watt absorbed}$$

with a 5% accuracy. Since the commercial and modified pyrodetector have the same responsivity (per Watt absorbed) when they are operating within their flat frequency bandwidth, the calibration of the modified pyroelectric detector used in MS is given by the R_i value shown above. Note that the same detector was used for all the measurements. The measured responsivity can be compared with the one calculated from the crystal physical properties given in the manufacturer's literature. For $LiTaO_3$, ρ=7.45 g/cm^3, c_p=0.43 J/g°C and p=0.019 μC/cm^2°C at 20 °C. So for a crystal thickness of 50 μm, the theoretical responsivity, as given by i/P_i in equation (3.1), is 1.19 μA per Watt absorbed, which is in very good agreement with the measured value.

A knowledge of the reflectivity of the gold front electrode as a function of wavelength is essential for broadband measurements. For its application in MS however, the pyrodetector is assumed to absorb 100% of the incoming radiation because the reflectivity of the gold electrode is very low at the wavelengths where MS radiates most of its power (500–900 Å). This reflectivity is in fact lower that what can be found in the literature for gold because the gold electrode is not a polished, shiny and perfectly flat surface. The side of the $LiTaO_3$ crystal

onto which the gold is evaporated is not finely polished (whereas the opposite side, covered with the thin Cr electrode, is) and the absorption coefficient of the resultant coating is higher than for a smooth gold surface. For example, the gold electrode absorbs about 35% of the incident radiation at 6328 Å, which is 10 times the value obtained by a gold coating applied on a well polished substrate. Further confirmation of the very low electrode reflectivity in the VUV range was obtained by observing that the detector's output did not change during the months it was used in MS (when observing the same plasma volume in the same conditions) while its reflectivity decreased by 50% at 6328 Å during the same period. The reflectivity decreased in the visible because, like the walls of the vessel, the gold electrode got covered by a thin layer of the impurity elements that get blasted out of the discharge on each shot. The fact that a change in reflectivity caused by this "plasma coating" had no effect on the signal output when observing VUV light implies that the absorption coefficient of the detector was already very high in the VUV. So an extra advantage of the modified commercial detector is that an additional coating especially made to obtain a flat spectral response (like a "gold black" coating [89,90]) was not needed. These coatings increase the response time and are sometimes fragile.

• **Corrections to the signal output**

Three aspects of the bolometric measurements will be considered here: the energy of secondary electrons, the thermal droop of the detector and the temperature dependence of the pyroelectric coefficient.

i) The heating rate of the sensitive element is reduced by the energy carried away by secondary electrons. The photoelectric yield of the front electrode represents an upper limit to the loss since not all of the photon energy goes into the kinetic energy of the electron. Furthermore, an electron released within the volume of the gold electrode loses energy by multiple collisions before reaching the surface. Photoelectrons are thus released with a wide spread of energy even for radiation

of fixed energy [91]. Finally, the photoelectric yield of an unpolished surface, like the gold electrode of the pyrodetector, is lower than the one of a polished surface because most photoelectrons produced within crevices are recaptured by the metal before they can escape. Samson has measured a fractional loss to photoelectrons of 2% for radiation at 584 Å incident on gold black, and no loss at 1216 Å [92]. When a biased grid was used to repel the photoelectrons back to the electrode during tests with the modified detector, no observable change above the shot-to-shot variation was seen in the signal output. So for the measurements in MS, the energy loss due to photoemission at the detector surface is small, and no correction was made to account for this effect.

ii) The thermal droop of the detector determines the low end of its flat frequency bandwidth: $\omega_{low\ end} \sim \tau^{-1}$ where τ is the detector thermal time constant. Both the commercial and the modified pyrodetector have a τ in the hundreds of milliseconds, and since MS discharges last less than a millisecond no correction for the thermal droop was necessary. The larger heat loss at the crystal edges (from their contacts with the Torr-Seal barrier) for the modified detector is not enough to affect τ significantly, and this extra heat loss is also partly compensated by the reduced amount of heat going in the supporting beads now that these are not touching the highly thermally conductive gold electrode.

iii) The Curie temperature of $LiTaO_3$ is 620 °C. At around 20 °C, its pyroelectric coefficient p increases with temperature at a rate of 0.18% per °C . When the detector was used with a collimator, the temperature change of its sensitive element was small and the temperature dependence of p could be neglected. When used without collimation (as a 2π detector), the power incident on the sensitive element was high and the temperature change of the crystal could reach 20 °C by the end of the discharge. But since this means that the variation in the pyroelectric coefficient was less than 3.6% for most of the discharge, the temperature dependence of p was neglected here in comparison with the other sources of error associated with the 2π detector measurements (these have

nothing to do with the pyrodetector itself and will be discussed later). A thicker $LiTaO_3$ crystal could be used to reduce the temperature change of the sensitive element if this was an important source of error; the resulting lower sensitivity would not be a problem since the incident power is very large. Note finally that the small increase in the signal output due to the temperature dependence of p is partially cancelled out by the signal reduction due to photoemission energy losses.

- **Setup for collimated measurements**

A simplified drawing of the arrangement used for the collimated bolometric measurements is presented in figure 3.5. Because MS discharges create an electromagnetically noisy environment, the detector is double shielded with the copper tubing outer shield running all the way to the screen room (which contains the data acquisition system) where it is grounded. Pickup noise was reduced to a negligible level, and this could be checked regularly by closing a gate valve installed between the detector and the radiation source.

The "electronics" section of figure 3.5 is simply the external circuit shown in figure 3.2. The high-output-current operational amplifier used (PMI's model OP-50EY) can drive $\pm$ 50 mA into 50 Ω loads and was ideal for amplifying small signals for transmission through the long RG-58 cable. Its slew rate is about 2.5 $V/\mu s$, which is not very fast but perfectly acceptable here because an overall time resolution of 2–4 μs is sufficient for the measurements on MS. The Op Amp is powered by rechargeable batteries placed close to the electronics. The detector draws very little current between shots and the batteries were rarely recharged. Before being digitized in the screen room, the output signal goes through a low-pass filter having a RC time of 2 μs. Note that for low R_f, corresponding to small gains, the Op Amp has to be compensated to prevent oscillations.

The RG-58 cable bringing the signal to the screen room is in fact inserted in

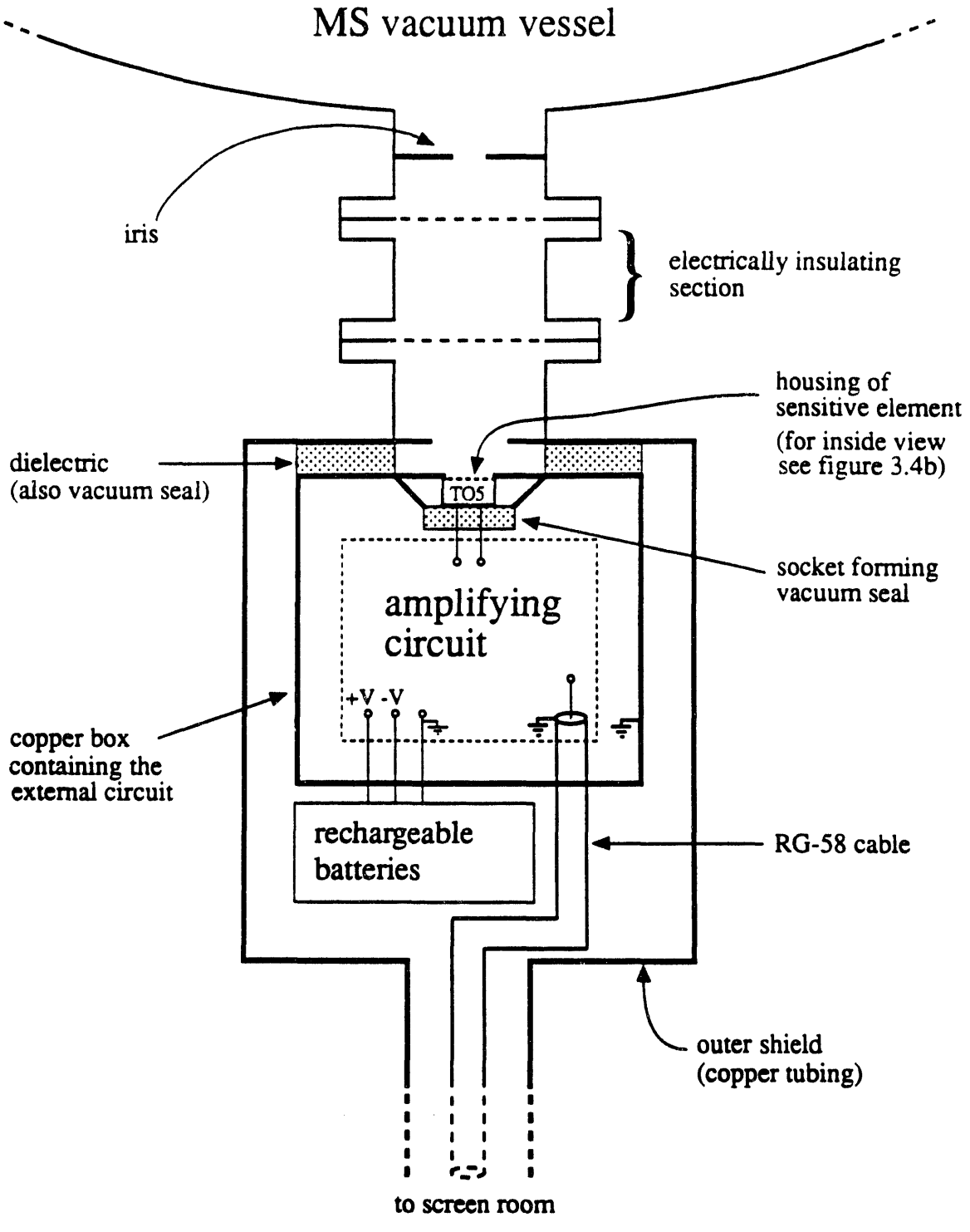

Figure 3.5: Collimated pyroelectric detector setup. The drawing is not to scale.

a braid (which is taped over to prevent contact with the outer shield), so the setup is partly triple shielded. The feedthrough section insulating the outer shield from the vacuum vessel prevents ground loops and problems associated with the voltage jump of the vacuum vessel during a discharge.

Finally, the detector's viewing angle is defined by 2 irises, one of which being very close to the front electrode (inside the TO5 housing), as shown in figure 3.4b.

- **2π pyrodetector setup**

In this arrangement, the detector is flush with the machine wall and is not collimated. The shielding is the same as the one for the collimated setup in principle but the construction is different because both the inner and outer shield have to fit into a small midplane port. The need to partially enclose the detector with the outer shield limits the (solid) angle of view to a little less than 2π but the detector still sees the entire plasma.

Originally, the outer shield was to be insulated from the vessel wall and it was covered with an insulator to prevent arcing. This approach had to be abandoned though and in the final arrangement the detector and its shields are floating with the machine walls, and the signal is transmitted to the screen room through a current monitor. This current monitor transforms the Op Amp current to a voltage read by the digitizer.

Besides greatly reducing the possibility of arcs associated with the voltage jump of the machine upon firing, the floating setup also eliminated a large spurious signal caused by a ground shift at the detector: early in the I_z discharge, a blast of charged particles hit the vessel walls and the detector front electrode, charging them up; in the non-floating setup, this front electrode was grounded directly to the screen room but the resistance of the signal cable braid was too large to keep the detector ground and screen room ground at the same potential and this ground shift was appearing as a spurious signal at the digitizer. The

false signal was greatly reduced when the RG-58 cable was replaced by a RG-8 cable (whose braid has a lower resistance) but it was still too large and the floating setup was adopted. As with the collimated setup, it is possible to block the detector's view and check for pickup noise, in this case with a blind that can be manipulated from an adjacent chamber port. The contribution to the output signal from the energy of the incident particles is negligible at the location chosen for the detector. More on this in chapter 4.

The current monitor used (model 2877 from Pearson Electronics) provides 0.5 volt/A when terminated in 50 Ω, has a risetime of 2 ns and a droop of 0.2%/μs. In practice, the risetime is increased to about 1 μs because the signal wire of the detector is wrapped 10 times around the current monitor to improve its sensitivity. The droop is corrected numerically at each time point by multiplying the integral of the signal (up to that point) by a constant and adding the result to the raw signal. The constant is chosen so that the corrected signal goes to zero at the end of the spheromak decay.

Chapter 4

Results from collimated bolometry and VUV spectroscopy

After being presented separately in sections 4.1 and 4.2, the collimated bolometric and spectroscopic measurements are combined in the third section to give some of the most important results of this chapter: the evaluation of the spheromak electron temperature T_e and the determination of the impurity content (as a percentage of the electron density) of the plasma. To obtain these results, the VUV spectrometer was calibrated absolutely in the range 500–2300 Å with the use of the pyroelectric detector. As described in section 4.3, this calibration was only possible because: a) for the lines of sight used, the fraction of the radiated power due to particles hitting the detector is negligible; b) the plasma continuum emission is negligible; and c) most of the emitted radiation comes at wavelengths longer than 500 Å and could be detected by the normal incidence VUV spectrometer.

The measurements were made with the 2 glass annuli in place and in the following conditions (referred from now on as the "standard" conditions) :

- bias coils current at 400±15 A (bias B field is $\sim$ 0.5 kG in the center)
- I_z bank consisting of 5 modules charged at 12 kV
- I_z current in the 600–630 kA range
- reversal bank consisting of 7 modules charged at ±4 kV

- reversal current in the 240–260 kA range
- deuterium working gas
- dynamic puff corresponding to pressures of 1.5 to 3.0 mTorr when puff is allowed to become static.

These conditions were chosen because they generate a reasonably well behaved spheromak for which interferometry and magnetic probe data are available. A very limited amount of measurements were made outside this standard operating regime because the MS project was ending and time became a constraint after the development of the pyrodetector had finally been completed. The selected set of operating conditions in no way restricts the general conclusions presented here.

4.1 Bolometry

4.1.1 Midplane scan

The midplane scan data were taken with the collimated pyrodetector setup (described in section 3.3) attached to a sliding seal moving in the z=0 plane. The plasma is viewed along chords that are parallel to each other and perpendicular to the symmetry axis of the spheromak. A total of 17 chords are available in the midplane (covering the top and bottom sections of the machine) with an inter-chord separation of 3.84 cm. The holes in the machine wall allowing these chordal views are normally used for the interferometry diagnostic.

Figure 4.1 shows the line averaged radiated power for 9 of the midplane chords. Each curve is an average of many shots. An array of detectors would obviously have been useful for these measurements since the discharge conditions may change slightly during the time the pyrodetector is moved from the lowest to the

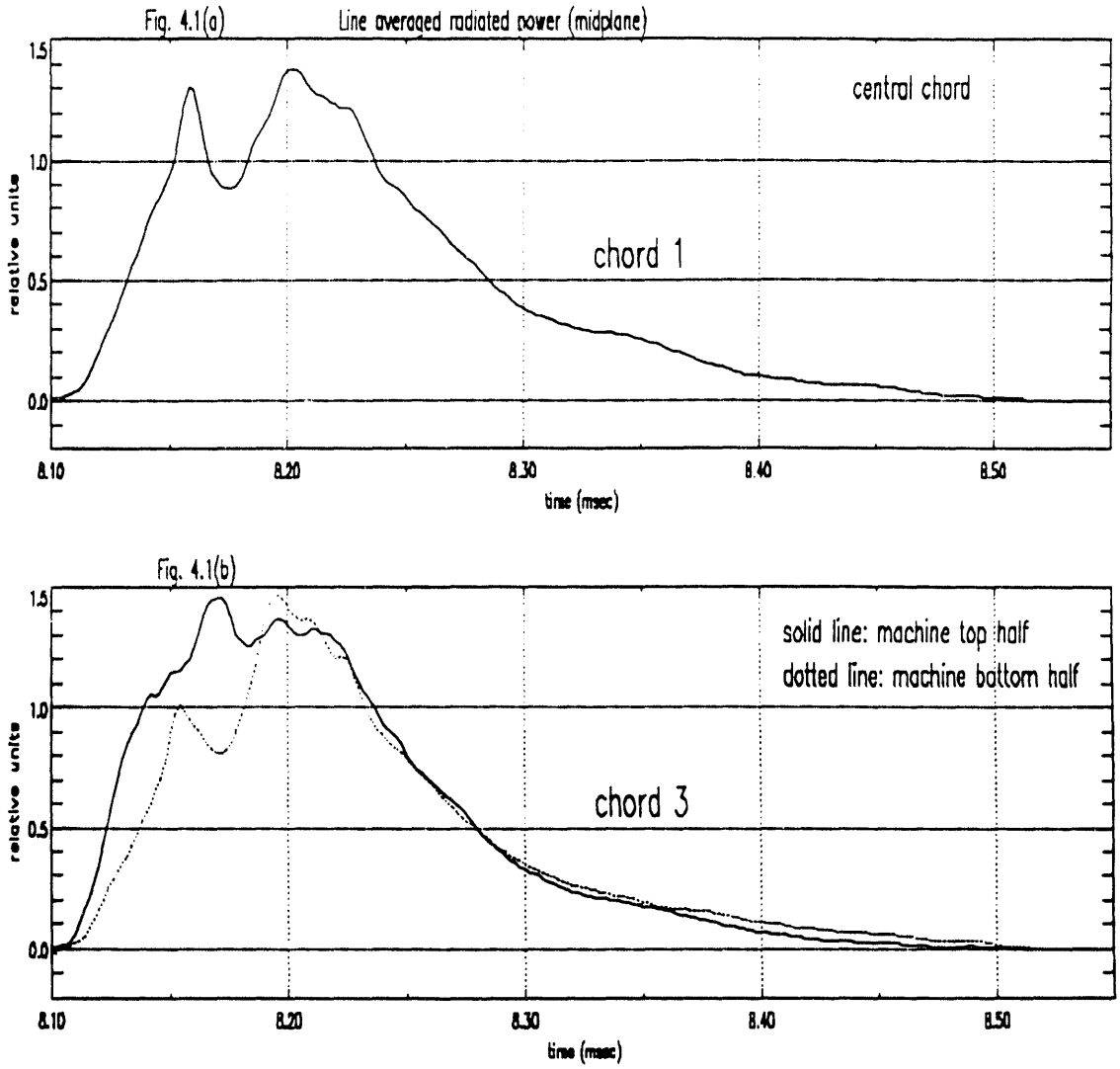

Figure 4.1 (a) to (e): Line averaged radiated power in the midplane as measured by the collimated pyroelectric detector. Each curve is an average of 4 to 7 shots. The plots show the measurements made in the top and bottom half of the vessel. Figures 4.1(c) to 4.1(e) appear on the next page. The time at which the spheromak is fully formed is indicated in figure 4.1(e).

Fig. 4.1(c) Line averaged radiated power (midplane)

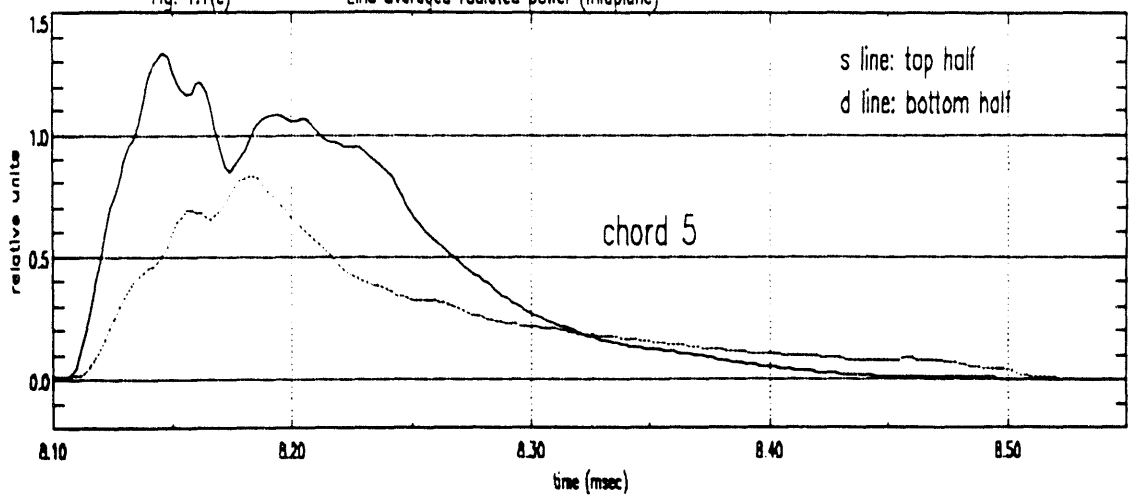

Fig. 4.1(d)

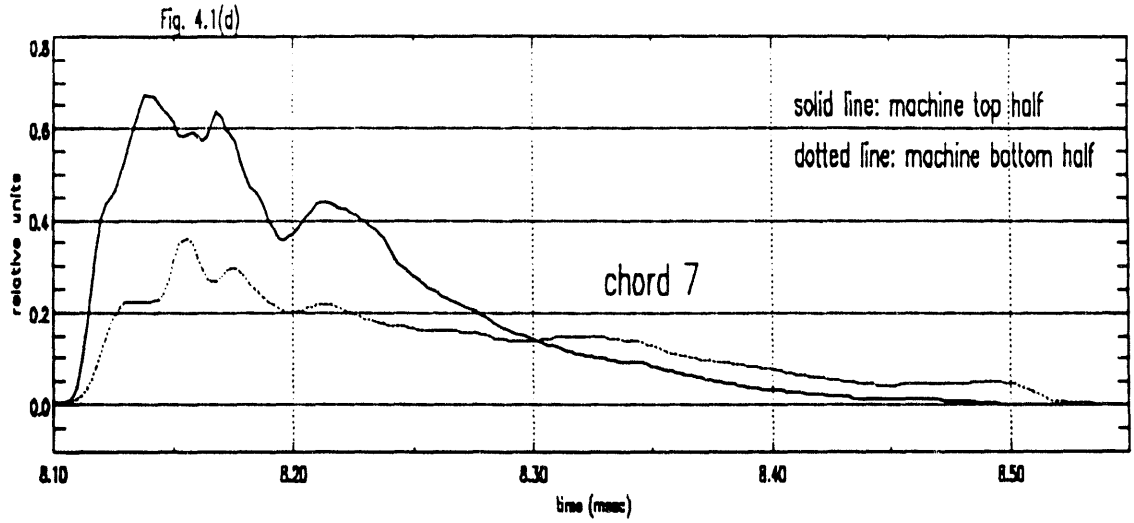

Fig. 4.1(e)

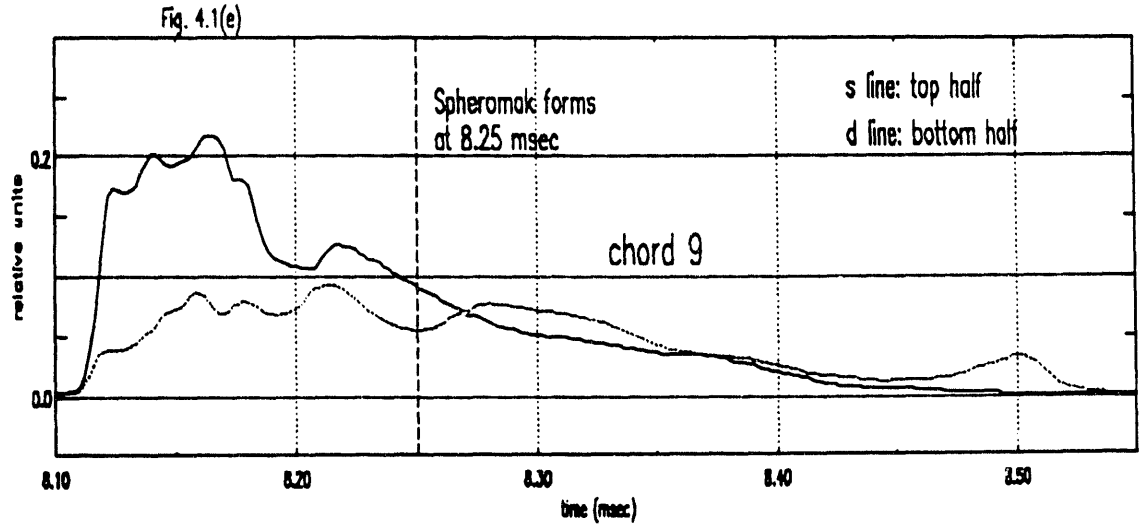

highest chord. Nevertheless, the degree of confidence in the data presented in figure 4.1 is very high because many midplane scans were done, starting from the lowest, middle or highest chord, and they all gave the same results. Magnetic probe measurements also showed a high degree of shot-to-shot reproducibility.

The most striking feature of the outer chords data is the asymmetry between the power radiated from the top and bottom half of the machine. During the formation phase, the top half radiates more, while after 8.30 ms more power is radiated from the bottom half (the spheromak forms at $\sim$ 8.25 ms). A possible explanation for these observations is that the spheromak initially forms a few cm off-center toward the machine top and then shifts (partly due to forces exerted by the confinement field and the figure-8 coils) toward the bottom where it eventually crashes. Evidence of this crash can be seen in the radiated power increase at 8.50 ms for the bottom chord 9. In any case, the radiated power asymmetry probably has it ultimate source in the up-down asymmetry of the reversal coils, which have their feeding points at the machine bottom. For example, the pre-ionization generated by the reversal breakdown (with the help of microwaves) could occur preferentially in the top half, affecting the I_z current paths and producing the immediate onset of the radiated power asymmetry that can be seen clearly in the data for chords 5 to 9. Since the radiation coming from the discharge is mainly impurity line radiation, small differences in electron temperature (especially in the range 1–15 eV) and impurity content between the top and bottom half of the machine early in the discharge could easily lead to an asymmetry in the radiated power. Because it is so reproducible from shot to shot, it is natural to associate the radiated power asymmetry to the only constant asymmetry in the experiment, which is the reversal coils asymmetry.

The slightly off-center formation of the spheromak and its subsequent shift toward the machine bottom can be observed with the magnetic probes. Midplane B probes were not used during the bolometric measurements (they would have obstructed the view of the pyrodetector) but careful examination of older

data taken under similar conditions [24] shows that the spheromak was forming (t=8.25 ms) a few cm above the machine symmetry axis and was then slowly shifting down, crossing the symmetry axis at around 8.30 ms, in agreement with the bolometric measurements. So it can be seen that a very simple and non-intrusive way of observing plasma shifts is to use collimated bolometers viewing opposite edges of the plasma. Information about an up-down asymmetry was not available from the interferometry diagnostic because the interferometer was never used in the machine top half.

Some other features of the collimated pyrodetector data, like the dip in the signal around 8.175 ms for chord 1, will be discussed in later sections. The midplane bolometric measurements were primarily made to obtain a radial profile of the plasma emissivity, and this is presented next.

4.1.2 Inversion of midplane chord data

Strictly speaking, the pyrodetector does not view the plasma along chords of very small and constant cross-section the way an interferometer does. The 2 collimating irises define a viewing cone whose cross-section increases as one moves away from the detector along the line of sight. For a plasma of uniform emissivity however, the contribution to the detector signal will be the same for any fixed section along the line of sight, as in the case of true chordal measurements. This is simply because the average solid angle subtended by the detector, as seen by a particular plasma section, decreases in proportion with the increase in the plasma volume observed as one moves away from the detector [93].

For a plasma of non-uniform emissivity, the collimated measurements will be a good approximation of true chordal measurements in the limit of a narrow viewing cone, and the power received at the detector for chord j will then be

given by [94]:

$$P_j = \frac{A_1 A_2}{4\pi D^2} \int_j e(r)\, dl, \tag{4.1}$$

where A_1 and A_2 are the areas of the collimating irises separated by a distance D, l is the line of sight path length coordinate across the plasma, and $e(r)$ is the volume emissivity, assumed to depend only on the cylindrical coordinate r in the midplane. In its application on MS, the sensitivity of the pyrodetector was high enough that the chords could be well collimated (the diameter of the viewing cone was about 1.5 cm at midpoint along the line of sight) and equation (4.1) was used as the starting point for the inversion.

The method used to invert the chord data is similar to the one described in reference 54. The plasma is divided into 6 concentric shells. The volume emissivity $e(r)$, assumed to be isotropic, is given a linear dependence on r for each shell. The integral in equation (4.1) can then be performed analytically and a set of linear equations representing all the chordal measurements is obtained. In the final step, this system of equations, which would take the form $(P)=(M)(e)$ in matrix notation, is inverted by a least square fit routine.

Because of the slight up-down asymmetry of the plasma during most of the discharge, one should ideally find the plasma symmetry axis for each time point and start the inversion from there. However, the emissivity radial profiles calculated by always keeping the z axis as the symmetry axis had the same general characteristics (with some differences in overall amplitude) when any of the pyrodetector midplane scans, top or bottom, was used for the raw data, and the final inversion results were obtained by averaging the data taken in the top and bottom half of the machine for each corresponding chord and using these as raw data. The inversion is then expected to give the plasma emissivity most accurately for the middle section of the plasma associated with the line of sight of chord 1. This is going to be useful when the bolometric and spectroscopic results will be combined since the VUV spectrometer has a view of this middle section.

The results of the inversion at 4 different times are presented in figure 4.2. An example of the error associated with the inversion process can be seen in the graph for t=8.22 ms. The error bars were obtained by running the inversion program many times with standard deviation noise added to the raw data; the range of inverted profiles obtained from the propagation of that noise gives the uncertainty in the emissivity at each radial point.

The dominant feature of the emissivity profiles is the inward motion of the emissivity peak during the discharge. Impurity line radiation is highest in regions of high T_e (provided that the radiation barriers for the dominant impurities have not been passed), high n_e and high impurity concentration. The radially inward motion of the emissivity peak is associated with two main phenomena: the inward motion of the main (I_z) current sheet from the beginning of the discharge to about 8.23 ms [13,24], and the on-axis peaking of the electron density late in the discharge [95].

During the formation phase, the location of the I_z current sheet determines the regions where large ohmic heating occurs and where the resultant higher T_e is responsible for strong impurity line radiation. The I_z annular sheet starts (t=8.10 ms) at around 20–25 cm, which is the midplane position of the field lines intersecting the electrodes, and slowly moves inward, reaching the symmetry axis at about 8.23 ms. The transition wave occurs in a coherent and reproducible manner and is thought to be a consequence of the plasma seeking a lower energy state (rather than being a z-pinch effect) while reacting to a large reverse current induced on axis at the beginning of the discharge [13]. While the peak of the emissivity profile moves inward during the formation phase, it does not strictly follow the main current sheet as the amount of impurity line emission varies also in relation with the induced plasma currents and with the radial profiles of the impurity concentration and electron density.

After the spheromak has formed, the I_z current drops rapidly, T_e is more uniform throughout the plasma volume, the impurity influx is reduced, and the

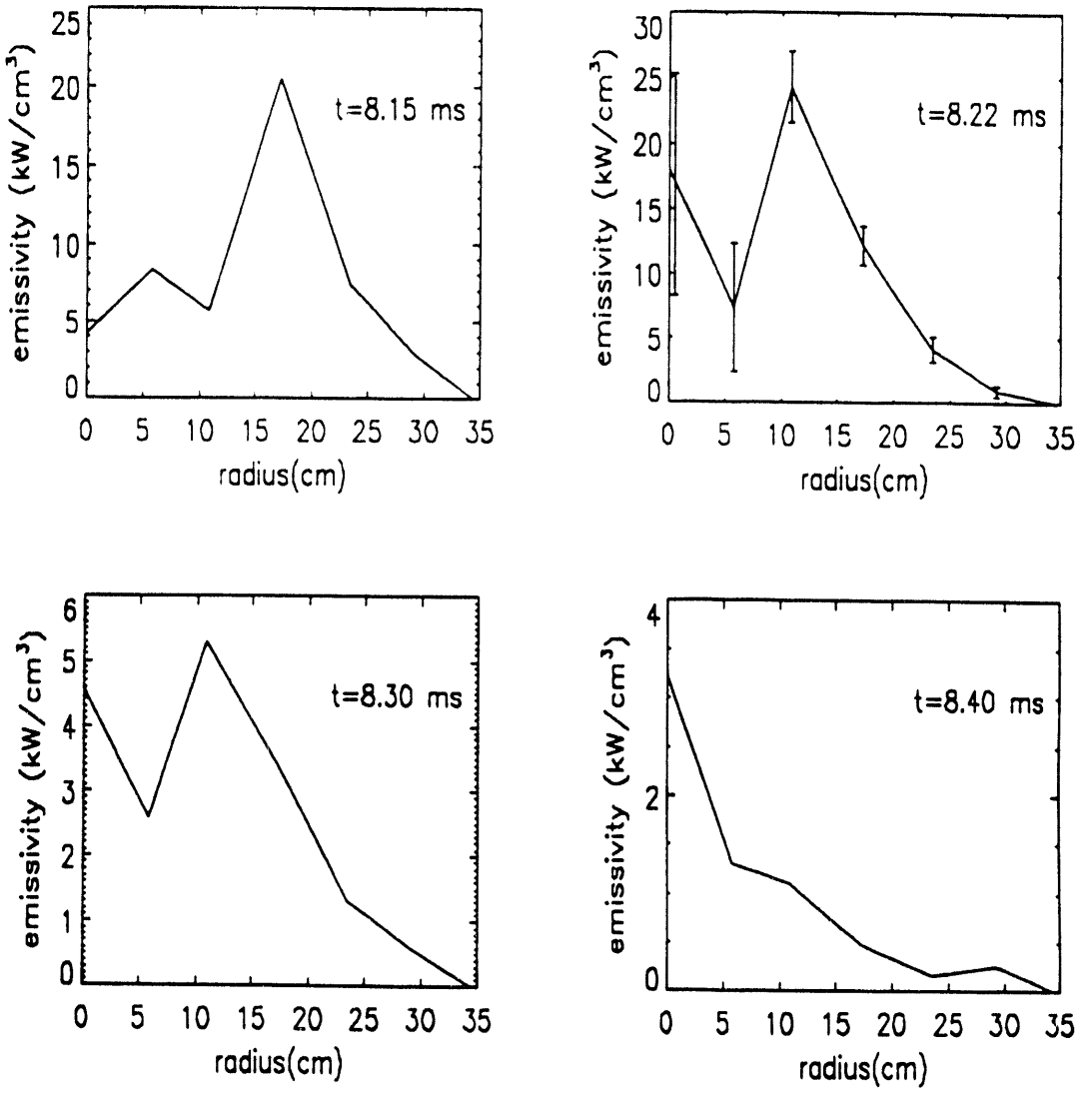

Figure 4.2: Radial profile of the plasma emissivity in the midplane at 4 different times.

emissivity profile becomes a reflection of the electron density. The emissivity peak past 10 cm for t=8.22ms, the double peak seen at 8.30 ms and the central peaking at 8.40 ms all correspond to peaks in the electron density at the corresponding times [95]. The central peaking of the density profile is associated with the shrinking of the plasma during the decay phase.

The various processes affecting the shape and time evolution of the emissivity profile have only been touched briefly here but the main point was to establish the legitimacy of the midplane bolometric measurements so that they can be used with confidence later in this chapter.

4.1.3 Nature of the plasma radiation

In order to use the VUV spectrometer measurements in combination with the bolometer data, it is important to know the particle contribution to the pyrodetector signal and to have an idea of the plasma radiation spectrum. The particle contribution, expected to come mainly from impact of charge-exchange neutrals on the detector, was investigated by placing the midplane collimated pyrodetector at different distances from the machine with the same line of sight. The part of the signal due to particles will be delayed when the detector is placed farther away from the plasma. As it turned out, the signals obtained with the pyrodetector placed at 2 locations separated by 1.08 m were identical within the shot-to-shot fluctuation. With the 3 μs time resolution of the pyroelectric detector, a simple calculation shows that unacceptably high particle energies would be needed to explain this result if particles contribute to the signal. For midplane collimated bolometry then, there is no significant particle contribution to the radiated power. This was further confirmed by observing that the pyrodetector signal looked similar with or without filters (the filters used,i.e., Al foil, LiF and quartz windows, all blocked particles).

Filters were also used to characterize the plasma radiation spectrum. A quartz window with a sharp cut-off at 1600 Å showed that over the discharge duration 98% of the radiation was at wavelengths shorter than 1600 Å.The contribution from above 1600 Å was lowest during the formation phase (higher T_e) and highest at the end of the discharge (lower T_e). Thin-foil aluminum and carbon filters helped determine that a few percent of the radiation was at wavelengths below 300 Å, beyond the detection capability of the normal incidence VUV spectrometer. More details on the plasma radiation spectrum will be given in the following sections.

Finally, it is worth mentioning that bremsstrahlung radiation, with its $n_e^2 T_e^{1/2}$ dependence, is completely negligible for the low temperature MS plasma in comparison with line radiation. Continuum emission resulting from recombination processes is in fact more important than bremsstrahlung radiation for the MS plasma but, as discussed later in this chapter, it is still negligible compared to line radiation.

4.2 VUV spectroscopy

Spectroscopic data were taken with a 1 meter normal incidence monochromator (McPherson model 225, which has a 15° angle between entrance and exit beams). A tripartite Al grating, blazed for 800 Å with 1200 lines/mm, was used. For most of the measurements, the spectrometer was viewing the plasma, which is optically thin for the emission lines considered, along the middle midplane chord (chord 1). Additional data were taken with the spectrometer looking at the outside edge of the spheromak along chord 8, and also looking at an I_z electrode.

The emission lines present were identified through a broad survey in the range

300–2300 Å. This was accomplished by replacing the exit slit assembly by a film holder (Kodak X-ray film type 101 was used), by scanning the developed film with a microdensitometer to put the data in a more usable form, and finally by matching the microdensitometer traces with emission lines listed in wavelength tables [96,97]. Note that the high resolution of the grating forced the survey to be done in steps of ~350 Å. For each 350 Å wide spectrum, and with an entrance slit width of 30 μm, one MS discharge was enough to reveal the strongest lines. If a few shots were taken on the same piece of film for each 350 Å step, hundreds of lines could be seen and identified in the range 450–2300 Å. The wavelength region from 300 to 450 Å was investigated by replacing the Al grating (whose reflectivity is very low below 450 Å) with a platinum grating. No important line was present in this range. There are strong lines around 200 Å but they could not be observed with the normal incidence spectrometer. These were studied with the pyrodetector used with filters, as mentioned before.

The elements which had emission lines identified in the broad survey are oxygen, nitrogen, fluorine, carbon, silicon, aluminum and copper. A few lines of hydrogen, deuterium, iron, nickel and chromium (the last two originating from the Nichrome foil covering the reversal coils) were also present but their contribution to the total radiated power was negligible. A small number of weak lines that could not be identified are believed to be emanating from tungsten (the I_z electrode tips are made of Elkonite, a copper-tungsten alloy), whose radiation spectrum is not well known in the low ionization stages likely to be observed in MS.

The light ions O, N and C get into the discharge by processes involving low energy detachment of molecules adsorbed on the machine walls and other surfaces. Probable sources of the impurity elements are: the reversal coils Teflon tape insulation for F (and C); the ceramic (Alumina) insulation of the I_z electrodes for Al (and O); oil vapors from the pumping system for C (and H); the Elkonite electrode tips and figure-8 coils for Cu; and the glass annuli for Si (and O).

Wavelength (Å)	Ion	Transition
507.39, 507.68, and 508.18	O III	$2s^22p^2(^3P)^*$–$2s2p^3(^3S^\circ)$
525.795	O III	$2s^22p^2(^1D)$–$2s2p^3(^1P^\circ)$
553.33 to 555.26 (4 lines)	O IV	$2s^22p(^2P^\circ)^*$–$2s2p^2(^2P)$
597.82	O III	$2s^22p^2(^1S)$–$2s2p^3(^1P^\circ)$
599.60	O III	$2s^22p^2(^1D)$–$2s2p^3(^1D^\circ)$
608.40 and 609.83	O IV	$2s^22p(^2P^\circ)^*$–$2s2p^2(^2S)$
624.62, 625.13, and 625.85	O IV	$2s2p^2(^4P)$–$2p^3(^4S^\circ)$
629.73	O V	$2s^2(^1S)^*$–$2s2p(^1P^\circ)$
656.12, 656.87, and 658.33	F III	$2s^22p^3(^4S^\circ)^*$–$2s2p^4(^4P)$
676.12 to 679.21 (5 lines)	F IV	$2s^22p^2(^3P)^*$–$2s2p^3(^3D^\circ)$
684.99 to 686.33 (4 lines)	N III	$2s^22p(^2P^\circ)^*$–$2s2p^2(^2P)$
702.33 to 703.85 (4 lines)	O III	$2s^22p^2(^3P)^*$–$2s2p^3(^3P^\circ)$
758.68 to 762.00 (6 lines)	O V	$2s2p(^3P^\circ)$–$2p^2(^3P)$
765.15	N IV	$2s^2(^1S)^*$–$2s2p(^1P^\circ)$
787.71, 790.11, and 790.20	O IV	$2s^22p(^2P^\circ)^*$–$2s2p^2(^2D)$
921.99 to 924.28 (6 lines)	N IV	$2s2p(^3P^\circ)$–$2p^2(^3P)$
977.02	C III	$2s^2(^1S)^*$–$2s2p(^1P^\circ)$
989.79, 991.51, and 991.58	N III	$2s^22p(^2P^\circ)^*$–$2s2p^2(^2D)$
1031.92 and 1037.61	O VI	$1s^22s(^2S)^*$–$1s^22p(^2P^\circ)$
1083.99 to 1085.70 (6 lines)	N II	$2s^22p^2(^3P)^*$–$2s2p^3(^3D^\circ)$
1174.93 to 1176.37 (6 lines)	C III	$2s2p(^3P^\circ)$–$2p^2(^3P)$
1206.51	Si III	$3s^2(^1S)^*$–$3s3p(^1P^\circ)$
1206.53	Si III	$3s3p(^1P^\circ)$–$3s3d(^1D)$

Table 4.1: Dominant impurity lines. An asterisk in a transition term denotes the ground configuration. The table continues on the next page.

Wavelength (Å)	Ion	Transition
1238.82 and 1242.80	N V	$2s(^2S)^*$–$2p(^2P^\circ)$
~1260.42	unknown	
1311.36	C I	$2s^22p^2(^1D)$–$2s^22p5d(^1F^\circ)$
1334.53, 1335.53, and 1335.71	C II	$2s^22p(^2P^\circ)^*$–$2s2p^2(^2D)$
1343.39	Si III	$3s3d(^3D)$–$3p3d(^3D^\circ)$
1345.64	Cu IV	$3d^74s(^5F)$–$3d^74p(^5G^\circ)$
1371.29	O V	$2s2p(^1P^\circ)$–$2p^2(^1D)$
1379.67 and 1384.13	Al III	$2p^63p(^2P^\circ)$–$2p^64s(^2S)$
1393.75 and 1402.77	Si IV	$2p^63s(^2S)^*$–$2p^63p(^2P^\circ)$
1411.59/1411.45	Cu IV/Ni IV	
1431.93/1431.95/1432.03	Al IV/Cu IV	
1443.02 and 1443.14	Cu IV	
1449.69	Cu IV	$3d^74s(^3F)$–$3d^74p(^3G^\circ)$
~1467.75	unknown	
1548.20 and 1550.77	C IV	$1s^22s(^2S)^*$–$1s^22p(^2P^\circ)$
1593.56/1593.75	Cu II/Cu III	
1605.77, 1611.81, and 1611.87	Al III	$2p^63p(^2P^\circ)$–$2p^63d(^2D)$
1628.29	Cu III	$3d^84s(^4F)$–$3d^84p(^4F^\circ)$
1642.21	Cu III	$3d^84s(^4F)$–$3d^84p(^4G^\circ)$
1670.79	Al II	$3s^2(^1S)^*$–$3s3p(^1P^\circ)$
1709.03	Cu III	$3d^84s(^4F)$–$3d^84p(^4D^\circ)$
1718.55	N IV	$2s2p(^1P^\circ)$–$2p^2(^1D)$
1854.72 and 1862.79	Al III	$2p^63s(^2S)^*$–$2p^63p(^2P^\circ)$
1935.84, 1935.86, and 1935.95	Al III	$2p^63d(^2D)$–$2p^64f(^2F^\circ)$
2135.38	Cu II	
2296.87	C III	$2s2p(^1P^\circ)$–$2p^2(^1D)$

The dominant impurity lines, responsible for almost all of the radiated power, are listed in table 4.1. Note that this list of important lines could only be made after the VUV spectrometer setup has been calibrated to determine its relative sensitivity as a function of wavelength (the procedure used will be described in the next section). The list also represents all the lines whose time evolution was later studied by placing a photomultiplier tube at the exit slit of the spectrometer. A number of lines are part of multiplets and these are grouped together in the left column of the table when the entire multiplet (not necessarily on the same shot) was observed with the PM tube. The highest ionization stages present are C IV, N V and O VI. The strongest lines are the resonance lines, as expected, but the list also contains a large number of "non-resonant" lines.

To study the time evolution of individual lines, the exit slit assembly was reinstalled on the spectrometer. The vacuum seal just in front of the exit slit consisted of a quartz window whose vacuum side (the side facing the slit) was covered by a thin layer of the fluorescent material sodium salicylate. A PM tube was then used to detect the visible light emitted by the sodium salicylate upon absorption of VUV light and transmitted through the window. The maximum intensity of fluorescence for sodium salicylate is at 4200 Å [98]. For each transition listed in table 4.1, the exit slit was opened wide enough to see the entire line (or the entire multiplet if it was tightly packed) and a few shots were taken to make sure that the spectrometer was adjusted precisely at the wavelength of interest and to check on the shot-to-shot reproducibility. Stray light and continuum emission were completely negligible.

Time-resolved spectrometer data for selected impurity ions are presented in figure 4.3. Again, the spectrometer sensitivity calibration has been used to plot the graphs shown here, and the intensity of the different emission lines can be compared directly. Early in time, the strongest lines are the O V line at 629.73 Å, the N V doublet at 1238.82 and 1242.80, and the O IV multiplet between 553.33 and 555.26 Å. These three transitions account for about 55% of the line averaged

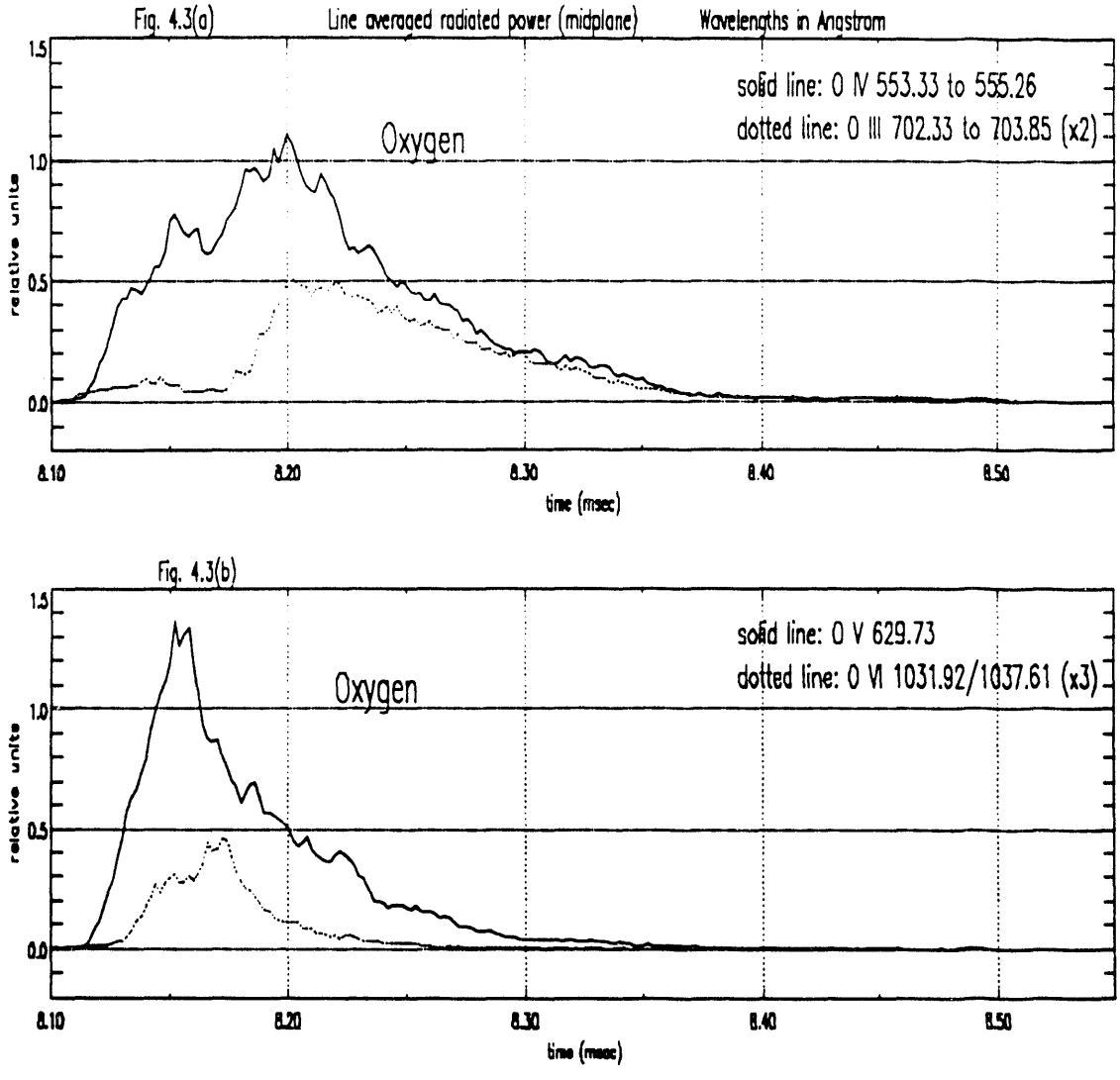

Figure 4.3 (a) to (h): Time evolution of the line emission (from selected transitions) for the major impurity species in MS. The VUV spectrometer view is through the center of the plasma along the midplane (chord 1). Figures 4.3(c) to 4.3(h) appear on the next two pages.

Fig. 4.3(c) Line averaged radiated power (midplane)

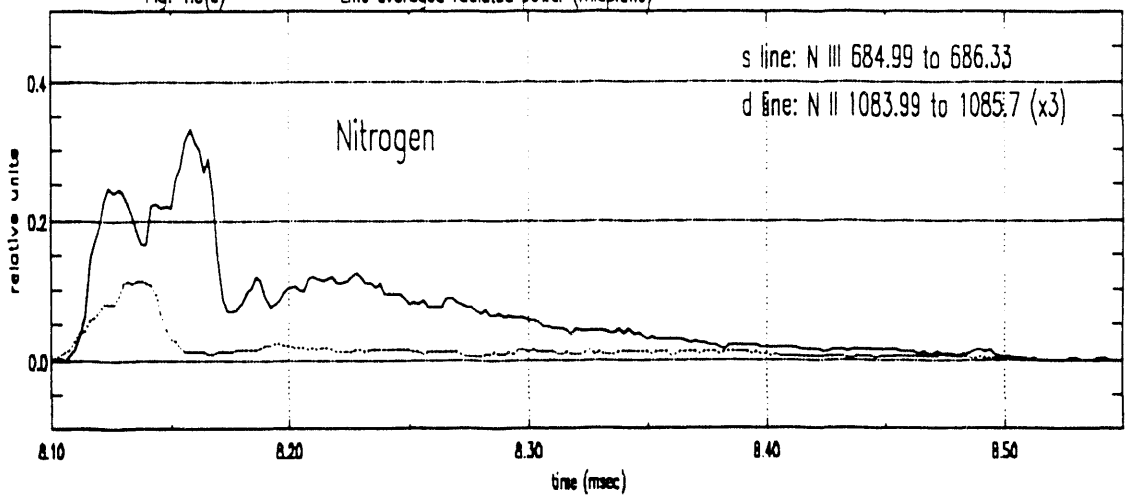

Fig. 4.3(d)

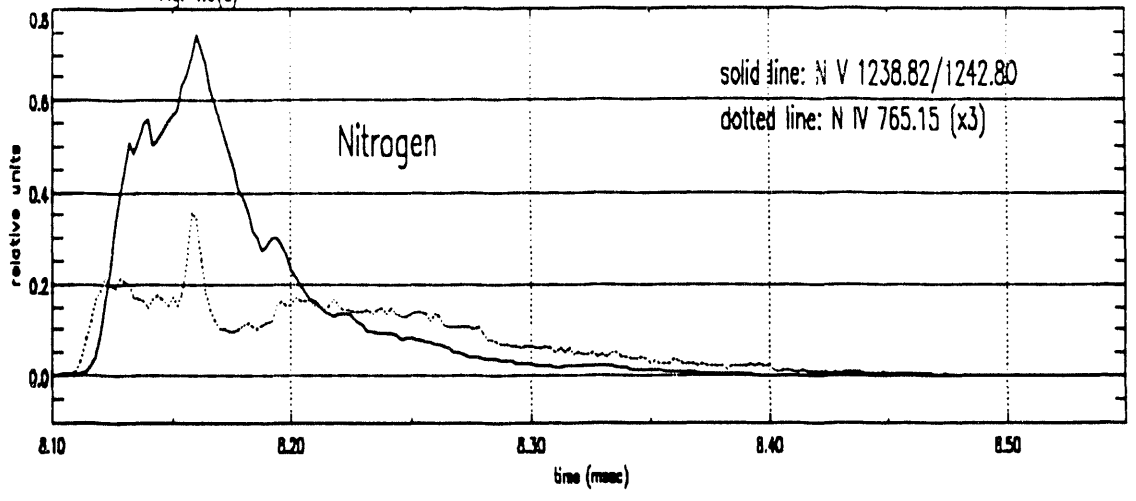

Fig. 4.3(e)

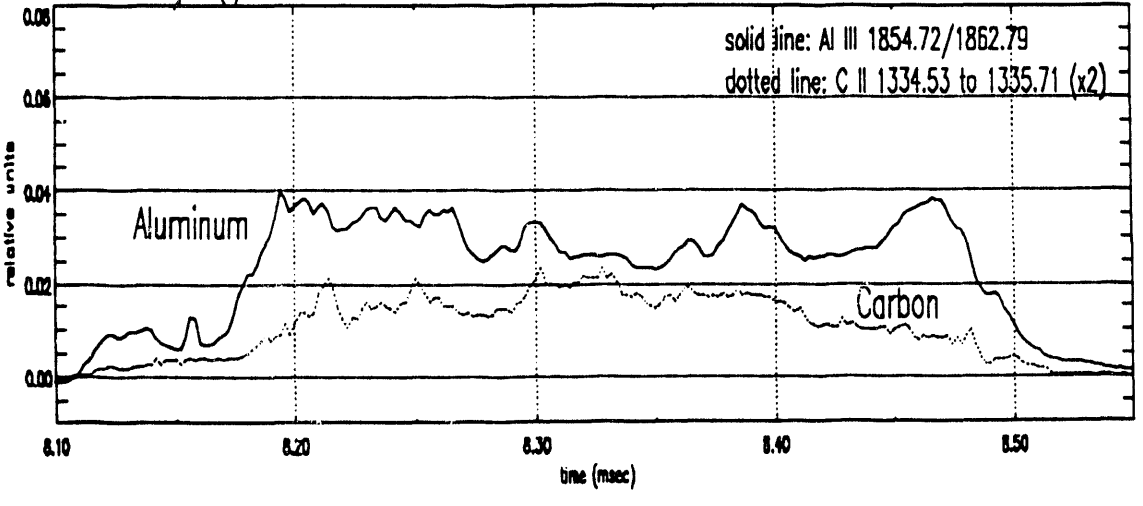

Fig. 4.3(f) Line averaged radiated power (midplane)

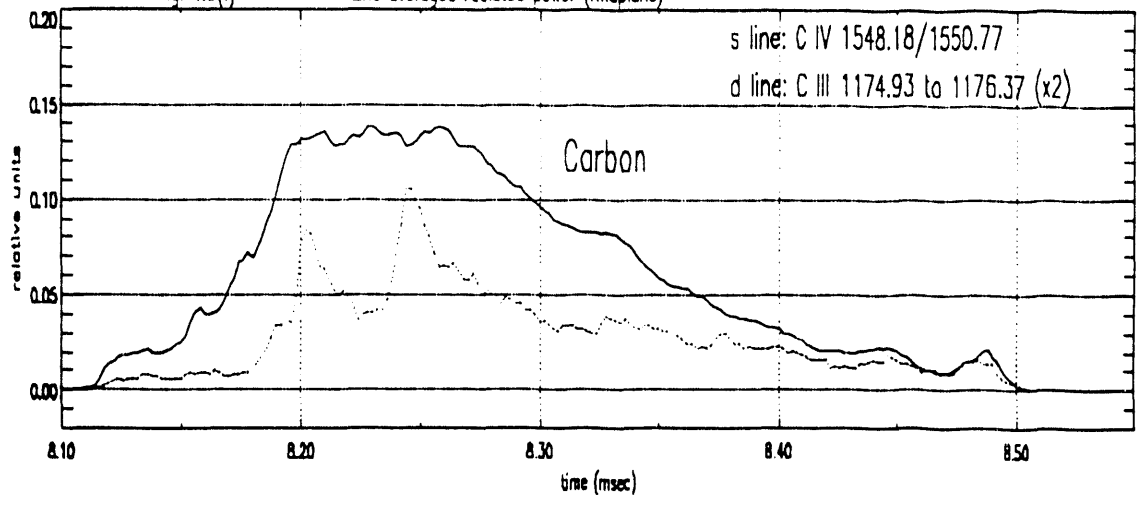

Fig. 4.3(g)

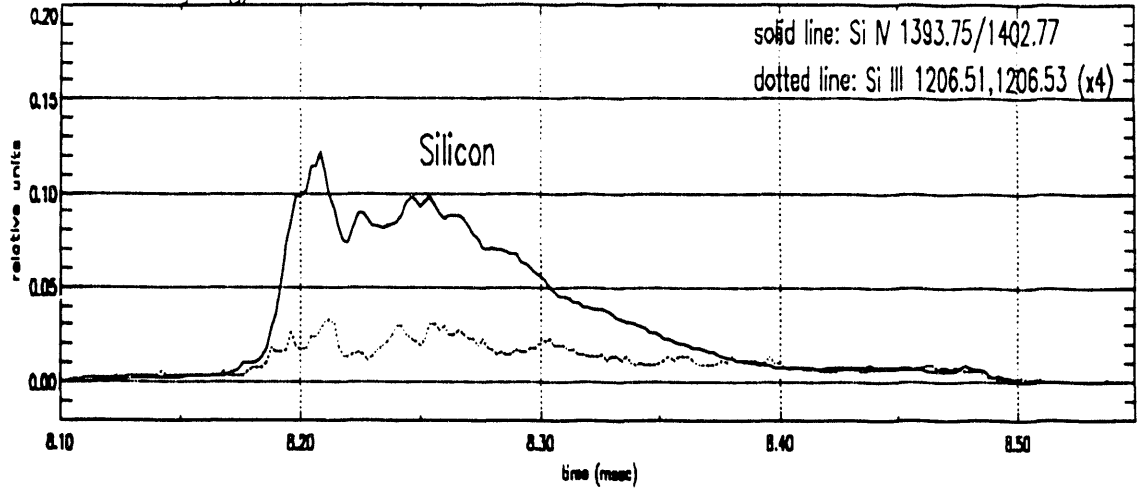

Fig. 4.3(h)

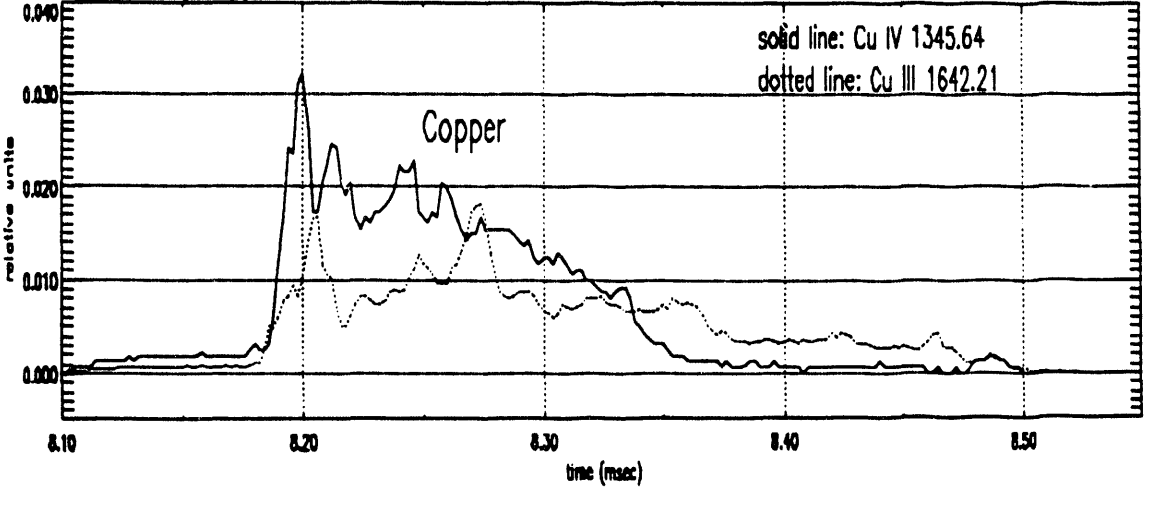

radiated power for chord 1 at 8.15 ms. Note that chord 1 line averaged measurements are representative of the whole plasma in the case of MS because the central region does not contribute disproportionately to the radiated power and the emissivity goes down at the plasma edges. When the plasma is viewed along chord 8, the time-resolved signals are similar to the ones of figure 4.3 except that the intensity ratios of different ionization stages indicate a slightly lower electron temperature.

The gradual rise of T_e after initiation of the discharge can be seen in the plots for oxygen (figures 4.3a and 4.3b) by looking at the leading edge of the curves for O IV, O V and O VI, which shows that the transitions of the different ionization stages get excited in succession (it is even more obvious for nitrogen). When T_e starts decreasing at ~8.17 ms, the O III lines get stronger.

While oxygen and nitrogen radiate strongly in the first 100 μs, the contribution from other impurity elements increases as time progresses. This phenomenon and other aspects of the impurity behavior will be discussed in more detail in the next section. The time-resolved spectroscopic data will also be used later to determine the temperature and impurity concentration of the spheromak plasma.

4.3 Combination of bolometric and spectroscopic data

4.3.1 Intensity calibration of the VUV spectrometer setup

The time-resolved spectroscopic data for chord 1 were all taken with the same entrance slit width and the same voltage on the PM tube. To determine the relative sensitivity of the spectrometer setup as a function of wavelength, the signals for all the important lines were added up and the resulting sum was

compared to the signal obtained with the pyrodetector viewing the exact same plasma region. The sum of lines was weighted at each wavelength associated with a line emission in order to obtain a match between the shape of the pyrodetector signal and the shape of the sum of lines curve. Those weights then define the spectrometer relative sensitivity as a function of wavelength. The good match obtained is shown in figure 4.4 where the sum of lines has been multiplied by an arbitrary factor to give the two curves the same overall amplitude. This procedure was only possible of course because a limited number of lines located in a wavelength range accessible to the spectrometer completely dominates the radiated power in MS. The flat spectral response of the pyroelectric detector in the VUV and the negligible particle contribution to its signal were also crucial. A plot of the relative sensitivity of the VUV spectrometer setup is given in figure 4.5.

Far from having been chosen arbitrarily to offer the best possible match, the weight values were based on published measurements relative to the reflectivity and efficiency of the Al grating [98,99], and to the quantum yield of sodium salicylate [98,100]. It is important to note that for this relative sensitivity calibration, only the relative wavelength dependence of the spectrometer setup components is needed. This is rather convenient since relative wavelength dependence is less affected by oxidation, contamination from oil vapors, etc. than absolute values of metal reflectivities and quantum yield of fluorescent materials. Furthermore, parameters such as the entrance slit width or the PM tube response curve as a function of wavelength (the fluorescent spectrum of sodium salicylate is independent of the exciting wavelength between 275 and 2537 Å [98]) do not enter into the calibration.

The Al grating and the sodium salicylate window were many years old and their characteristics were stable during the time needed for the measurements. When data from the literature on the reflectivity of "old" Al coatings and the quantum yield of "old" sodium salicylate were used directly to give the weights

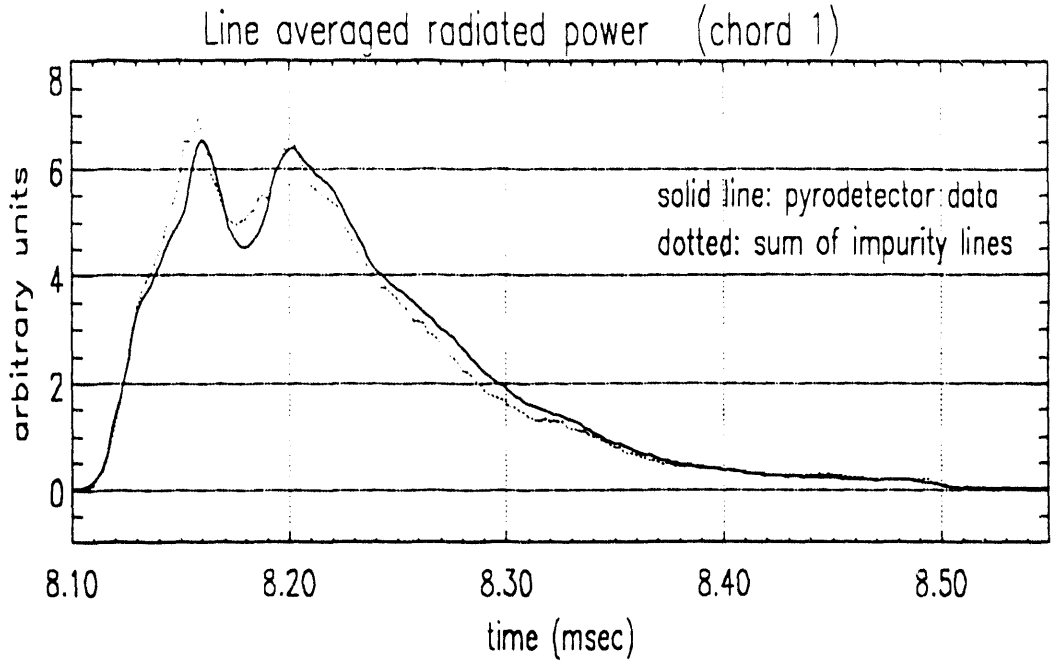

Figure 4.4: Comparison between the collimated pyrodetector signal and the curve obtained by summing up the VUV spectrometer signals from the strongest emission lines. The pyrodetector data is an average of 14 shots.

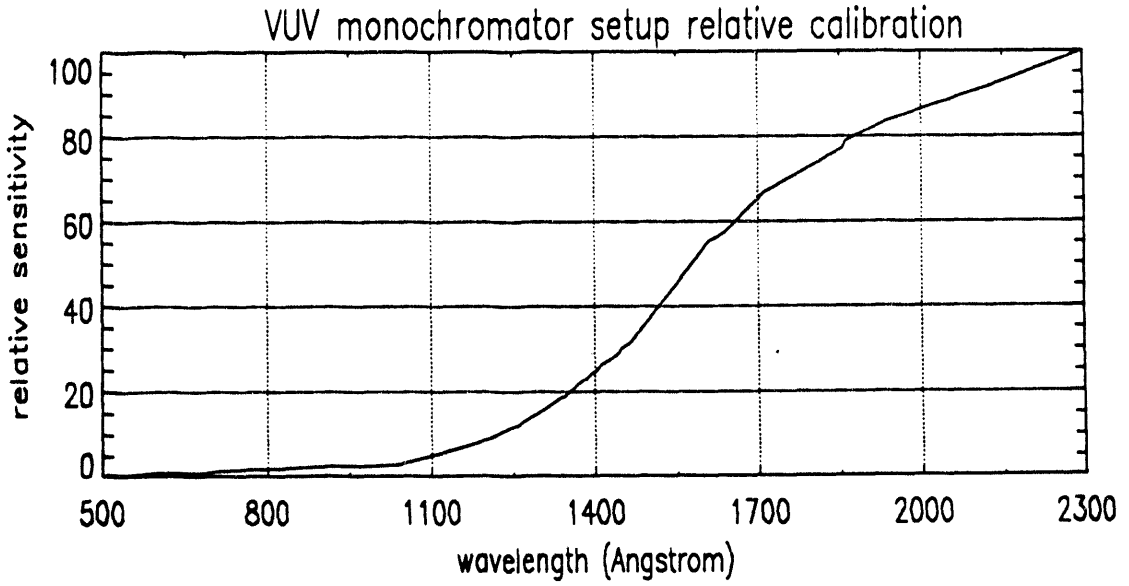

Figure 4.5: Sensitivity of the VUV monochromator setup as a function of wavelength. The effect of the sodium salicylate window is included.

in the sum of lines, the match with the pyrodetector signal was not quite as good as the one showed in figure 4.4. The histories of the grating and the fluorescent window used here are unique and obviously their characteristics may differ somewhat from similar old gratings and windows. To find out how the weights should be adjusted to improve the match, the sum of lines and the pyrodetector signal were compared in specific spectral regions with the use of filters. An 800 Å thin foil Al filter (transmitting from 170 to 800 Å) and a quartz window (transmitting above 1600 Å) were used separately with the pyrodetector and the resulting signals were compared with the numerically filtered sum of lines. By numerical filtration, we mean, for example, that only the lines below 800 Å were used in the sum of lines for the comparison with the Al filtered pyrodetector data, with values of transmission at different wavelengths given by the experimental transmission curve for an oxidized Al foil 800 Å in thickness [98]. The Al filter allowed the low wavelength weights to be adjusted and the quartz window took care of the longer wavelengths. The corrections needed on the initial weights were small and always done monotonically as a function of wavelength. In the end, the match between the spectrometer sum of lines and the pyroelectric detector signal was very good with the Al filter, the quartz window, and without filter for chord 1 (figure 4.4) and also chord 8.

The astute reader may be wondering at this point about the fate of the emission lines around 200 Å. Those lines were isolated from the pyrodetector signal with the use of filters, and added to the sum of lines before the weights were evaluated. The weight given to this group of lines was adjusted such that their contribution to the sum of lines was the same as the one for the pyrodetector signal (this contribution had a maximum value of 9% at 8.15 *ms*). Two thin film filters were used simultaneously to pick up the lines around 200 Å: a carbon film, 952 Å in thickness, transmitting below 500 Å and the 800 Å thick Al filter used before, which transmits between 170 and 800 Å. The Al filter is needed because the carbon film has a second transmission band above 1000 Å.

Those two filters then select lines in the range 170–500 Å. But, as mentioned before, no important line was observed between 300 and 500 Å when the Al grating was replaced by a platinum grating. Furthermore, measurements made in experiments comparable to MS (in electron temperature and impurity line radiation) have shown that the dominant lines below 500 Å are oxygen lines around 200 Å [101]. These are, for O V, the lines at 172.17 and 185.74 Å, the triplet between 192.75 and 192.91 Å (this is expected to be the strongest line), the triplet between 215.04 and 215.24 Å, and the line at 220.35 Å; for O IV, the resonance doublet at 238.36/238.57 Å. Starting from the filtered pyrodetector signal amplitude, the contribution of these lines to the total signal is determined by the transmissivity of Al and C around 200 Å [98,102].

The procedure just described for the VUV spectrometer intensity calibration is somewhat laborious and unsuitable for most plasma fusion experiments but the rewards are the wide wavelength range covered and an accuracy superior to what could have been obtained by using the atomic branching ratio method [103,104]. The discrepancy remaining between the two curves in figure 4.4 can be attributed mostly to shot-to-shot fluctuations since only one or two shots were taken for each emission line while the pyrodetector signal is an average of many shots taken on a different day. Once the calibration is completed, it will not change as long as the same old and stable grating and fluorescent window are used, and one can concentrate on the spectral region or lines of most interest. The VUV spectrometer can also be calibrated absolutely by using the known sensitivity of the pyrodetector and by comparing the slightly different viewing geometries of the two instruments.

4.3.2 Concentration of impurities and electron temperature

In order to relate line emission to ion densities, it is essential to determine

what type of equilibrium governs the plasma atomic physics. For the dominant lines emitted in MS, it is sufficient to use the coronal model [105], i.e., all upward transitions are collisional (since the radiation density is low) and all downward transitions are radiative (since the electron density is low) and instantaneous. In the case of ions belonging to isoelectronic sequences without highly populated metastable levels, the ground-state density is practically equal to the total ion density, and the power density P_j (W/cm^3) emitted as line radiation by the ion Z for the transition j is [106]:

$$P_j = 1.6 \times 10^{-19} n_e n_z Q_j(T_e) \Delta E_j \tag{4.2}$$

where n_z is the density of an ion of charge Z in cm^{-3}, $Q_j(T_e)$ is the temperature dependent electron-impact excitation rate coefficient in cm^3/sec, and ΔE_j is the excitation energy in eV.

In computer simulations of plasma radiated power, the line radiation is calculated from equation (4.2) by summing up the contributions from the strongest resonance transitions, assuming some total impurity ion density and using an ionization model to determine the distribution of ionization stages. In situations where the plasma lifetime or the particle confinement time are short (like in MS), impurity transport and recycling must be taken into account, and one must use a coronal non-equilibrium treatment [95,107]. An accurate evaluation of the radiated power is then difficult to obtain. Fortunately, for the inverse calculation, i.e., the evaluation of ion densities from the line radiation, there is no need to choose between an equilibrium and a non-equilibrium model, as the density of the different ionization stages is given directly by equation (4.2).

A self-consistency check can be made at this point between these computer simulations of coronal plasma and our bolometric and spectroscopic data. In a simulation involving oxygen, nitrogen, carbon and iron, Breton *et al* [106] have shown that line radiation completely dominates over radiation from radiative recombination, dielectronic recombination and bremsstrahlung for T_e below 50 eV.

At these low temperatures, the contribution from charge-exchange (CX) recombination radiation has also been found to be negligible compared to line radiation resulting from electron-impact excitation [107,108] because the CX cross-section reaction rates, which go as $q^{3/4}$, are small for the low ionization stages present in these conditions. Furthermore in the case of MS, the neutrals do not penetrate deep into the plasma in regions containing the highest ionization stages because of their short mean free path ($\sim$ 1 mm) in the high density plasma. For these reasons also (and considering the low energy of the ions at the plasma edge, where most CX interactions occur), the particle contribution to the total radiated power from CX neutrals is small in MS. Charge-exchange processes will be discussed in more detail in the chapter about the spheromak power balance. The results just mentioned based on a coronal model of the plasma are then in agreement with our measurements, which indicate that line radiation can account for all of the energy received by the collimated pyroelectric detector.

Coming back to equation (4.2), we note that to calculate the impurity concentration of a given ion at a specific location, we need to know the power density of an emission line from that ion along with the electron density and temperature (to get the excitation rate coefficient), all for the plasma region chosen. To illustrate the steps taken in evaluating these quantities, the details of the calculation for the O V resonance line at 629.73 Å for t=8.15 ms are now presented. The calculations will be done for the plasma region around r=17 cm in the midplane. This is the region of maximum emissivity in terms of the total radiated power at 8.15 ms, as seen in figure 4.2.

- **power density**

Using the sensitivity calibration of the VUV spectrometer, the O V line at 629.73 Å is found to contribute 25.6% of the total radiated power for chord 1 and 24.9% for chord 8 at t=8.15 ms. Ideally, spectroscopic data would be available for all chords and an inversion could be performed to give the contribution of

this O V line at r=17 cm. In this case though, it is clear that this contribution is about 25% since the peak emissivity region around r=17 cm dominates the pyrodetector signal for chord 1 and, furthermore, chord 8 data show that the relative contribution from this transition does not change much throughout the plasma volume. The power density around r=17 cm is then taken to be 25% of the total emissivity at that location (~17 kW/cm^3). So for the O V line at 629.73 Å, P=4.25 kW/cm^3 around r=17 cm at t=8.15 ms.

• electron density

The line averaged density for chord 1 was shown in figure 2.6. Those interferometer data were taken concurrently with the spectroscopic data and give a line averaged density of 3.0×10^{14} electrons/cm^3 at 8.15 ms. No midplane interferometer scan was done during our measurements and use will be made of older inverted density results obtained under similar conditions but without the glass annuli [95]. These inverted data show a large density beyond r=35 cm because of the large I_z curren g behind the reversal coils along the vessel walls and because the electron ated in central regions could reach this outside location by moving along the magnetic field lines around the reversal coils during the formation phase. These currents were not present during our measurements and we will therefore only consider the radial density profile inside r=35 cm in these older data. At 8.15 ms, it is seen that n_e peaks around r=17 cm and that this peak value is about 2.2 times the chord 1 averaged density. Using this peak to line-averaged ratio with our chord 1 density data, we obtain an electron density of 6.6×10^{14} cm^{-3} around r=17 cm at 8.15 ms. The uncertainty on n_e is about 30% , twice the uncertainty on the power density P.

• excitation rate coefficient

The electron-impact excitation rate coefficient for oxygen are taken from Phaneuf *et al* [109]. The electron energy distribution is assumed to be Maxwellian. Taking an electron temperature of 25 eV at 8.15 ms, the coefficient Q for our

O V resonance line (ΔE=19.7 eV) is equal to 2.4×10^{-8} cm^3/sec, with a quoted accuracy of 20% . The T_e value of 25 eV was selected a posteriori, being the temperature most consistent with the oxygen distribution among its different ionization stages for a coronal plasma [106-108]. This distribution was determined from equation (4.2) using resonance lines emitted by the different ionization stages. The temperature was chosen so as to be slightly higher than the one associated with a coronal plasma in equilibrium since in a non-equilibrium plasma like MS, a larger proportion of the lower ionization stages will be found at a given temperature. Carbon lines were also used for the determination of T_e and the range of temperatures consistent with the distribution of both O and C was very narrow. Note that for the oxygen line at 629.73 Å, the excitation rate coefficient is not strongly dependent on T_e in the range 20–200 eV (the Q curve reaches its peak in the middle of that temperature range).

Using equation (4.2) with the above derived data, we obtain:

$$n_{O\,V} = 8.5 \times 10^{13} ions/cm^3$$

for the O V concentration around r=17 cm at 8.15 ms, with an uncertainty of 40% . This represents a staggering 12.8% of the electron density, dissipating any doubt about the high impurity content of the plasma.

Similar calculations were made for other O V lines and for lines from other oxygen ionization stages. By summing the contribution of the different stages, the total oxygen concentration is obtained. Absolute concentrations and percentages of electron density for oxygen at four specific times are presented in table 4.2, which also include the results for nitrogen, carbon, aluminum and silicon. Excitation rate coefficients were taken from calculations documented in references 109 to 114. Because of the large uncertainty in the data (40% for the impurity concentration and 50% for the percentage of n_e), trends are more significant than absolute magnitudes. Note that even if the results are given for a localized region for each time, they are representative of most of the

		t=8.15 $msec$	t=8.22 $msec$	t=8.30 $msec$	t=8.40 $msec$
T_e		**25 eV**	**17 eV**	**14 eV**	**10 eV**
n_e (cm^{-3})		6.6×10^{14}	11×10^{14}	6.0×10^{14}	6.5×10^{14}
radius		17 cm	12 cm	12 cm	0.0 cm
O	n_O (cm^{-3})	1.6×10^{14}	2.4×10^{14}	9.0×10^{13}	4.2×10^{13}
	% of n_e	**24%**	**22%**	**15%**	**6.5%**
N	n_N (cm^{-3})	7.3×10^{13}	2.2×10^{13}	1.1×10^{13}	1.0×10^{13}
	% of n_e	**11%**	**2.0%**	**1.9%**	**1.6%**
C	n_C (cm^{-3})	2.6×10^{12}	1.1×10^{13}	1.1×10^{13}	1.4×10^{13}
	% of n_e	**0.4%**	**1.0%**	**1.8%**	**2.2%**
Al	n_{Al} (cm^{-3})	2.6×10^{11}	9.9×10^{11}	9.6×10^{11}	3.3×10^{12}
	% of n_e	**.06%**	**.14%**	**.24%**	**.75%**
Si	n_{Si} (cm^{-3})	1.3×10^{11}	2.2×10^{12}	1.8×10^{12}	1.0×10^{12}
	% of n_e	**.03%**	**0.3%**	**0.45%**	**.23%**

Table 4.2: Electron temperature and concentration of selected impurities in regions of peak plasma emissivity in the midplane.

plasma based on the fact that the spectrometer data for chord 8 were in general showing the same lines with the same intensity ratios as the chord 1 data (the difference between these two sets of data can be largely explained by a slightly lower average temperature for the plasma seen along chord 8).

Looking at the column for t=8.15 $m$sec in table 4.2, one observes that the total impurity concentration is very high during the formation phase at around 35% of the electron density. The contribution of species not included in the table is small at that time. Since the average charge state of the impurity ions is between +3 and +4, most of n_e can be accounted for by electrons coming from the ionization of impurities during the formation phase of MS. In fact, the number of impurity ions is of the same order as the number of deuterium ions (D_2 is the filling gas) during that time. The source of the abnormally high density in the Maryland Spheromak is then seen to be an extremely large impurity content. Note that hydrogen (excluded from our definition of impurity here) also contributes to the dilution of the deuterium plasma even if its contribution to the total radiated power is negligible.

Shortly after the spheromak formation at 8.30 $m$sec, the total impurity content is still high at about 21% of n_e (where Cu and F are assumed to contribute a few percent), resulting in a radiation dominated plasma. The total impurity concentration continues to decrease during the decay phase and the total number of electrons in the plasma goes down. The high value of n_e in a small volume around r=0 cm at 8.40 $m$sec is partly due to a shrinking of the plasma.

A measure of Z_{eff} based on the plasma bremsstrahlung emission could have provided some of the basic information just discussed but it would not have given the more detailed histories of the various impurity elements available here.

4.3.3 Impurity behavior

As can be seen from table 4.2, the concentrations of oxygen and nitrogen, initially very high, decrease during the discharge while, in general, the concentration of other species increase with time. These trends are shown more dramatically in figure 4.6 where the contribution of O and N line emission to

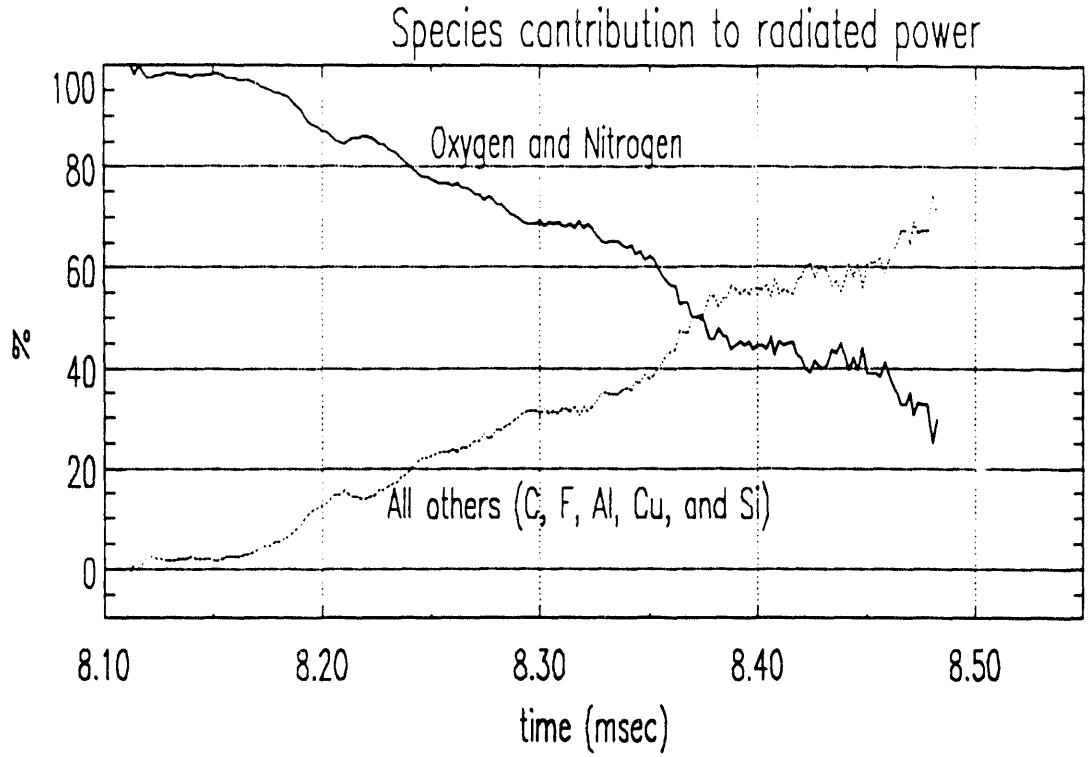

Figure 4.6: Time-resolved contribution to the midplane radiated power from the line emission of 2 groups of impurities.

the radiated power for chord 1 is compared to the contribution of all the other species. From less than 2% at 8.15 *m*sec, the contribution from C, F, Al, Cu and Si reaches 60% at 8.45 *m*sec. This result is also partly due to the large excitation rate coefficient of some of the lines from these elements at low T_e, in particular the C IV doublet at 1548.2/1550.77 Å, the Al III doublet at 1854.72/1862.79 Å and the Si IV doublet at 1393.75/1402.77 Å. A nearly identical graph was obtained for chord 8. Note that the traces in the figure were obtained directly from the calibrated VUV spectrometer data and do not depend on estimates of n_e or T_e.

The diverging concentration levels of the two groups of impurities are indicative of their different sources and production mechanisms. Adsorbed molecules containing oxygen or nitrogen are attached to the chamber internal surfaces by weak van der Waals forces and are easily set free by low energy processes [115]. The very high initial concentrations of O and N suggest that the reversal coils discharge, which is triggered 90 μsec before the main discharge, is probably responsible for the release of a large amount of oxygen and nitrogen (adsorbed on the Nichrome foil covering the coils) that gets ionized later by the I_z discharge. Induced currents near the surface of the coils can provide enough energy to desorb impurities (when shots are taken with no I_z discharge, the reversal discharge sometimes produces a visible gas breakdown). Molecules or atoms adsorbed on the I_z electrode tips would also get into the plasma quickly. When the discharge terminates, most of the O and N impurities are simply redeposited on the internal surfaces, only to be released again on the next shot. The irregular shape and the folds of the nichrome foil covering the reversal coils can explain the limited success achieved with titanium gettering.

Since most of the desorption processes occur early in time, oxygen and nitrogen ions leaving the plasma outnumber the incoming ions later in the discharge and the concentrations of these impurities go down. Similar behavior has been observed in tokamaks.

The fact that the O and N concentration stays high even after a large number of shots have been taken indicates that air is possibly leaking into the chamber at an excessive rate for the experiment. The high pumping speed provided by the vacuum pumps gives good base pressure but may mask inadequate sealing of the vacuum vessel, even if the measurements were always made in conditions where no leak could be found with a helium leak detector. Oxygen and nitrogen absorbed in components inside the chamber, like the teflon tape insulating the reversal coils, could be sources of virtual leaks. The base pressure was in general lower when the room temperature of the experimental area was lower,

indicating that outgassing from inside the vessel was not negligible. Note also that the vacuum vessel was flushed with nitrogen every time it was brought to atmospheric pressure. In the case of oxygen, an additional source is the ceramic (aluminum oxide) insulation of the electrodes. On each shot, some of the I_z current flows back along the insulation to the machine wall, eroding the ceramic and releasing oxygen and aluminum impurities; the oxygen forms molecules that are easily desorbed on subsequent shots. The ceramic pieces placed at the tips of the figure-8 coils (used to insulate closely spaced loop sections) are also a possible source of oxygen. Those various oxygen sources can explain why the oxygen concentration does not decrease as fast as the nitrogen concentration.

While oxygen and nitrogen line emission dominates the early part of the discharge, the other impurities come into play in a vigorous manner after the spheromak formation. The delayed release of silicon and copper is particularly evident in figures 4.3(g) and 4.3(h), where line radiation for different ionization stages of these impurities is shown. Substantial contribution from Si and Cu does not begin until 80 μsec after the triggering of I_z. The same is true for fluorine (not shown in figure 4.3). This can be contrasted to the case of nitrogen (figures 4.3(c) and 4.3(d)) for which lines of all the important ionization stages are strong very early. The presence of silicon is due to energetic processes occurring on the glass annuli surfaces during the formation phase while the magnetic field lines are still open and fast charged particles can reach and hit those glass barriers. When the field lines close, the release of silicon is much reduced and the absolute concentration of Si goes down, as can be seen from table 4.2.

Copper is released when plasma currents start interacting with the figure-8 coils, which are made of this metal. Patterns indicative of surface currents can be seen on these coils when the vessel is brought to air. The late release of Cu suggests that the main source of this impurity is probably not the Cu-W alloy used for the electrode tips. It should be pointed out however that the late appearance of Cu and Si in the midplane is partly due to the transit time from

the source of these impurities to the middle section of the machine. Off-midplane time-resolved spectroscopic measurements have unfortunately not been made.

The case of aluminum is interesting because the concentration of this element increases throughout the discharge (although the total number of aluminum ions in the plasma may not increase since the spheromak shrinks over time). The release of Al atoms into the plasma is associated with the aluminum oxide (ceramic) components used in the vessel. A fraction of the I_z current flows back along the electrode ceramic insulation between 8.14 and 8.21 $m$sec and energetic processes on the surface of the ceramic eject Al atoms or ions during that time. One would expect the Al concentration to start decreasing after that but the shrinking of the plasma and the central peaking of n_e during the spheromak decay phase bring more plasma in close proximity to the insulating ceramic pieces placed at the tips of the figure-8 coils and interaction between the plasma and those pieces bring more aluminum impurities into the plasma.

No general statement can be made for carbon because of the many possible sources (teflon tape, oil vapors, stainless steel wall and adsorbed molecules) for this impurity. The relatively low carbon concentration during the first 100 μsec is somewhat surprising in view of the large initial amount of oxygen and nitrogen.

The above discussions on impurity sources and release mechanisms was only qualitative and additional experimental work would be needed to verify some of the ideas presented and to evaluate quantities of interest such as diffusion coefficients, impurity confinement times, etc. The information gathered by the combined use of the pyroelectric detector and the VUV spectrometer provides a great first step in the understanding of impurity behavior in MS and indicates direction for further experimentation.

Among the most surprising results of this chapter are the very high initial concentration of oxygen and nitrogen, explaining the abnormally high electron density, the large contribution of the other impurities (Al, Si, C, Cu and F)

to the radiated power during the spheromak decay, and the fact that T_e peaks before the peak of I_z. Even if the amount of oxygen and nitrogen in the plasma was reduced to a negligible level and n_e lowered by a factor of 5, the combined concentrations of the other impurity elements would be high enough to keep MS in a radiation dominated regime.

Chapter 5

Power balance

Two aspects of the power balance of the MS discharge will be discussed. First, we will look at the entire discharge in the vacuum vessel. The energy input here is basically determined by the voltage at the I_z electrodes and the current running through them, and this energy is eventually dissipated in radiation (light) and acceleration of particles (electrons, ions and neutrals) that heat the electrodes and strike the internal surfaces of the vessel. Secondly, the power balance of the decaying spheromak is treated. Without auxiliary heating, the spheromak energy source is the ohmic heating associated with the decay of its magnetic fields. In the case of MS, considering the high concentration of impurities, the spheromak energy is expected to be lost mainly through radiation. In this chapter, use will be made of the data taken with the 2π pyroelectric detector. This detector is not collimated and is flush with the inside wall of the machine in the midplane; details of its setup were given at the end of chapter 3.

5.1 Power balance of the electrode discharge

The power going into the vacuum vessel from the main discharge can be obtained from the voltage at the base of the electrodes and the current flowing through the I_z circuit. These quantities are measured routinely and with good

accuracy. The power delivered by the main discharge, averaged over 5 shots, is shown in figure 5.1(a) where the product $\Delta V \times I_z$ is plotted against time. ΔV is the voltage difference between the positive (anode) and negative (cathode) electrodes. Integration of the signal gives a total input energy of 125 kJ.

Some of this energy is initially stored in the plasma inductance L_p and is liberated when dI_z/dt turns negative. It is possible to evaluate L_p from the power and current curves and extract the "resistive" power going into the vessel. In contrast to the apparent power given directly by $\Delta V \times I_z$, this resistive power is never negative and has a better time correlation with actual plasma heating and with the various energy dissipation mechanisms. Separating ΔV into its resistive and inductive components, the apparent main discharge power is:

$$P = \Delta V I_z = \left(R_p I_z + L_p \frac{dI_z}{dt} + \frac{dL_p}{dt} I_z \right) I_z$$

where R_p is the plasma resistance. Taking the time derivative of this expression and evaluating the resulting equation at the point where dI_z/dt is zero, we obtain:

$$\frac{dP}{dt} = \left(L_p \frac{d^2 I_z}{dt^2} + \frac{d^2 L_p}{dt^2} I_z \right) I_z \qquad (5.1)$$

where it was assumed that R_p is constant at the peak of the current pulse; this is a good assumption since at this point we are well into the discharge, the gas is fully ionized and the plasma resistance has only a weak time dependence. Now to evaluate the time dependence of L_p, use will be made of magnetic scan data giving the total toroidal magnetic energy W_B(tor) as a function of time for the so-called "scan 24" conditions [24]. These differ from the standard conditions used for this thesis mainly in the use of additional capacitors for the main discharge, which increase the I_z current and the peak spheromak fields. The curve for W_B(tor) can be found in figure 5.4(a). During the rise of I_z, $W_B(\text{tor}) \approx \frac{1}{2} L_p I_z^2$. From the measured W_B(tor) and I_z, it is determined that L_p is roughly constant between 8.10 and 8.18 $m$sec for scan 24. If L_p has any time dependence for the same time interval in the standard conditions, it is therefore weak and can be

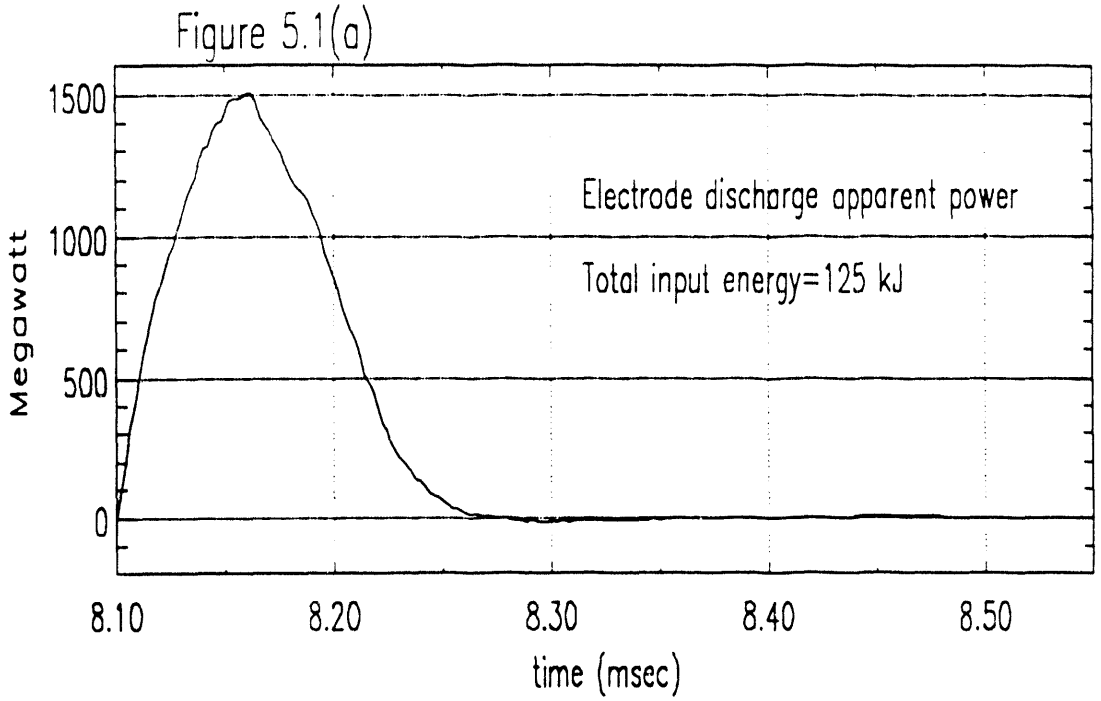

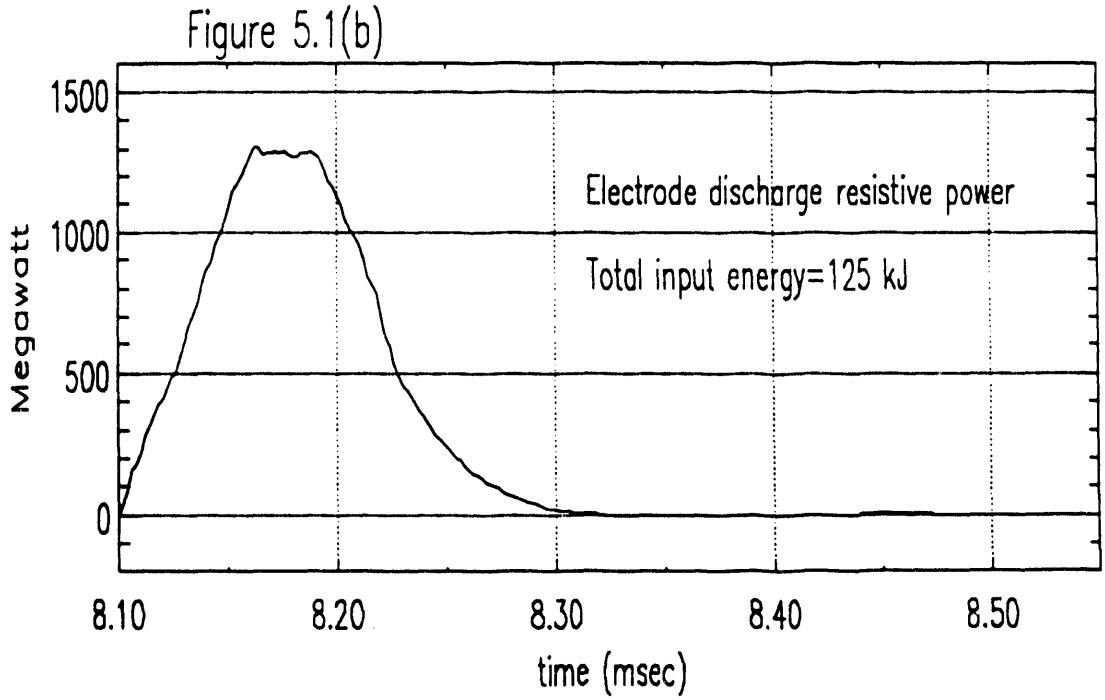

Figure 5.1: **(a)** Power delivered by the main I_z discharge as obtained from $\Delta V \times I_z$, where ΔV is the voltage drop in the plasma. **(b)** Resistive power calculated from equation (5.2).

neglected. Note that the relation $W_B(\text{tor}) \approx \frac{1}{2} L_p I_z^2$ does not hold during the I_z current decay because internal plasma currents are then induced that maintain the toroidal B fields.

Neglecting the d^2L_p/dt^2 in equation (5.1), solving for L_p, and using the experimental data for P and I_z, we get L_p=110 nH at t=8.176 $m$sec (time of I_z current peak). The resistive power is given by:

$$P_{res} = (I_z R_p) I_z = \left(\Delta V - L_p \frac{dI_z}{dt} \right) I_z \qquad (5.2)$$

where the term involving dL_p/dt has been dropped. The electrode discharge resistive power obtained from equation (5.2) with L_p=110 nH is shown in figure 5.1(b). Note that time integration of this signal gives the same total input energy (125 kJ) as before. The resistive power pulse is stretched out in time by the $L_p dI_z/dt$ term. At the peak of the P_{res} pulse, about 1.3 GW of power is liberated inside the vacuum vessel. Solving for R_p in equation (5.2), one gets $R_p \sim 3.4\ m\Omega$ at t=8.176 ms.

The electrode discharge input power signal has a flat-top portion between 8.16 and 8.19 $m$sec. It was determined in chapter 4 that the electron temperature reaches a maximum at ~8.16 $m$sec and decreases from that point on. The decrease of T_e during the flat-top portion of the input power pulse can be explained by the increase in total impurity concentration between 8.15 and 8.22 $m$sec which was given numerically in table 4.2. While still being radiated away at a high rate, more of the I_z discharge power goes into heating and ionizing the incoming particles while the newly created cold electrons bring T_e down.

As far as the 345 kJ of total I_z bank energy are concerned, it was determined (by the use of the high voltage probe at different locations) that besides the 36% (125 kJ/345 kJ) going into the electrode discharge, 28% is lost in the RG-8 cables connecting the I_z ignitrons to the electrodes, 11% is lost in the copper strips used to increase the I_z circuit inductance, 19% is lost in the I_z ignitrons and crowbar resistances (most of this in the ignitrons), and 6% goes into the

internal and external (25 $m\Omega$ for each capacitor) resistances of the capacitors and into the RG-8 cables connecting the capacitors to the I_z ignitrons. The largest fraction of wasted I_z bank energy goes into the RG-8 cables. There are 80 such cables going from the ignitrons to the positive electrodes in the standard conditions (and also 80 going to the negative electrodes), each about 11 m in length. The DC resistance of a RG-8 cable is 6.1 Ω/km for the center conductor and 4.0 Ω/km for the braid. A larger number of cables or cables with a lower resistance could be used to minimize the resistive losses between the I_z ignitrons and the electrodes.

Finally, it should be mentioned that the power input into the plasma due to the current pulse in the reversal coils is small compared to the main discharge power input. The much smaller net energy input of the reversal coils was established by looking at the stored poloidal magnetic energy at t=8.10 $m$sec, the time of peak reversal current. The curve for W_B(pol) in the scan 24 conditions can be seen in figure 5.4(a). The maximum poloidal energy, generated mostly by the current in the reversal coils with a small contribution from the bias field, is about 20 kJ in the standard conditions. As the reversal current decays, some of the poloidal field is trapped by the plasma created by the I_z discharge while the rest of the poloidal magnetic energy is dissipated in induced currents going through the reversal coils circuit. The input energy associated with the reversal coils then comes from the decay of the trapped poloidal field and is probably less than 10 kJ.

The principal mechanisms involved in the dissipation of all the electrode discharge energy are examined in the following subsections.

5.1.1 Radiation losses

As it was shown in the previous chapter, the radiation losses consist almost

exclusively of impurity line radiation due to the high electron density, low T_e and high concentration of impurities. Figure 5.2 shows the total power radiated by the plasma, P_{rad}, during the discharge as seen by the 2π pyrodetector. This curve was obtained by assuming isotropic emission of the plasma as a whole so that the power per steradian directly measured by the detector simply needs to be multiplied by 4π to get the total radiated power. This will be true for a plasma of any shape if the detector is placed at a large enough distance compared to the size of the plasma, and also true for a spherically symmetric plasma no matter how close the detector is. In the case of MS, the plasma is roughly spherical and small enough so that the raw pyrodetector data can be treated in the way described above with good confidence.

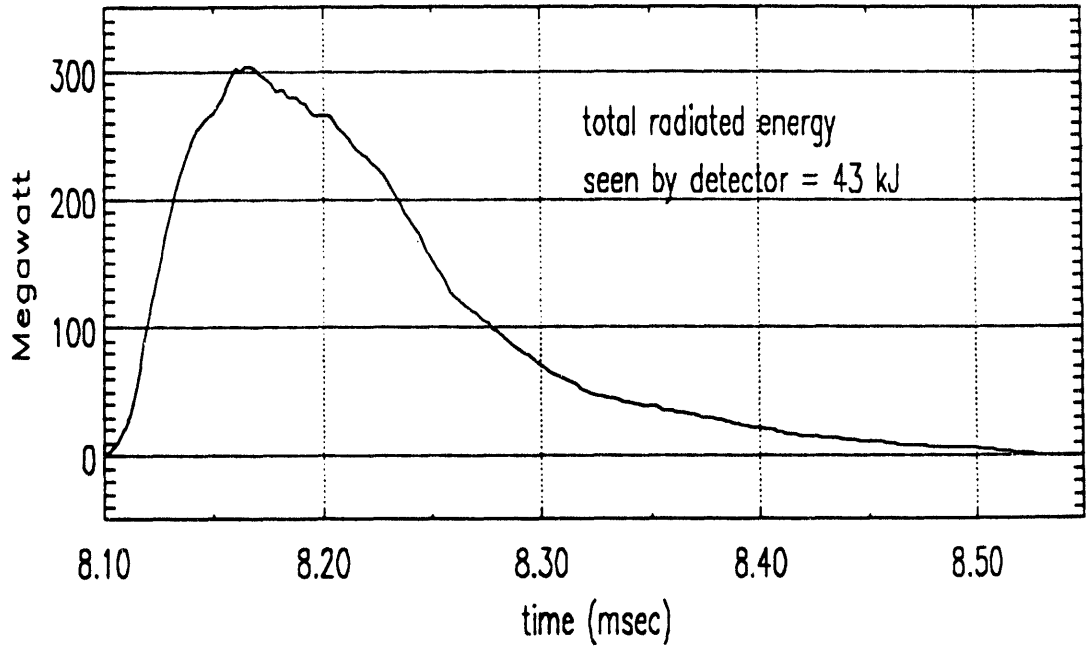

Figure 5.2: Total power radiated by the MS discharge as measured by the 2π pyrodetector. This is the average of 6 shots taken in the standard conditions.

Notice that the dip in the collimated pyrodetector signal around 8.175 $m$sec for chord 1 (see figure 4.1(a) or 4.4) is not present in the 2π detector signal. In fact, the chord 1 dip disappears if the midplane B probe is inserted far enough into the plasma. These facts suggest that the processes responsible for the dip are localized in the central (small r) portion of the midplane and that they do not involve a substantial amount of energy.

Integrating the signal of figure 5.2, the total radiated energy seen by the pyrodetector is found to be 43 kJ. This is in excellent agreement with extrapolations on total radiated energy based on two other sets of measurements. First, use can be made of the midplane emissivity data presented earlier: P_{rad} can be evaluated by selecting a toroidal shape of reasonable size (as indicated by the magnetic probes for example) for the plasma and assuming that the emissivity does not change greatly as a function of z. The second data set is a combination of the measurement made with a 2π pyrodetector covered with a quartz window (for which the floating setup was not necessary since no particle was hitting the detector) and the measurements giving the ratios of the midplane pyrodetector signal with and without the quartz window for different chords, from which the average quartz/no quartz ratio over the entire plasma volume in the midplane can be obtained. Assuming again moderate z dependence of the ratio data, P_{rad} can be evaluated from the 2π-with-quartz pyrodetector data. The fact that these evaluations of P_{rad} using midplane collimated measurements agree well with the 2π detector result shows that the region surrounding the electrode tips, which are seen by the 2π detector, do not contribute much to the total radiated power. Photographs of the discharge using films sensitive to visible light showed that the electrode tip region was brighter than the main plasma in that spectral range. This is viewed as an indication that since the plasma is colder near the electrodes, the radiation spectrum in that region is shifted toward longer wavelengths.

Further evidence of the small contribution to P_{rad} from the electrode tip region

was provided by collimated bolometric measurements with a direct view at an electrode. The vacuum vessel port used was off-midplane and the detector line of sight was through the region between one of the glass barriers and the back wall that holds the electrodes (the detector view is shown in figure 2.1). No significant difference in the pyrodetector signal was observed when the collimated setup was aimed directly at the electrode tip or at the ceramic insulation further down along the body of the electrode, and this signal was much smaller than the midplane pyrodetector signals. While this shows that the radiation from the electrode tip region is not especially high, it does indicate that some power is radiated "behind" the glass barriers (i.e., between each barrier and the adjacent back wall). Most of this region is not in the view of the 2π pyrodetector. The energy input in that region comes in part from the fraction (about 5%) of the I_z current that flows to the back wall along the ceramic insulation on each shot, as illustrated in figure 5.3(a). The difference between the solid and dotted curves gives the amount of current flowing back to the wall for that particular electrode. The back-current is present for about 80 μsec centered on the peak of I_z. This corresponds to the peak of the signal obtained with the collimated pyrodetector looking behind one of the glass barriers, as shown in figure 5.3(b). Note that a spectroscopic time-integrated survey of that region has demonstrated that the same impurity elements (with similar relative concentrations) as the ones found in the midplane plasma are present there. The main difference is a lower electron temperature as determined by the relative intensity of the different ionization stages.

Considering the amount of current flowing back to the wall and the magnitude of the power radiated behind the glass barriers, along with the fraction of the main plasma screened from the 2π pyrodetector by the figure-8 coils and the midplane magnetic probe, the total amount of energy radiated during a MS discharge is adjusted up to 50 kJ (from the 43 kJ of figure 5.2) with an accuracy of 20%. So about 40% (50 kJ/125 kJ) of the total electrode discharge input

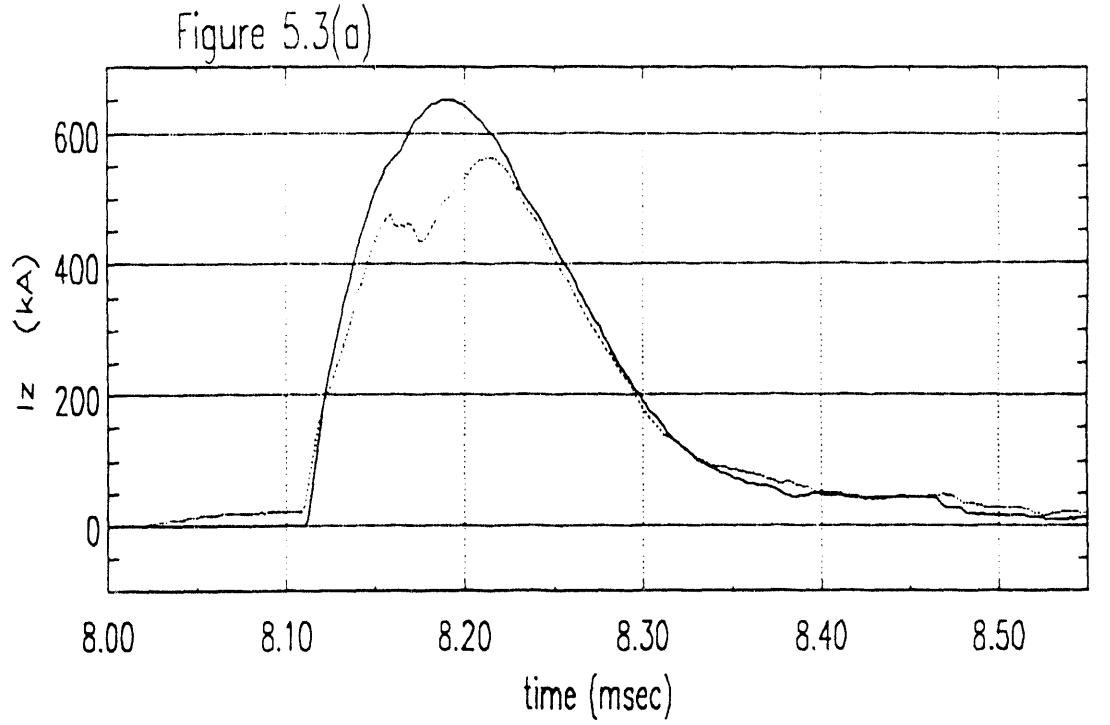

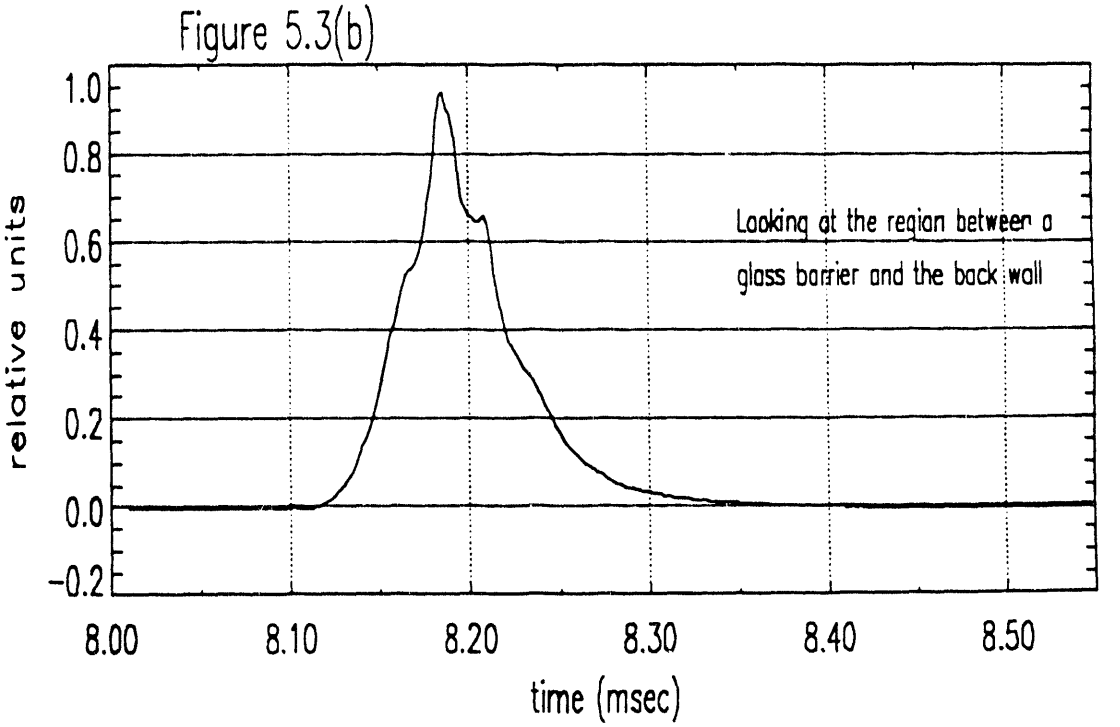

Figure 5.3: (a) I_z current measured by Rogowski loops outside (solid line) and inside (dotted line) the vacuum vessel; (b) signal from the pyrodetector looking "behind" a glass barrier.

energy is lost through radiation.

5.1.2 Electrode heating

The extremity of the electrodes, i.e., the surface of the rounded part of the tip, is bombarded during the discharge by charged particles (ions for the cathode and electrons for the anode) that have been accelerated in the potential drop of the electrode plasma sheath. The resultant rapid heating of a thin layer of the electrode tip is greater at the cathode because the voltage fall is larger for that electrode. The larger cathode fall voltage is needed for various processes that increase the emissivity of the initially cold cathode so that it can act as an electron source capable of supporting the discharge current [116] (the anode fall voltage can be high in cases where a strong magnetic field parallel to the surface of the anode makes it difficult for the electrons to reach that electrode). The fraction of the discharge energy that heats the electrodes varies greatly between the different types of discharge and it can be very high if the inter-electrode gap is small and the initial gas pressure is low.

Because of the wide spacing between the electrodes (41 cm) and the few mTorr of initial gas pressure in the case of MS, it is not expected that a very large fraction of the electrode discharge energy goes into heating of the electrode tips. Nevertheless, a series of shots with aluminum electrode tips resulted in severe erosion and damage of these tips, especially at the cathode. Even if this was after many shots, the high degree of deterioration of the Al electrodes suggests that electrode heating should be considered in the discharge power balance.

To estimate the energy going into the electrodes, we will use information obtained from shots made with stainless steel electrodes. Elkonite is not a true alloy and does not have well defined thermal properties (for example, the copper and tungsten forming this material will melt at their own characteristic melting

points upon heating of the sample) and this would be a problem in the following analysis.

The stainless steel electrodes showed evidence of surface melting of the rounded part of the cathode tip to a depth of several μm. To get an estimate of the energy going into the electrode tips, we will calculate the power density (W/cm^2) required to melt a layer of s.s. several μm deep. The temperature of a semi-infinite body can be calculated as [117]:

$$T(x,t) = T_0 + \left(\frac{\sqrt{\kappa}}{K\sqrt{\pi}}\right)\int_0^t \left[f(t-\tau) exp\left(\frac{-x^2}{4\kappa\tau}\right)\frac{1}{\sqrt{\tau}} \right] d\tau \qquad (5.3)$$

where T_0 is the initial temperature of the body, K is the thermal conductivity, κ is defined as $\kappa = K/(\rho c_s)$, ρ is the mass density, c_s is the specific heat, $f(t)$ is the time-dependent power flux (power density) at the surface, and x is the depth below the cathode surface. For the case of a constant power flux F_0 applied over the entire interval $[0, t]$, equation (5.3) can be rewritten as:

$$T(x,t) = T_0 + \left(\frac{2F_0}{K}\sqrt{\frac{\kappa t}{\pi}}\right) exp\left(\frac{-x^2}{4\kappa t}\right) - \left(\frac{F_0 x}{K}\right) erfc\left(\frac{x}{2\sqrt{\kappa t}}\right) \qquad (5.4)$$

where $\mathrm{erfc}(y) = 1 - \mathrm{erf}(y) = 1 - (2/\sqrt{\pi})\int_0^y exp(-\tau^2)\, d\tau$. The semi-infinite body approximation is valid in our case because the discharge is of very short duration and the bulk of the electrode tip remains at its initial temperature while the surface is being heated.

For type 304 stainless steel, K=0.18 W cm^{-1} °K^{-1}, ρ=8.02 g cm^{-3} and c_s=0.5 J g^{-1} °K^{-1}. The melting point for s.s. is approximately 1700 °K. Using equation (5.4), it is found that for a heating interval of 100 μsec a power flux F_0 of 0.2 MW/cm^2 is needed to melt an electrode tip layer a few μm (13.8 μm to be exact) deep. The surface temperature reaches 2956 °K while 100 μm deep into the stainless steel, the temperature has increased by only 0.75 °K at the end of the 100 μsec heating interval. The magnitude of F_0 implies a voltage drop greater than 100 V in the cathode fall. This value was obtained by comparing $F_0 \times$(tip area of one electrode) to $\frac{I_s}{16} \times V_{drop}$, with the knowledge that the ions

accelerated toward and heating the cathodes carry only part of the discharge current. Assuming that the cathode sheath thickness is a few Debye lengths, this voltage drop implies a very large electric field at the cathode surface since the low T_e and high n_e of the MS discharge plasma combine to produce a very small value for the Debye length ($\lambda_D \propto (T_e/n_e)^{1/2}$). This large E field can greatly increase the emission of electrons at the cathode through field-enhanced thermionic emission[116,117].

Based on a value of 9 cm^2 for the area of an electrode tip and counting the 16 electrodes on the cathode side, the 100 μsec power flux pulse to the electrodes is seen to be responsible for 2.9 kJ of the main discharge energy going into cathode heating. The melted section of the electrodes on the anode side is smaller and a maximum value of 1 kJ is estimated for the energy going into the anodes. So a total of about 4 kJ is used for heating the electrode tips. A similar result would have been obtained if a sinusoidal pulse shape had been used for F_0 instead of a square pulse. Note that the entire area of the tip end is probably not melted on each shot and the above value for the heating energy could be overestimated. Furthermore, if the electrodes receive a higher power flux F_0, the tips will start to vaporize (at around 3300 °K for stainless steel) and the heat conduction into the electrodes will be greatly diminished, putting an upper limit of a few kJ on the amount of energy going into the electrode tips.

Elkonite electrodes do not show as much evidence of surface melting in good part because of their higher thermal conductivity (the thermal conductivities of copper and tungsten are 22 and 10 times greater than the conductivity of stainless steel, respectively). In fact, a small section of each Elkonite tip is eroded in a way indicative of the formation of cathode spots. This mechanism of electron generation that helps provide the large discharge current may be necessary for a longer period of time in the case of the Elkonite electrodes since the efficiency of thermionic emission [116] will be reduced on the cooler Elkonite tip compared to the melted s.s. electrode tip. In any case, there is no reason

to believe that the energy going into the Elkonite tips is substantially different than the energy going into the s.s. tips. And again, a much larger amount of electrode heating for the Elkonite tips would imply vaporization of the electrode material (for which there is no evidence) and this would reduce heat conduction, limiting the total energy going into the tips to a few kJ.

Finally, the resistive energy dissipated in the body of the electrodes (as opposed to the impact heating of the tips) needs to be considered since the electrode voltage is measured at the base of the electrode assembly and includes the potential drop in the stainless steel electrode body. The solid s.s. body is 32 cm long with a diameter of 3.1 cm. Its DC resistance was measured at 0.34 $m\Omega$, in agreement with calculations based on the resistivity of type 304 s.s. (72 $\mu\Omega$-cm). This value will increase if a high frequency current pulse is sent into the electrode because the current will only travel through a surface layer of the electrode body. For the typical 3×10^3 Hz I_z current pulse in MS, the skin depth of s.s. is 0.78 cm which is half of the electrode body radius. For this ratio of skin depth to cylindrical conductor radius, the effective resistance is 25% higher than the DC resistance [118], or 0.43 $m\Omega$ in our case. From the measured I_z current (assumed to be distributed evenly among the electrodes), it is then found that a total of 2.1 kJ is dissipated in the body of the 32 electrodes.

So, of the 125 kJ delivered by the electrode discharge, about 50 kJ goes into impurity line radiation, 6 kJ into heating of the electrodes (~4 kJ for the tips and 2.1 kJ for the body), and 69 kJ remains to be accounted for. The net contribution to the total input power from the reversal coils, although small, will increase this last value even more.

5.1.3 Particle losses

During the spheromak formation phase, many processes are involved in the

joule heating (i.e., the conversion of the energy of directed drift motion in the electric field into random motion) of the plasma, not to mention compressional heating, anomalous ion heating, etc. The details of the various energy transfer mechanisms during that phase are out of the scope of the present work but it is clear that the part of the total plasma energy that is not radiated away eventually takes the form of particles hitting and giving their energy to the machine walls and other internal structures of the vessel. The particle losses are much larger during the formation phase due to the presence of open magnetic field lines that intersect solid surfaces. Electrons, ions and neutrals all contribute to the particle flux to the walls but considering the huge total energy involved in this process (more than 69 kJ as deduced in the previous section) it turns out that only electrons can provide a large enough outward flux to balance the electrode discharge input power still unaccounted for.

To obtain an upper bound on the energy going to the ions and neutrals, oxygen ions will be considered. Oxygen is the most abundant impurity species and its ions have more energy than deuterium ions during the formation phase (as determined from Doppler broadening) while having a similar concentration. We will look at the 150 μsec time interval between 8.12 and 8.27 $m$sec where most of the electrode discharge energy is deposited into the plasma and dissipated away. The most energetic oxygen ions with substantial abundance (O IV and O V) have a maximum temperature of ~400 eV early in the 150 μsec interval. The ions quickly cool off and have less than 20 eV at 8.27 $m$sec. We will then assume a maximum average temperature T_i of 200 eV for the oxygen ions during the formation phase. Based on that temperature, an upper limit energy of 600 ev will be attributed to each lost ion (this includes $\frac{3}{2}T_i$ of internal kinetic energy, an amount T_i of work done by the plasma pressure pushing the ion out of the plasma [119], and 100 ev of ionization energy). The highest oxygen concentration observed is 2.4×10^{14} cm^{-3} at a radial position r=12 cm at t=8.22 $m$sec. In the spirit of our upper bound calculation, that maximum value of oxygen density

will be used for the entire plasma volume and 150 μsec time interval. Neutral atoms are neglected because of their low energy and concentration.

Assuming now a maximum plasma volume of 40 cm (the axial distance between the electrodes) $\times \pi(25\text{ cm})^2 \approx 7.8\times10^4$ cm^3 during the formation phase, the maximum energy dissipated if all the ions escape is estimated at 1.8 kJ. Because of the open field lines early in the discharge, the ions may recycle a number of times during the formation phase. However, the recycling rate is limited by the low speed of the oxygen ions. A 200 eV oxygen ion has a thermal velocity of 3.46 cm/μsec. Using this as the maximum possible average ion velocity and considering the distance the ions have to travel to escape the plasma, hit the walls and be replaced by incoming atoms or ions, it is estimated that the entire inventory of oxygen ions cannot be recycled more than 5 times during the 150 μsec time interval. The upper limit on the energy going into oxygen ions that can eventually take the form of ion or neutral flux to the walls is then $\sim$9 kJ. In regard of the approximations we have made, the real amount of energy associated with ion and neutral fluxes to the walls is probably much lower. A similar result is obtained if the working gas, deuterium, is considered. Deuterium ions could recycle faster but they are less energetic during the formation phase where most of the energy is dissipated.

So almost all of the $\sim$69 kJ of electrode discharge energy (plus the net input energy of the reversal coils) that is not dissipated in radiation or electrode heating eventually goes into electron fluxes reaching the walls and other internal surfaces through convection along open field lines (or along the closed field lines intercepting the glass barriers during the formation phase). The bulk of the power flux is through the ends of the machine in proximity of the electrodes and is associated with the most energetic electrons of the Maxwellian distribution since fast electrons suffer fewer collisions and carry more energy at a greater rate. The magnetic field lines close to the electrodes during the formation phase guide those electrons toward the base of the electrodes, the back walls and the

glass barriers. All these surfaces show evidence of particle impact. The electron flux could be higher on the anode side if a good fraction of the electrons accelerated toward these electrodes are deflected toward the back end by the magnetic fields near the tips (the pulsed magnetic field of the reversal coils does not penetrate the electrodes much and this could results in the existence of magnetic field components parallel to the electrode tip surface).

Such free-streaming of electrons requires that their mean free path be longer than the typical distance between the edges of the central plasma and the walls or structures that they hit in following the magnetic field lines. For electron-electron collisions along the B field lines, the mean free path is [120]:

$$\lambda_{ee} \simeq 3.4 \times 10^{13} \frac{\left[T_{e(eV)}\right]^2}{n_{e(cm^{-3})} ln\,\Lambda} \quad cm$$

where $ln\,\Lambda$ is the Coulomb logarithm. Note that this is comparable to the mean free path for electron-ion collisions. During most of the formation phase, the peak electron density is in the range 4–8 $\times 10^{14}$ cm^{-3}. The density at the edges of the central plasma will be lower, on the order of 10^{14} cm^{-3}. Now the plasma pressure along the magnetic field lines between the central plasma edges and the walls is roughly maintained considering that the ion sound velocity in our conditions is 1–2 cm/μsec and that the typical edge-wall distance is 30 cm. So the density of most of the plasma that an electron has to travel through to reach a wall is about 10^{14} cm^{-3}, assuming that temperature variations are small except at the walls. Using this value of n_e, we get $\lambda_{ee} \approx 71$ cm for 50 eV electrons (a value of 12 was taken for $ln\,\Lambda$). This is long enough for most of the energetic electrons responsible for the particle losses to stream freely to the walls without collision. The density can be higher on a thin layer near a wall because of the sudden decrease in temperature at that location; this may reduce λ_{ee} very close to the wall but it should still be greater than the layer thickness. The large value of the collision mean free path along the B field lines for electrons also means that a fluid treatment of particle loss via thermal conduction is not appropriate

since a large number of collisions is implied in such a treatment. Note that a density in the low 10^{13} cm^{-3} for the flux of energetic electrons (50–100 eV) is sufficient to account for the 60 kJ or so of particle losses, assuming an outgoing flux area of 2×1500 cm^2.

Naturally, in the presence of open field lines and with similar electron and ion temperatures, the electrons will remove energy from the plasma by escaping along these field lines at a much higher rate than the ions because of their greater velocity. This has been observed, for example, in some single-cell magnetic mirror devices [121]. In most magnetic mirrors however, the electron losses are limited, after an initial transient phase, by the requirement of plasma quasineutrality. The first electrons escaping the plasma leave behind a positive space charge and an electrostatic field is set up which retards the electrons and accelerates the ions. Eventually, both species diffuse at the same rate, leading to what is called ambipolar diffusion. The ambipolar diffusion rate is about twice the ion diffusion rate when electron and ion temperatures are equal [122].

Returning to the case of particle losses in MS, it is clear from our calculations on ion losses that ambipolar diffusion is not a vigorous enough mechanism to account for the energy losses during the formation phase. The only way to sustain a high electron flux carrying energy away from the plasma without going into an ambipolar regime is to have a flux of lower energy electrons entering the plasma at such rate as to keep it quasineutral. In mirror devices where high electron end losses have been observed, the source of the incoming electrons was a cold plasma located just outside the mirror traps. In MS, there exists a cold plasma in the end regions near the back walls during the formation phase as shown by measurements with the pyroelectric detector and the VUV spectrometer looking behind one of the glass barriers. A high n_e in the end regions along the B field lines was also assumed (from pressure balance considerations) in the calculation of λ_{ee}. Note that another source of slow incoming electrons is the secondary electrons emitted when the fast outgoing electrons strike the walls and

other internal structures. The secondary emission yield is of order 1 for normal incidence on clean metal surfaces of electrons with energies $\geq$50 eV [122,123]. Metals which have a layer of gas on the surface and dielectrics give higher yields. Furthermore, yields are greatly increased when the primary electrons fall at an angle to the surface. Most of the secondary electrons have energies between 2 and 5 eV and come out normally to the surface. Considering these facts, the secondaries resulting from the high energy electron flux to the walls can constitute a good part of the electrons refueling the cold outside plasma during the formation phase.

In concluding this section, we may note that the high electron flux to the walls during the formation phase, carrying more than half of the electrode discharge energy, is clearly detrimental to the quality of the spheromak plasma, as the high power flux to the walls and other internal surfaces liberates a large amount of impurities. The higher electron density observed when the electrode discharge input power is increased (in the hope of raising the spheromak electron temperature) is probably due to the resulting larger electron end losses which cause the release of more impurities that fuel the plasma density.

5.2 Power balance of the decaying spheromak

After 8.30 $m$sec, the power input from the I_z discharge is negligible and the fully formed spheromak gets its energy from the decay of its magnetic fields. Under the conditions of low T_e, high n_e and high impurity content described in the previous chapter, it is known both computationally [124] and experimentally [125] that the spheromak dissipates most of its energy through impurity line radiation. The confinement time of radiation dominated spheromaks have been shown to be rather insensitive to many plasma characteristics (n_e, stored

magnetic energy, etc.) [126], as it is observed in MS.

5.2.1 Measurements

The magnetic energy content of MS has been measured for the scan 24 conditions and is shown in figure 5.4(a). At t=8.30 $m$sec, the stored magnetic energy for the scan 24 shots was found to be 10.2 kJ while the power input associated with the decay of the magnetic fields was 146 MW [24]. In order to compare these values with the radiated power (P_{rad}) and energy, a few shots were taken under the scan 24 conditions with the 2π pyrodetector in the vessel. Note that this was done more than a year after the magnetic measurements were made and caution must be exercised in comparing the 2 data sets (for example, the L-probe used for the magnetic scan was not in the vacuum vessel for the 2π pyrodetector measurements). The power radiated at 8.30 $m$sec was measured at 115 MW and the total energy radiated from 8.30 $m$sec to the end of the spheromak decay was 8.1 kJ. The midplane B probe indicated that the magnetic fields had roughly the same amplitude for the shots with the 2π detector as for the earlier shots used in the complete magnetic scan. Considering then the magnetic energy and input power measurements of reference 24 to be still valid for our more recent shots, we find that the radiation losses in MS represent ~80% of the input power at 8.30 $m$sec, confirming the dominance of this loss mechanism. The radiated power is compared with the input power (the time derivative of the stored magnetic energy) during the entire decay phase in figure 5.4(b). It can be seen that impurity line emission accounts for 80 to 100% of the power losses during the spheromak lifetime. The error bars on the pyrodetector signal represent the $\pm$ 15% uncertainty in the evaluation of the total radiated power; the uncertainty in the input power is about $\pm$ 10% .

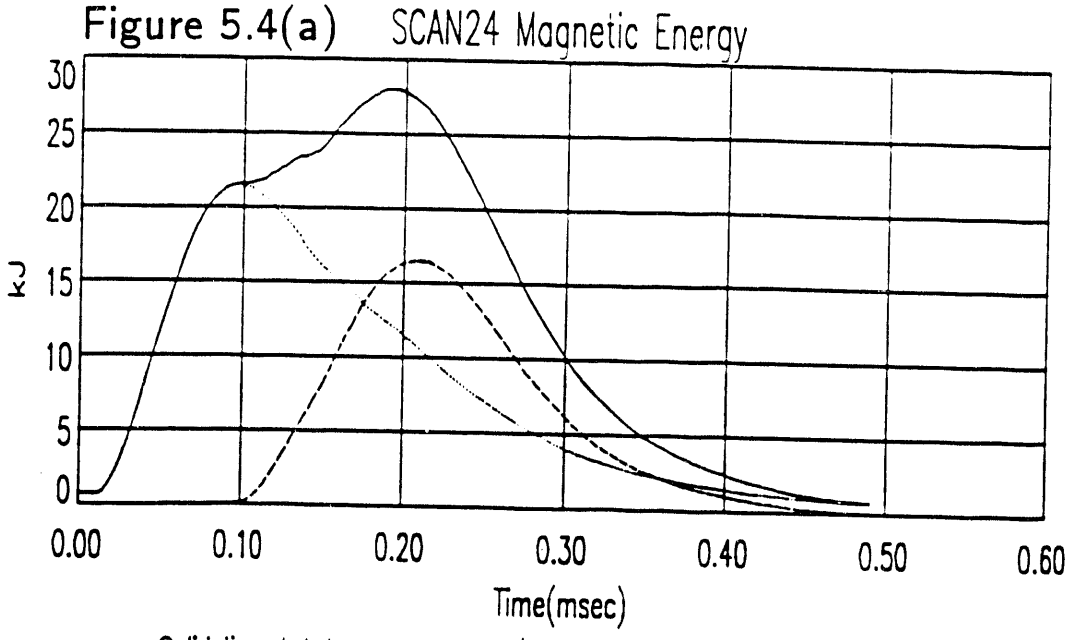

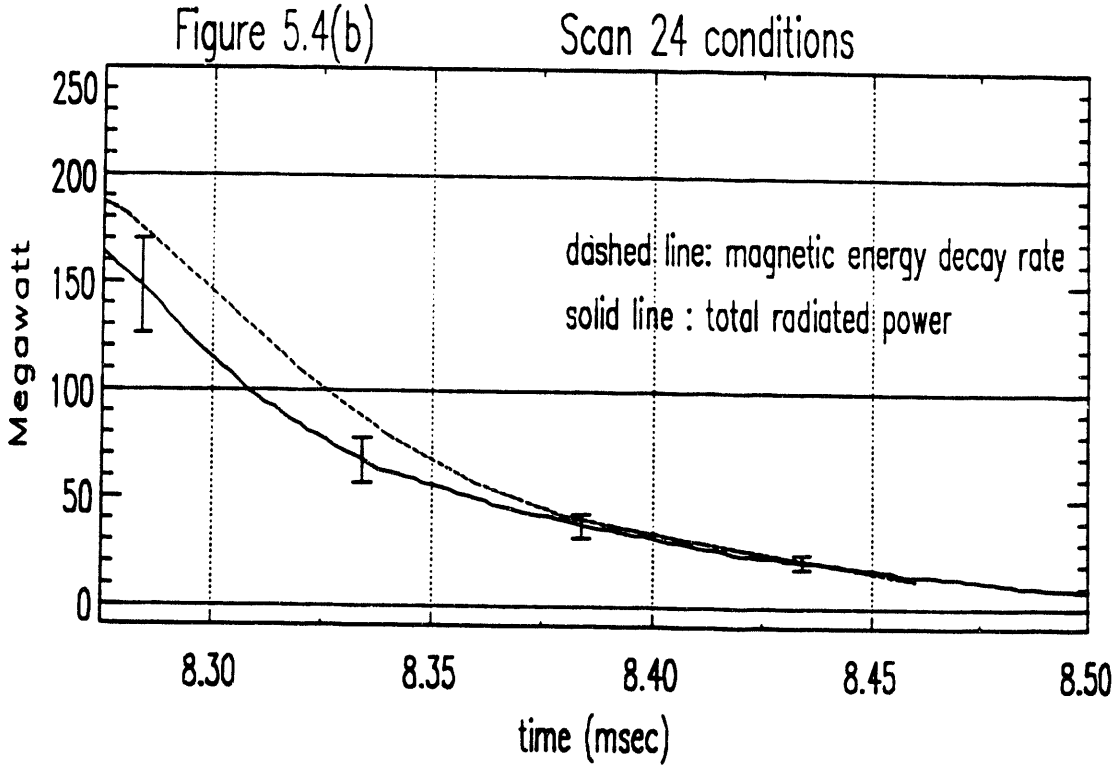

Figure 5.4: **(a)** Time evolution of the stored magnetic energy in scan 24 conditions; **(b)** comparison between the input power and the total radiated power during the spheromak decay phase.

Without using magnetic scan data or knowing the impurity concentration, evidence that MS is radiation dominated can be obtained by the 2π pyrodetector used under various conditions. For the large density and very dirty discharges typical of cleanup shots , the spheromak radiated power (assumed to dominate the power balance in this situation) is the same as for standard shots. So whatever the exact impurity content in the standard conditions, it is high enough for radiation to remain the dominant energy loss mechanism in MS.

In the analytical model of Auerbach for a radiation dominated compact toroid [126], the plasma lifetime was found to scale roughly as the square root of the stored magnetic energy. Such a scaling cannot be observed in MS because of the higher density and greater impurity content resulting from the larger I_z current needed to increase the spheromak magnetic energy. This larger stored energy simply gets dissipated at a higher rate through increased impurity line radiation as can be seen by comparing the 2π pyrodetector signals from the standard and scan 24 conditions (see figure 5.2 after t=8.275 $m$sec and figure 5.4(b)). Note also that in the analytical model the separatrix radius R_s was assumed constant. In MS, the plasma lifetime is also influenced by the magnetic pressure balance between the spheromak fields and the external bias field and R_s decreases during the decay phase.

The spheromak energy that is not radiated away is dissipated mostly through particle loss mechanisms. A 0-D computer simulation of the power and particle balance in MS has shown that thermal conduction is not an important process in the MS power balance [95]. Additionally in MS, there is no anomalous ion heating at the spheromak edges like that seen in CTX [49]. This anomalous heating at the edges is believed to be associated with high helicity dissipation resulting from magnetic field errors at the boundary between the spheromak and the flux conserver. Note also that charge-exchange losses are very small compared to the radiation losses in MS, as determined by the pyroelectric detector (see chapter 4). There is little doubt that the neutral density at the spheromak edges

close to the separatrix is large but the high electron density inside the separatrix, resulting in a short mean free path for neutrals, prevents these neutrals from penetrating far into the plasma. The neutrals then interact mainly with the ions at the edges which are in low ionization stages and for which the charge-exchange cross sections are small.

5.2.2 Discussion

The 0-D code simulating the time evolution of the particle and power balance in MS [95] contains the details of the balance equations and also the analytical form of the various processes involved. According to the code, the best way to increase T_e in MS was to simultaneously work on lowering n_e, reducing the impurity concentration and raising the stored magnetic energy. Impurity fractions of a few percent (of n_e) were assumed for the code runs. Experimentally though, a value of about 20% was found for the impurity fraction of the fully formed spheromak (combining all the species of table 4.2 at t=8.30 $m$sec). In view of this high concentration of impurities and of the fact that the ionization of impurities is directly responsible for the high electron density, and considering the increase in the absolute impurity content when an attempt is made to raise the stored magnetic energy, it is obvious that the emphasis in the effort to improve the spheromak characteristics should be put squarely on the control of impurities.

The limited success of the vacuum vessel cleaning and wall conditioning methods used in MS (heating of the chamber, discharge cleaning, Ti gettering) was due to the number and complex shape of the vessel internal structures, meaning that large fractions of the internal surfaces were left untreated, together with the huge amount of I_z discharge energy diverted toward processes responsible for the release of impurities (I_z current running along the electrode ceramic insulation,

electron fluxes to the walls, etc.). Note that a tenfold reduction in the plasma impurity content at t=8.30 $m$sec, resulting in a $\sim$2% concentration of oxygen say, would still have left the spheromak in a radiation dominated regime according to the power balance 0-D code. The exact percentage of impurities that would allow the plasma to get out of the radiation dominated regime depends on the recycling rates.

A comparison can be made between MS and spheromaks that have reached an electron temperature of $\sim$100 eV with a low plasma impurity content. In S-1 [14], the (electrodeless) inductive flux core formation scheme limits the amount of energy going into impurity release processes during the formation phase. The total energy used to form the plasma is smaller than in MS and the formation phase plasma is better isolated from the walls by closed magnetic flux lines. This results in a lower impurity concentration and lower n_e when the spheromak formation is completed. After taking a very large number of cleanup shots, the impurity fraction of the S-1 plasma becomes small (there is not a substantial amount of new impurities created on each shot like in MS) and the oxygen radiation barrier can be passed.

In contrast to S-1, a large amount of impurities is released during the formation phase of the CTX spheromak [15], another experiment where a T_e of 100 eV was achieved with ohmic heating only. The plasma in this device is generated by a magnetized plasma gun source with flux conserver and, as in MS, the large currents and energy of the electrode discharge in addition to the open field lines favor the release of impurities from the vacuum chamber internal surfaces early in the discharge. A high T_e could still be reached in CTX for two main reasons. First, a number of impurities associated with the coaxial electrode discharge are left behind in the translation of the plasma from the gun source to the flux conserver region because of their large mass. Heavy impurities are effectively removed from the plasma in this way. Secondly, the spheromak in the flux conserver is sustained for a long enough time (half a $m$sec or so) through

helicity injection that the remaining impurities are "pumped out" (meaning that some of the particles lost from the system are not replaced), eventually leading to a small impurity fraction and electron density, and allowing CTX to get out of the radiation dominated regime. This pump-out effect, accelerated by an anomalously short particle confinement time in the case of CTX, was seen in reversed-field pinches [127] and is in fact also observed in MS for O and N impurities during the spheromak decay (see table 4.2). During the first 500–600 μsec of sustainment, the CTX spheromak is totally radiation dominated, like MS in its decay phase. Note that CTX has to be refueled during helicity injection because the working gas is also effectively pumped out.

In MS, even if a method was found to sustain or "stretch" the spheromak for some time to let the O and N impurities pump out, it is not clear that a low enough impurity concentration would be achieved because of the high impurity content of the plasma and gas just outside the separatrix. Furthermore, some impurity species did not pump out during the decay phase in MS (see table 4.2) and there is no guarantee that they will during a sustainment phase. Ideally of course the initial release of impurities into the plasma should be sharply reduced. Within the constraint of keeping the Maryland Spheromak a boundary free system, it is very unlikely that this could be done without major modifications to the experiment.

Finally, it should be pointed out that a negligible impurity content in the MS plasma would not necessarily lead to a large increase in the spheromak decay time since new power dissipation mechanisms (magnetic fluctuations, instabilities, edge effects, etc.) will come into play. But these would in some sense be welcome since they represent some of the plasma physics that MS was designed to study.

Chapter 6

Conclusions

The combination of measurements made with a pyroelectric detector and a VUV spectrometer has provided a wealth of information about the power balance and the role of impurities in the Maryland Spheromak. For most plasma fusion experiments, these types of measurements, usually made under a variety of operating conditions, are very useful in isolating the principal mechanisms responsible for the deterioration of the major plasma characteristics. A number of important results have been obtained in MS, perhaps the dominant one being the existence of very large amounts of impurities throughout the discharge. Because of the diverse impurity sources and species involved, and based on the fact that many impurities are detached from the walls during the early part of the discharge by intense fluxes of energetic electrons that reach the internal surfaces of the vessel in their travel along open magnetic field lines, it is very unlikely that any wall conditioning program would substantially reduce the amount of impurities in MS.

As a consequence of this high impurity fraction, the electron density is increased dramatically and almost all of the input power during the spheromak decay phase is dissipated through impurity line radiation. The plasma never goes over the oxygen (the most abundant impurity) radiation barrier and the low electron temperature results in a highly resistive plasma with a short confinement time.

Improvements in plasma characteristics have been achieved in some devices by taking advantage of a short particle confinement time: the magnetic field configuration is maintained for a long enough time after the initial gas breakdown to allow the impurities to "pump out", leading to a cleaner, hotter plasma. Even is such a sustainment phase could be achieved in MS through helicity injection or field programming, there is no guarantee that the impurity concentration would reach a low enough level for the plasma to get out of the radiation dominated regime.

Appendix

Microwave pre-ionizer setup

A schematic of the entire experimental setup is shown in figure A.1. The magnetron is tunable from 8.5 to 9.6 GHz and can deliver 250 kW of microwave power for short pulses ($\leq$ 2 μsec) and somewhat less (150-200 kW) for longer pulses. For the pre-ionization experiment, the microwave pulse length was varied from 10 to 90 μsec, and the frequency was set at 8.56 GHz. This frequency will match the electron gyrofrequency for a magnetic field of 3 kGauss.

The magnetron, dating from the 1960's, was originally designed to produce short pulses ($\leq$ 1 μsec) at a high repetition rate for radar applications. In order to achieve pulse lengths of up to 100 μsec, a period of conditioning is necessary. Basically the duration of the high voltage pulse from the modulator is increased slowly until the magnetron starts arcing occasionally. The system is left pulsing in this way (at a few hertz) for some time. When the arcing stops, the process is repeated. The voltage is adjusted slightly up or down depending on the magnetron behavior. It is believed that the arcs ionize residual gas emanating from the various metallic surfaces inside the magnetron, and that the resulting charged particles are driven back into the metallic surfaces where they combine with getter material emitted by the magnetron filament. The length of the pulse is ultimately limited by the temperature rise of the cathode due to return electrons.

Immediately following the magnetron in the transmission line is a four-port

circulator that isolates the magnetron from reflections. Those reflections are redirected in the high power dummy load, which is a big aluminum cavity of pyramidal shape whose inside surfaces are covered with a microwave absorbing material.

The waveguide section that enters the MS chamber has to be isolated from the (grounded) transmission line leading to the magnetron. This is because this section jumps to some potential when it is in contact with the plasma created by the I_z discharge or when it is actually connected to the vessel wall. As shown in the schematic, the electrical insulation is provided by two horn antennas facing each other and separated on their edges by a layer of mylar. The large opening provided by the horns was necessary to prevent arcing inside the waveguide when mylar is introduced.

The microwave vacuum window is a slab of MACOR half a (microwave) wavelength thick. It covers the opening of the horn antenna inside the chamber. MACOR was chosen because of its good transmission properties (loss tangent=0.007 and dielectric constant=5.68 at 25 °C and 8.6 GHz), because it is machinable (thickness may be machined down if we want to increase the frequency), and because it does not introduce too many impurities in the plasma. It would have been preferable to locate the vacuum window elsewhere in the transmission line to prevent interaction with the plasma but unfortunately it turned out to be impossible to avoid arcing in the evacuated waveguide section leading to the antenna when this was tried (using different techniques and materials). The arcs were presumably due to a combination of factors: some of the fill gas was entering the evacuated section before the microwaves were launched; the bias magnetic field was affecting the wave propagation; the window materials caused electrical disturbances; and the inside surface of the evacuated section may have been outgassing.

Finally, a E-H tuner is used to minimize transmission line mismatch and control reflections. In fact, when the microwaves were launched in the "magnetized"

vacuum of the machine (no fill gas but with the bias and reversal magnetic fields on), the reflected power was negligible.

For completeness, more details on the modulator part of the setup are shown in figures A.2 and A.3. The negative high voltage pulse fed to the magnetron is created (figure A.2) by first charging a capacitor that has its negative side initially grounded through a diode. The switch that connects the positive side of the capacitor to the (grounded) magnetron anode is then closed and this pulls the other side of the capacitor to high negative voltage. The magnetron cathode, which is connected to the capacitor negative side, jumps to high voltage and the magnetron starts emitting until the switch is opened again. Note that this arrangement does not require the capacitor to be recharged completely after each pulse. Figure A.3 is a schematic of the all important "switch" which is really 2 tetrode switch tubes in parallel. Two were needed to handle the 23 amperes or so of current going through the circuit. Note that the grid supply and the high voltage pulser have to be isolated from each other; this is accomplished by the 2.5 H inductance on the grid supply side and the 10 μF capacitance on the pulser side.

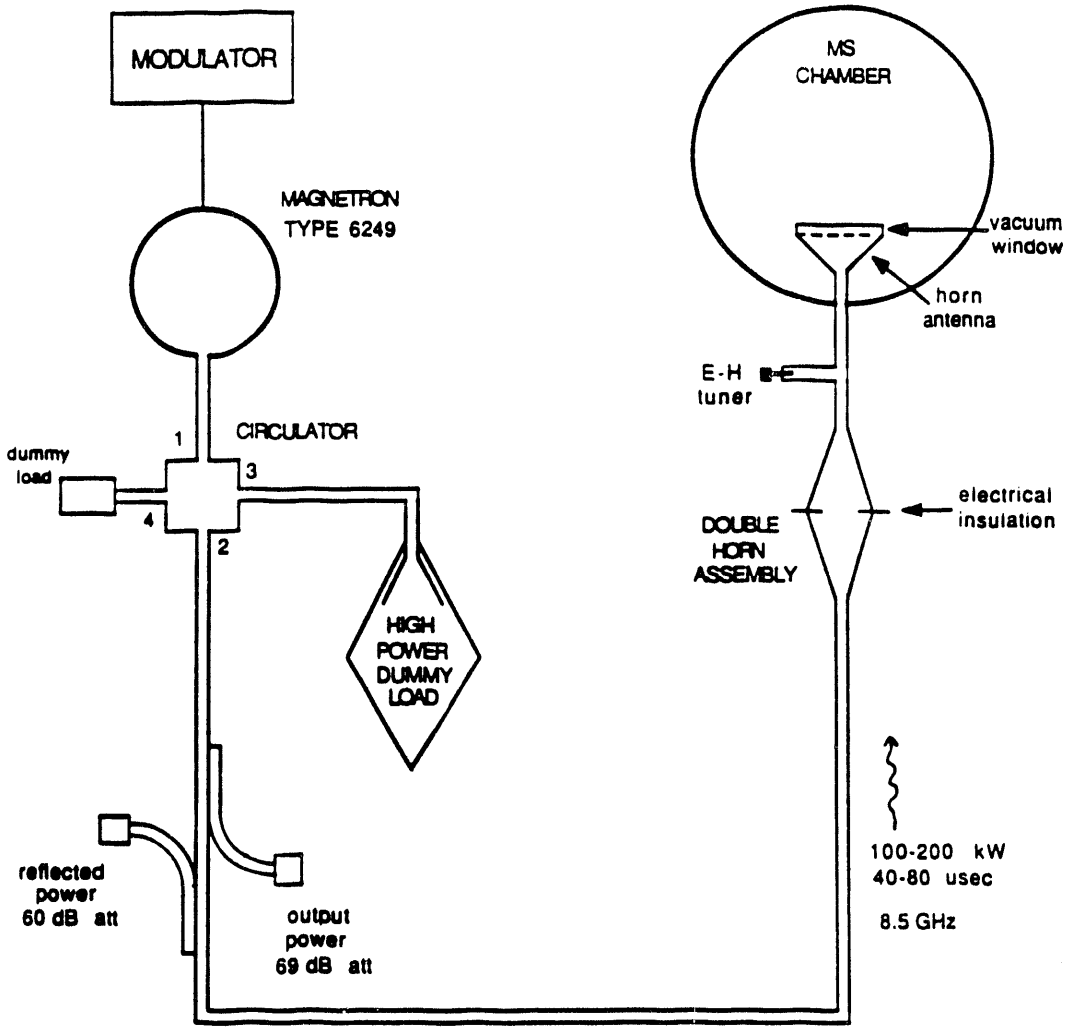

Figure A.1: Schematic of the microwave pre-ionizer setup.

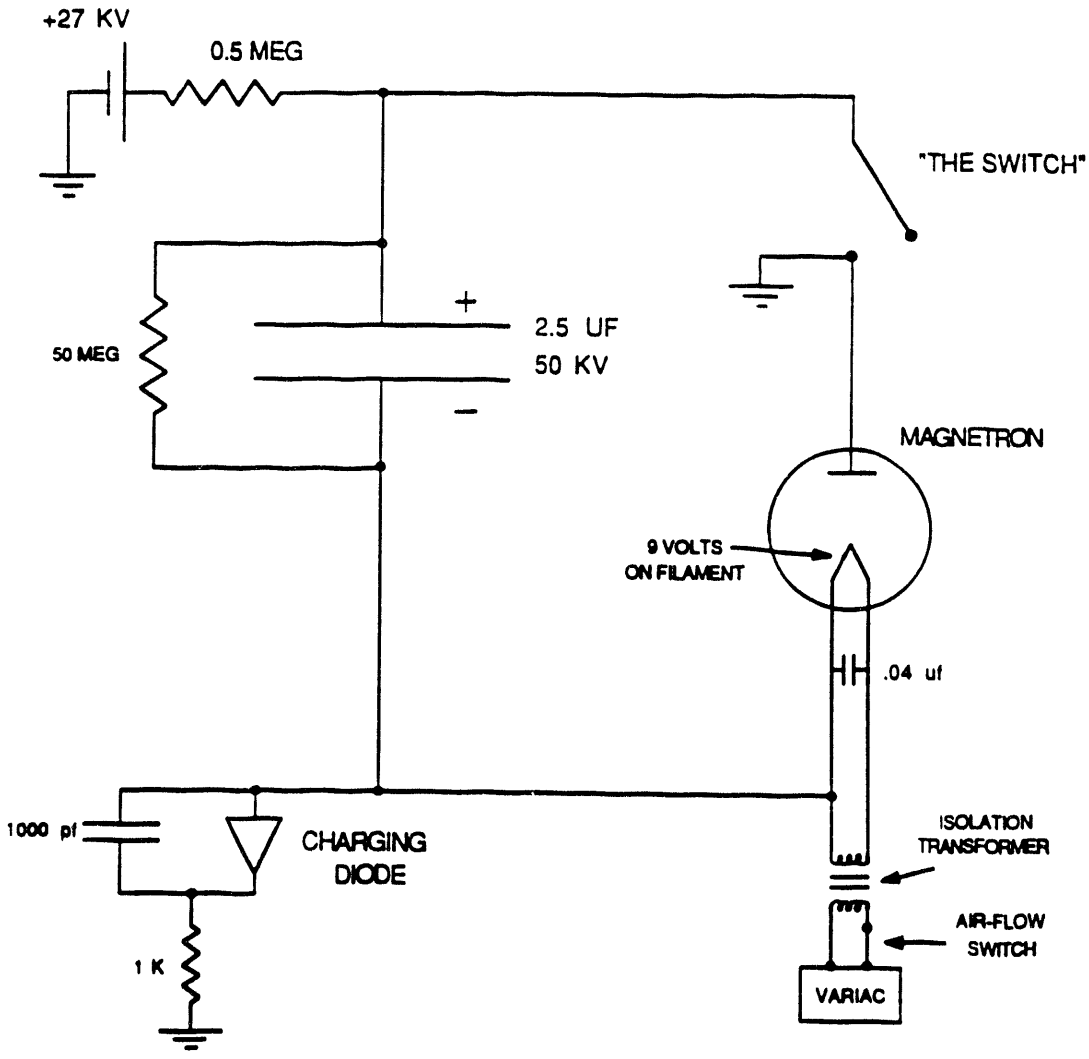

Figure A.2: Circuit diagram of the modulator used in the microwave experimental setup.

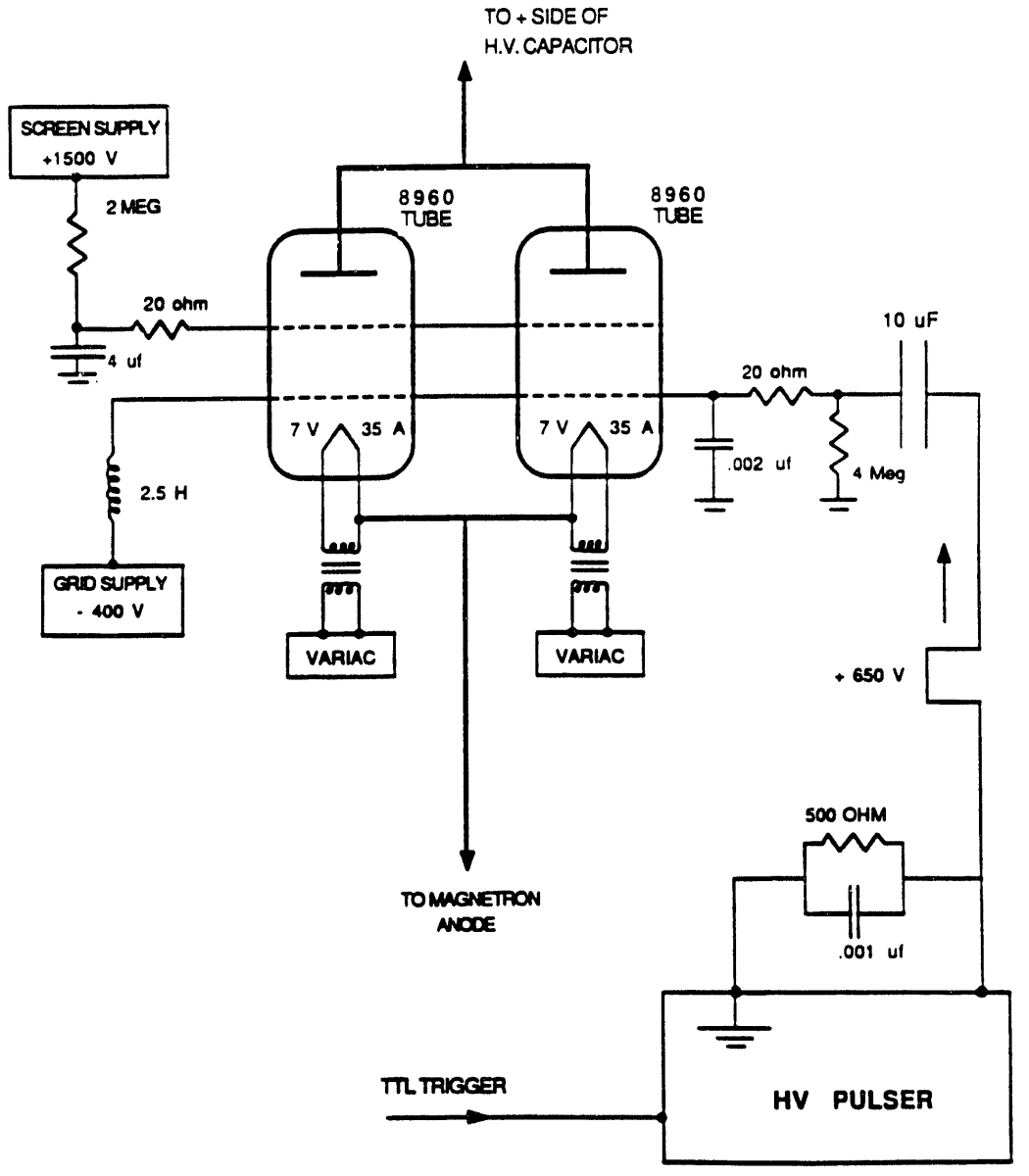

Figure A.3: Circuit diagram of the triggering/switching section of the modulator.

References

1. K. Miyamoto, *Plasma Physics for Nuclear Fusion* (MIT Press, Cambridge, 1980).
2. R. V. Jensen, D. E. Post, W. H. Grasberger, C. B. Tarter, and W. A. Lokke, Nucl. Fusion **17**, 1187 (1977).
3. F. Engelmann, Contr. Plasma Phys. **31**, 167 (1991).
4. R. B. White, *Theory of Tokamak Plasmas* (North-Holland, New York, 1989).
5. J. Wesson, *Tokamaks* (Oxford University Press, Oxford, 1987).
6. L. A. Artsimovitch, Nucl. Fusion **12**, 215 (1972).
7. J. F. Lyon, Plasma Phys. & Contr. Fusion **32**, 1041 (1990).
8. N. Hershkowitz, S. Miyoshi, and D. D. Ryutov, Nucl. Fusion **30**, 1761 (1990).
9. M. Tuszewski, Nucl. Fusion **28**, 2033 (1988).
10. B. L. Wright, Nucl. Fusion **30**, 1739 (1990).
11. M. Yamada, Fusion Tech. **9**, 38 (1986).
12. M. N. Bussac, H. P. Furth, M. Okabayashi, M. N. Rosenbluth, and A. M. M. Todd, in *Plasma Physics and Controlled Nuclear Fusion Research 1978* (IAEA, Vienna, 1979), Vol. 3, p. 249.
13. C. Chin-Fatt, A. W. DeSilva, G. C. Goldenbaum, R. Hess, C. Cote, A. Filuk, J.-L. Gauvreau, and F. K. Hwang, Phys. Fluids B **5**, 1816 (1993).
14. M. Yamada, Nucl. Fusion **25**, 1327 (1985).
15. T. R. Jarboe, F. J. Wysocki, J. C. Fernandez, I. Henins, and G. J. Marklin, Phys. Fluids B **2**, 1342 (1990).

16. Y. Kato, N. Satomi, M. Nishikawa, and K. Watanabe, J. Phys. Soc. Jap. **59**, 939 (1990).

17. G. C. Goldenbaum, Phys. Scripta **T2/2**, 359 (1982).

18. W. Baade, Bull. Astron. Inst. Netherlands **12**, 12 (1956).

19. L. Woltjer, Proc. Nat. Acad. Sci. **44**, 489 (1958).

20. M. R. Brown and P. M. Bellan, Phys. Fluids B **2**, 1306 (1990).

21. M. R. Brown and P. M. Bellan, Nucl. Fusion **32**, 1125 (1992).

22. A. W. DeSilva, G. C. Goldenbaum, H. R. Griem, and E. Ott, "Maryland magnetic fusion research program, MS Spheromak", Laboratory for Plasma and Fusion Energy Studies, University of Maryland, 1982.

23. J. A. Antoniades, C. Chin-Fatt, A. W. DeSilva, G. C. Goldenbaum, R. A. Hess, and R. S. Shaw, "MS-The University of Maryland Spheromak Fusion Experiment", University of Maryland technical report, Laboratory for Plasma Research, 1986.

24. F. K. Hwang, *Measurement of Magnetic Properties of Confined Compact Toroid Plasma (Spheromak)*, Ph.D. thesis, University of Maryland, 1991.

25. R. C. Isler, Nucl. Fusion **24**, 1599 (1984).

26. Equipe TFR, Nucl. Fusion **17**, 1283 (1977).

27. K. Tei, *et al*, Nucl. Fusion **19**, 1643 (1979).

28. G. C. Goldenbaum, J. H. Irby, Y. P. Chong, and G. W. Hart, Phys. Rev. Lett. **44**, 393 (1980).

29. G. W. Hart, *Experimental Investigation of Spheromak Equilibrium*, Ph.D. thesis, University of Maryland, 1983.

30. T. A. Peyser, *Plasma Motion during the Formation Phase of the PS-3 and PS-3.5 Spheromaks*, Ph.D. thesis, University of Maryland, 1987.

31. B. J. Barrow, *Magnetic Helicity and Plasma Velocities in the PS-3.5 Spheromak Experiment*, Ph.D. thesis, University of Maryland, 1991.

32. P. N. Guzdar, J. M. Finn, K. W. Whang, and A. Bondeson, Phys. Fluids **28**, 3154 (1985).

33. M. Yamada, *et al*, Phys. Rev. Lett. **46**, 188 (1981).

34. W. C. Turner, *et al*, J. Appl. Phys. **52**, 175 (1981).

35. J. H. Hammer, C. W. Hartman, J. L. Eddleman, and H. S. McLean, Phys. Rev. Lett. **61**, 2843 (1988).

36. J. B. Taylor, "Relaxation of Toroidal Discharges", in *Pulsed High Beta Plasmas* (D. E. Evans ed., Pergamon Press, New York, 1976).

37. J. B. Taylor, Rev. Mod. Phys. **58**, 741 (1986).

38. A. Janos, G. W. Hart, and M. Yamada, Phys. Rev. Lett. **55**, 2868 (1985).

39. C. W. Barnes, *et al*, Phys. Fluids **29**, 3415 (1986).

40. L. Lindberg and C. Jacobsen, Astrophys. J. **133**, 1043 (1961).

41. M. N. Rosenbluth and M. N. Bussac, Nucl. Fusion **19**, 489 (1979).

42. S. C. Jardin, M. S. Chance, R. L. Dewar, R. C. Grimm, and D. A. Monticello, Nucl.Fusion **21**, 1203 (1981).

43. S. C. Jardin and U. R. Christensen, Nucl. Fusion **21**, 1665 (1981).

44. G. C. Goldenbaum, R. A. Hess, and R. S. Shaw, Rev. Sci. Instrum. **57**, 2691 (1986).

45. M. Yamada, in *Plasma Physics and Controlled Nuclear Fusion Research 1984* (IAEA, Vienna, 1985), Vol. 2, p. 535.

46. C. J. Buchenauer and A. R. Jacobson, Rev. Sci. Instrum. **48**, 769 (1977).

47. J. Volkl and G. Alefeld, in *Hydrogen in Metals* (Topics in Applied Physics Series, Vol. 28, Spring-Verlag, New York, 1978), Vol. 1, G. Alefeld and J. Volkl eds.

48. R. M. Mayo, C. K. Choi, F. M. Levington, A. C. Janos, and M. Yamada, Phys. Fluids B **2**, 115 (1990).

49. J. C. Fernandez, C. W. Barnes, T. R. Jarboe, I. Henins, H. W. Hoida, and B. L. Wright, Nucl. Fusion **28**, 1555 (1988).

50. T. Fujita, K. Saito, J. Matsui, Y. Kamada, H. Morimoto, Z. Yoshida, and N. Inoue, Nucl. Fusion **31**, 3 (1991).

51. R. B. Howell and Y. Nagayama, Phys. Fluids **28**, 743 (1985).

52. P. C. Thonemann, *et al*, Nature **181**, 217 (1958); A. N. Zaidel', O. V. Konstantinov, and G. M. Malyshev, Sov. Phys. Tech. Phys. **7**, 265 (1962).

53. J. M. Finn and P. N. Guzdar, Phys. Fluids B **3**, 1041 (1991).

54. J.-L. Gauvreau, *Ion Temperature Measurements in the Maryland Spheromak*, Ph.D. thesis, University of Maryland, 1992.

55. A. Hossain and M. H. Rashid, IEEE Trans. Ind. Applic. **27**, 824 (1991).

56. E. L. Dereniak and D. G. Crowe, *Optical Radiation Detectors* (John Wiley & Sons, New York, 1984).

57. S. G. Porter, Ferroelectrics **33**, 193 (1981).

58. E. H. Putley, Ferroelectrics **33**, 207 (1981).

59. S. T. Liu and D. Long, Proc. IEEE **66**, 14 (1978).

60. L. S. Kremenchugskii and O. V. Roitsina, Instrum. & Exp. Tech. **19**, 603 (1976).

61. C. E. Bush, *et al*, Nucl. Fusion **23**, 67 (1983).

62. I. Ogawa, *et al*, Jap. J. Appl. Phys. **25**, 1057 (1986).

63. Y. N. Kiselev and V. Z. Krokhin, J. Appl. Mech. & Tech. Phys. **17**, 577 (1976).

64. Y. Ta, Compt. Rend. Acad. Sci. **207**, 1042 (1938).

65. S. B. Lang, *Sourcebook of Pyroelectricity* (Gordon and Breach Science, London, 1974).

66. S. B. Lang, Ferroelectrics **7**, 231 (1974).

67. E. T. Keve, *et al*, Solid State Commun. **8**, 1517 (1970).

68. M. W. Geis, K. A. Smith, and R. D. Rundel, J. Phys. E **8**, 1011 (1975).

69. A. Viehl, *et al*, Rev. Sci. Instrum. **64**, 732 (1993).

70. G. Fiksel, S. C. Prager, and W. Shen, Bull. Amer. Phys. Soc. **37**, 1606 (1992).

71. J. Cooper, J. Sci. Instrum. **39**, 467 (1962).

72. TFR Group, J. Nucl. Mater. **93**, 377 (1980).

73. A. N. Vertiporokh, S. Yu. Luk'yanov, and Yu. S. Maksimov, Sov. J. Plasma Phys. **6**, 7 (1980).

74. E. D. Andryukhina, *et al*, Sov. J. Plasma Phys. **7**, 27 (1981).

75. K. Odajima, *et al*, Nucl. Fusion **18**, 1337 (1978).

76. C. L. Wang, *et al*, Rev. Sci. Instrum. **57**, 2177 (1986).

77. I. Pelah and A. Hauer, Rev. Sci. Instrum. **48**, 1068 (1977).

78. V. I. Bayunov and A. M. Pukhov, Sov. J. Opt. Technol. **52**, 62 (1985).

79. R. A. Ganeev, *et al*, Instrum. & Exp. Tech. **31**, 250 (1988).

80. E. J. McLellan and S. C. Stotlar, Opt. Spectra **15**, March issue, 55 (1981).

81. S. C. Stotlar, E. J. McLellan, and C. R. Jones, SPIE **288**, 421 (1981).

82. C. B. Roundy and R. L. Byer, Appl. Phys. Lett. **21**, 512 (1972).

83. C. Hilsum, J. Opt. Soc. Am. **44**, 188 (1954).

84. J. A. R. Samson in *Methods of Experimental Physics*, Vol. 13, Part A (Academic Press, New York, 1976).

85. B. Joye, P. Marmillod, and S. Novak, Rev. Sci. Instrum. **57**, 2449 (1986).

86. J. A. Snipes, D. Bora, and T. P. Kochanski, Fusion Research Center, Report No. 269, December 1984.

87. G. Miller, J. C. Ingraham, and L. S. Schrank, Rev. Sci. Instrum. **53**, 1410 (1982).

88. C. B. Roundy, *Advances in Pyroelectric Detectors*, Ph.D. thesis, Stanford, 1973.

89. Harris and Loeb, J. Opt. Soc. Am. **43**, 1114 (1953).

90. L. Harris and J. K. Beasley, J. Opt. Soc. Am. **42**, 134 (1952).

91. W. C. Walker and G. L. Weissler, Phys. Rev. **97**, 1178 (1955).

92. J. A. R. Samson, J. Opt. Soc. Am. **54**, 6 (1964).

93. A. Kuthy, Nucl. Instrum. Methods **180**, 17 (1981).

94. G. Miller, J. C. Ingraham, and R. Cowan, "Space- and Time-Resolved Bolometry on ZT-40M", Los Alamos National Laboratory, Report No LA-10577-MS.

95. A. B. Filuk, *Particle Confinement and Fueling Effects on the Maryland Spheromak*, Ph. D. thesis, University of Maryland, 1991.

96. R. L. Kelly, "Atomic and Ionic Spectrum Lines below 2000 Angstroms: Hydrogen through Krypton", J. Phys. Chem. Ref. Data **16**, suppl. No 1 (1987).

97. W. L. Wiese, M. W. Smith, and B. M. Glennon, *Atomic Transition Probabilities*, U. S. Dept. of Commerce, National Bureau of Standards (National Standard Reference Data Series NSRDS-NBS 4), Washington, D.C., 1966.

98. J. A. R. Samson, *Techniques of Vacuum Ultraviolet Spectroscopy* (Wiley, New York, 1967).

99. E. M. Reeves and W. H. Parkinson, J. Opt. Soc. Am. **53**, 941 (1963).

100. R. A. Knapp and A. M. Smith, Appl. Optics **3**, 637 (1964).

101. S. Costa, R. De Angelis, S. Ortolani, and M. E. Puiatti, Nucl. Fusion **22**, 1301 (1982).

102. B. L. Henke, *et al*, Atom. Data Nucl. Data Tab. **27**, 1 (1982).

103. E. Hinnov and F. W. Hofmann, J. Opt. Soc. Am. **35**, 1259 (1963).

104. K. Okazaki, K. Ando, and K. Mori, in *Diagnostics for Fusion Experiments*, E. Sindoni and C. Wharton, eds (Pergamon Press, New York, 1978), p. 169.

105. I. H. Hutchinson, *Principles of Plasma Diagnostics* (Cambridge University Press, Cambridge, 1987).

106. C. Breton, C. de Michelis, and M. Mattioli, J. Quant. Spectrosc. Radiat. Transfer **19**, 367 (1978).

107. P. G. Carolan and V. A. Piotrowicz, Plasma Phys. **25**, 1065 (1983).

108. M. E. Puiatti, C. Breton, C. de Michelis, and M. Mattioli, Plasma Phys. **23**, 1075 (1981).

109. R. A. Phaneuf, R. K. Janev, and M. S. Pindzola, *Collisions of Carbon and Oxygen Ions with Electrons, H, H2 and He*, Atomic Data for Fusion Series, Vol. V (Oak Ridge National Laboratory, 1987), publication ORNL 6090.

110. D. Gregory, *et al*, Phys. Rev. A **20**, 410 (1979).

111. R. P. Stafford, K. L. Bell, and A. Hibbert, J. Phys. B **25**, 5449 (1992).

112. S. Nakazaki and T. Hashino, J. Phys. Soc. Japan **43**, 281 (1977).

113. P. L. Dufton and A. E. Kingston, J. Phys. B **20**, 3899 (1987).

114. J. Mitroy and D. W. Norcross, Phys. Rev. A **39**, 537 (1989).

115. J. Halbritter, IEEE Trans. Elec. Insul. **EI-20**, 671 (1985).

116. Y. P. Raizer, *Gas Discharge Physics* (Springer-Verlag, Berlin, 1991).

117. W. Hartmann, *et al*, J. Appl. Phys. **65**, 4388 (1989).

118. S. Ramo, J. R. Whinnery, and T. Van Duzer, *Fields and Waves in Communication Electronics*, 2^{nd} ed. (John Wiley & Sons, New York, 1984).

119. S. I. Braginskii, "Transport Processes in a Plasma", in *Reviews of Plasma Physics*, Vol. 1 (Consultants Bureau, New York, 1965).

120. F. F. Chen, *Introduction to Plasma Physics and Controlled Fusion, 2^{nd} ed.* (Plenum Press, New York, 1984), Vol. 1.

121. G. M. Melin, D. P. Grubb, Bull. Am. Phys. Soc. **23**, 775 (1978).

122. G. Francis, *Ionization Phenomena in Gases* (Butterworths, London, 1960).

123. L. N. Dobretsov and M. V. Gomoyunova, *Emission Electronics* (Nauka, Moscow, 1966).

124. D. E. Shumaker, J. K. Boyd, B. McNamara, and W. C. Turner, Lawrence Livermore National Laboratory Report No. UCRL-85579, October 1981.

125. W. C. Turner, *et al*, Phys. Fluids **26**, 1965 (1983).

126. S. P. Auerbach, Phys. Fluids **25**, 1108 (1982).

127. A. Buffa, *et al*, in *Plasma Physics and Controlled Nuclear Fusion Research 1980* (IAEA, Vienna, 1981), Vol. 2, p. 275.

DATE
FILMED
5/19/94
END